

Diploma Thesis  
at the  
Freie Universität Berlin  
carried out at the  
Institut des Materiaux Jean Rouxel /  
Université de Nantes, France

---

**Spectrally Resolved  
Current Losses in Cu(In,Ga)Se<sub>2</sub>  
Thin-film Solar Cells**

---



Submitted by : **Jonas Lähnemann**, December 17, 2008  
Supervisors : Prof. Dr. Martha Lux-Steiner (FU Berlin)  
Prof. Dr. John Kessler (Université de Nantes)



# Contents

<b>1</b>	<b>Introduction</b>	<b>1</b>
<b>2</b>	<b>Cu(In,Ga)Se<sub>2</sub> Solar Cells</b>	<b>3</b>
2.1	The Photovoltaic Principle . . . . .	3
2.1.1	p-n Junctions . . . . .	4
2.1.2	Semiconductor Solar Cells . . . . .	5
2.2	Cu(In,Ga)Se <sub>2</sub> Thin-film Photovoltaics . . . . .	5
2.2.1	CIGS Material Properties . . . . .	7
2.2.2	Deposition . . . . .	7
2.2.3	The Window: Buffer Layer and TCO . . . . .	8
<b>3</b>	<b>Solar Cell Characterization</b>	<b>11</b>
3.1	Current-Voltage Characteristics . . . . .	11
3.1.1	Experimental Setup . . . . .	13
3.2	Quantum Efficiency . . . . .	14
3.2.1	Current Loss Mechanisms in Cu(In,Ga)Se <sub>2</sub> Solar Cells . . . . .	15
3.2.2	Internal versus External Quantum Efficiency . . . . .	17
3.2.3	Recombination in Cu(In,Ga)Se <sub>2</sub> . . . . .	18
3.2.4	Voltage Bias . . . . .	18
3.2.5	Bias Illumination . . . . .	21
3.2.6	Analytical Modelling of Quantum Efficiencies . . . . .	22
3.2.7	Derivation of Parameters from QE Measurements . . . . .	24
<b>4</b>	<b>Quantum Efficiency Setup</b>	<b>28</b>
4.1	Measurement Principle . . . . .	28
4.2	Setup Details . . . . .	29
4.2.1	Optics . . . . .	31
4.2.2	Electronics . . . . .	38
4.2.3	System Summary . . . . .	40
4.3	Discussion of System Precision . . . . .	41
4.3.1	Systematic Error Sources . . . . .	42

4.3.2	Random Error . . . . .	43
4.3.3	Reproducibility . . . . .	45
4.3.4	Intercomparison . . . . .	46
4.3.5	Summary of QE Precision . . . . .	48
4.4	Continuous Illumination QE on Dye-sensitized Solar Cells . . . . .	49
<b>5</b>	<b>Effects of Varying Cu Supply in Three-stage Absorber Growth</b>	<b>51</b>
5.1	Growth Specifics . . . . .	51
5.2	Surface and Bulk Analysis . . . . .	53
5.2.1	Absorber Surface . . . . .	53
5.2.2	Absorber Bulk Composition and Growth Model . . . . .	57
5.2.3	Summary of Surface and Material Characteristics . . . . .	61
5.3	Photoelectric Characterization . . . . .	62
5.3.1	Current-Voltage Characteristics . . . . .	62
5.4	Quantum Efficiency . . . . .	65
5.4.1	Quantitative Analysis of Current Density Variations . . . . .	68
5.4.2	Series Resistance Deduced from QE . . . . .	70
5.5	Another View on Interface Formation and Recombination . . . . .	72
5.6	Conclusions . . . . .	74
<b>6</b>	<b>Summary</b>	<b>77</b>
<b>A</b>	<b>Thin-film Material Characterization</b>	<b>81</b>
A.1	Scanning Electron Microscopy (SEM) . . . . .	81
A.2	Atomic Force Microscopy (AFM) . . . . .	82
A.3	Energy Dispersive X-ray Spectroscopy (EDX) . . . . .	83
A.4	X-ray Diffraction (XRD) . . . . .	84
A.5	Secondary Ion Mass Spectrometry (SIMS) . . . . .	86
	<b>Bibliography</b>	<b>87</b>
	<b>List of Figures</b>	<b>94</b>
	<b>List of Tables</b>	<b>96</b>
	<b>Acknowledgements</b>	<b>97</b>

# Abbreviations

AC	Alternating Current (symbolizes modulated light QE measurements)
AFM	Atomic Force Microscopy
AM	Air Mass
ASTM	ASTM International, former American Society for Testing and Materials
BNC	Bayonet Neill Concelman (coaxial cable connector)
CBD	Chemical Bath Deposition
CCD	Charge-coupled Device
CIGS	Cu(In,Ga)Se <sub>2</sub>
CIS	CuInS <sub>2</sub>
CNRS	Centre National de la Recherche Scientifique
DC	Direct Current (symbolizes continuous light QE measurements)
DSR	Differential Spectral Response
EDX	Energy Dispersive X-ray Analysis
EPD	End Point Detection
EQE	External Quantum Efficiency
FF	Fill-factor
IPCE	Incident Photon-to-current Conversion Efficiency
IQE	Internal Quantum Efficiency
$I(V)$	Current-Voltage (measurements)
NIR	Near-Infrared (light)
NREL	National Renewable Energy Laboratory (USA)
UV	Ultra-violet (light)
OH	Hydroxide
OP	Output Power
PEP	Photovoltaic Energy Project
PV	Photovoltaics
QE	Quantum Efficiency
QE(V)	Quantum Efficiency under Voltage bias
SCR	Space Charge Region
SEM	Scanning Electron Microscopy
SI	Système International (standard units)
SIMS	Secondary Ion Mass Spectrometry
SPM	Scanning Probe Microscopy
SR	Spectral Response
TCO	Transparent Conducting Oxide
TEM	Transmission Electron Microscopy
WPVS	World Photovoltaic Scale
XRD	X-ray Diffraction



# 1 Introduction

Among the most imminent challenges facing our modern society are the increasing global energy demand, dwindling of the conventional resources used for power generation and foremost the consequences coming along with an anthropogenic change in our earth's climate [1]. Nuclear power is not a solution, owing to the dangers from uranium mining, waste disposal and weapons proliferation, but also to limited resources. A key role in finding solutions to these problems, hence, comes to renewable energies and among them the use of solar energy [1, 2]. The sun delivers 162,000 terawatts (TW) in sunlight to the earth [3], about half of which reaches the earth's surface – in moderate climates we have about 1000 W/m<sup>2</sup> irradiation on a clear summer day. This can be harnessed for thermal applications or converted to electricity by concentrating solar power [4] and photovoltaics (PV).

The photoelectric effect was first observed by Alexandre-Edmond Becquerel in 1839 and theoretically explained by Albert Einstein in 1905. With the development of semiconductor p-n-junctions during the 1940s and their theoretical description by William B. Shockley in 1950, the fundamentals of modern semiconductor electronics, among them transistors and photovoltaic cells, were given. This quickly led to the first successful silicon solar cells being built at the Bell laboratories. They were also the first to work on CuInSe<sub>2</sub> as material for solar cells in the early 1970s, while the application in thin-films was pioneered by Kazmerski et al. [5].

For a long time photovoltaics was driven mostly by space applications and remote powering needs, however, the last decade has seen an explosion of the market, with growth rates exceeding 30 %, driven by increased installation of grid integrated systems pioneered by Germany and Japan [6]. While silicon wafer technology has so far been the workhorse of the PV industry, thin-film solar cells based on heterojunctions of direct bandgap semiconductors have become commercially available in the last years and are projected to get increasing market shares in the coming years [7]. They are based on either Cu(In,Ga)Se<sub>2</sub> or CdTe absorbers, the former so far having shown superior record efficiencies up to 19.9 % [8] and module efficiencies up to 13.4 % [9]. In comparison to silicon technology, reduced cell thickness and the need for less pure, polycrystalline material, as well as direct fabrication of modules, are among the reasons to expect a price advantage for thin-film modules with increasing production [10]. Production of thin-film solar cells faces certain restrictions in terms of metal resources, esp. indium; nevertheless there is still a huge growth potential [11]. In view of the complex nature of polycrystalline compound semiconductors in heterojunctions, progress in the past was often based on empirical work and hence there is still need to deepen the understanding of device physics [10].

Quantum efficiency measurements are among the fundamental characterization techniques for solar cells; probably the most important after current-voltage analysis of the diode characteristics. Through spectrally resolving the current yield of a photovoltaic device, quantum efficiency gives a closer view on the short-circuit current – one of the basic parameters of a solar cell – and loss mechanisms restricting it. It helps understanding the physics of current generation, recombination and carrier diffusion mechanisms. Hence, quantum efficiency is a valuable tool for scientists in this field.

In the scope of this report a quantum efficiency system was drafted and set up at the Université de Nantes to complement the characterizational possibilities of the research groups in  $\text{Cu}(\text{In,Ga})\text{Se}_2$  thin-film photovoltaics and electrochemical dye-sensitized solar cells. This is presented and discussed in chapter 4. An application of the system in a study on the correlation of  $\text{Cu}(\text{In,Ga})\text{Se}_2$  absorber morphology and device performance resulting from varied duration of the Cu-rich interval during isothermal three-stage co-evaporation of the absorber is the content of chapter 5. Fundamentals on  $\text{Cu}(\text{In,Ga})\text{Se}_2$  solar cells are given in chapter 2. Aspects of their characterization are discussed in chapter 3 with a focus on quantum efficiency measurements. Appendix A introduces the techniques from material physics used in this work.

# 2 Cu(In,Ga)Se<sub>2</sub> Solar Cells

To present the necessary fundamentals for later chapters, this chapter will introduce the basics of p-n junction semiconductor photovoltaics, as well as some details for thin-film solar cells. As specific example, Cu(In,Ga)Se<sub>2</sub> (CIGS) solar cells will be presented; this includes information on the cell setup, the material properties and the deposition process.

## 2.1 The Photovoltaic Principle

Planck introduced the notion confirmed by Einstein that the light's energy comes in discrete portions, later attributed to particles that were named photons. Every photon carries an energy  $E_{ph}$  that is the product of Planck's constant  $h$  and the light's frequency  $\nu$

$$E_{ph} = h\nu = h\frac{c}{\lambda} \quad (2.1)$$

The frequency [ $s^{-1}$ ] is related to the wavelength  $\lambda$  [m] through the speed of light  $c$  [m/s]. This concept delivered the explanation for the external photoelectric effect, where electrons are emitted from a metallic surface under illumination and carry the kinetic energy  $E_{kin} = E_{ph} - \phi$ ; here  $\phi$  is the metal's work function. The internal photoelectric effect is a variant in solids exhibiting a modest energy gap (bandgap)  $E_g$  between the valence band and conduction band, i.e. semiconductors.

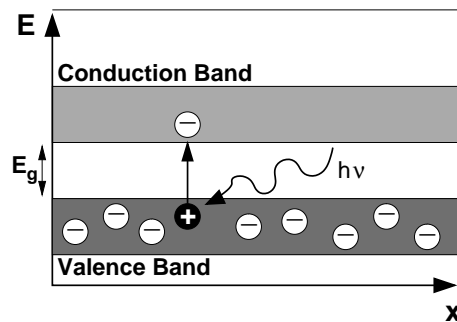


Figure 2.1: Schematic view of the band model for a semiconductor showing the internal photoelectric effect. The valence band is the highest energy band that is filled at 0 K, while the conduction band would be completely empty in that case. At higher temperatures thermic excitation will always lead to the availability of carriers – in contrast to insulators.

If the incident photon's energy exceeds that of the bandgap,  $h\nu \geq E_g$ , the energy transfer can excite an electron to the conduction band, leaving a 'hole' (free orbit) in the valence band (figure 2.1). This increase in free carriers, with holes acting as positively charged carriers, makes the semiconductor more conductive.

### 2.1.1 p-n Junctions

The electrical properties of a semiconductor can be modified through the introduction of impurity atoms. Atoms with an additional valence electron not needed for bonds in the crystal lattice are called donors and make a semiconductor n-type, i.e. provide additional negatively charged carriers that can participate in conduction. Conversely, p-type doping with acceptors uses atoms having a valence electron less than the host material. Consequently, the electron and hole concentrations differ in a doped semiconductor and the more common carrier type can be referred to as majority carrier, while the less common is called minority carrier. Doped semiconductors remain uncharged, but have a higher free carrier density and better conductivity. While in intrinsic (undoped) semiconductors the Fermi level is near the middle of the bandgap, it moves towards the conduction band for n-type and towards the valence band for p-type doping.

Bringing together an n-type and a p-type semiconductor creates a p-n junction. In a tendency to reduce the difference in carrier concentrations between the two sides, majority carriers from each side diffuse to the other. This allows the recombination of diffused carriers with majority carriers of the other side, leaving behind ionized donors (n-side) and acceptors (p-side) and resulting in an electric field that counteracts and limits the diffusion, see figure 2.2. The affected region is called space-charge region (SCR) or depletion zone. It is an insulating region between two conductive semiconductors. Concerning the band structure in thermal

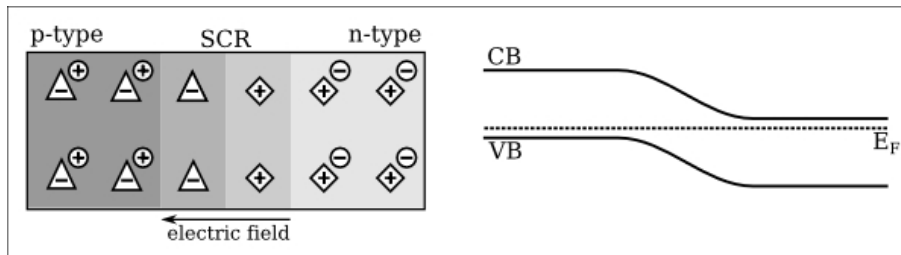


Figure 2.2: Scheme of a p-n-junction to visualize how the space-charge region (SCR) is formed. The triangles and diamonds indicate the acceptors and donors, while the circles stand for free carriers. To the *right* is a band diagram showing the band bending of conduction band (CB) and valence band (VB) through the alignment of the Fermi level  $E_F$ .

equilibrium, the Fermi levels align and cause a bending of conduction and valence bands (figure 2.2). Application of an external potential, referred to as voltage bias, will either increase (reverse bias) or decrease (forward bias) the potential difference between the two sides and therefore the width of the space-charge region. While a sufficient forward bias will allow a current to flow across the junction, it shows a current blocking behavior in reverse bias – we have a rectifying diode.

### 2.1.2 Semiconductor Solar Cells

The photovoltaic effect is the internal photoelectric effect in a p-n junction. If we consider the case of light incident on an unbiased p-n junction, each absorbed photon creates an electron-hole pair. When these carriers diffuse to the space-charge region, they are separated by the built-in electric field and accelerated in opposite directions. Consequently, a forward voltage is produced, because the electric field of the separated photoexcited carriers is opposite to the built-in field of the junction. Therefore, when connected to an external circuit, an illuminated p-n junction can serve as electric power source. In the case of silicon solar cells, one has a homojunction of oppositely doped silicon layers. Owing to silicon’s indirect bandgap – the valence band maximum and conduction band minimum do not coincide in momentum space and the simultaneous absorption of a photon and a phonon is necessary to bridge the bandgap – the absorption coefficient is rather low and cells have to be a few hundred micrometers thick. In p-n heterojunctions, two different compound semiconductors are joined to form a p-n junction, sometimes with an intermediate ‘buffer’ layer. Resulting from the different bandgaps of the used materials, the band diagram will become more complex; see figure 2.3. Usually, the semiconductors used in heterojunctions exhibit direct bandgaps allowing the cells to be a few micrometers thin; hence, the term thin-film solar cells is used.

## 2.2 Cu(In,Ga)Se<sub>2</sub> Thin-film Photovoltaics

The basic structure of a Cu(In,Ga)Se<sub>2</sub> thin-film solar cell is depicted in figure 2.3. The most common substrate is soda-lime glass of 1-3 mm thickness. It is coated on one side with molybdenum (Mo) that serves as metal back contact. The heterojunction is formed between the CIGS and ZnO semiconductor layers, buffered by a thin layer of CdS and a layer of intrinsic ZnO. The CIGS is p-type from intrinsic defects to a carrier concentration of about  $10^{16} \text{ cm}^{-3}$  [10], while the ZnO is doped n-type to a much larger extent through the incorporation of aluminum (Al) resulting in carrier concentrations in the order of  $10^{20} \text{ cm}^{-3}$  [14]. This asymmetric doping causes the space-charge region to extend much further into the CIGS than into the

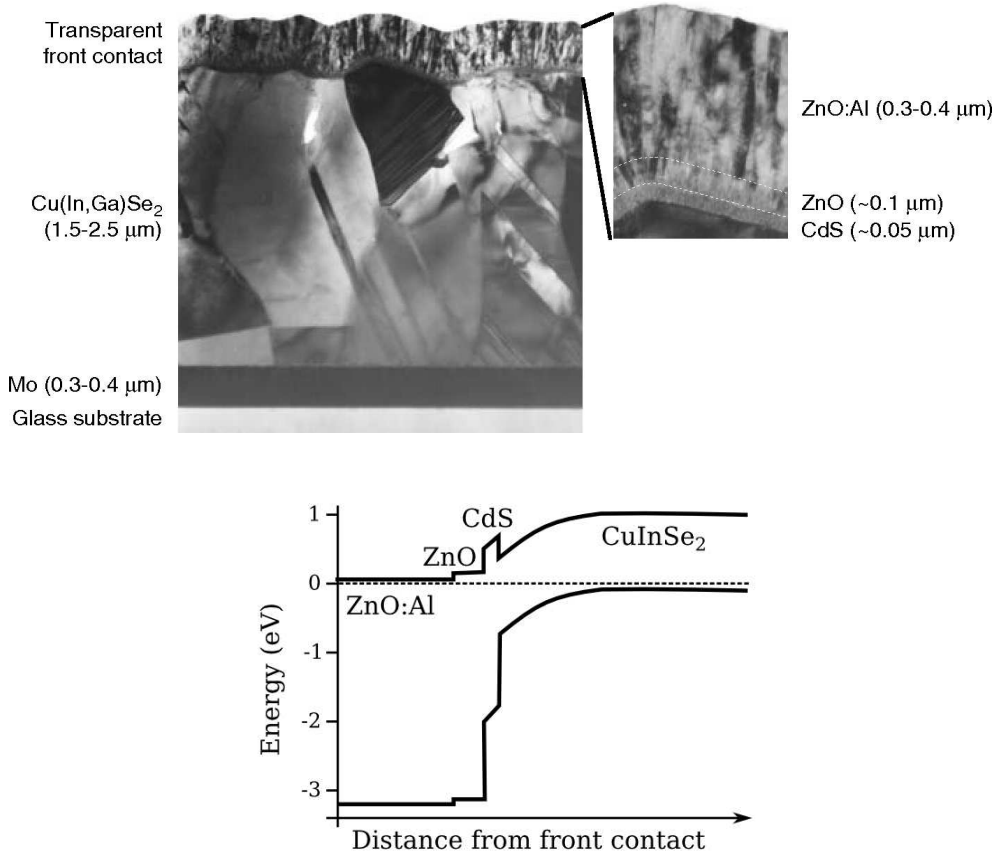


Figure 2.3: Transmission electron micrograph of a complete CIGS solar cell (*top*); the individual layers can be distinguished. *Reproduced from Platzer-Björkman [12].* A typical band diagram for CIGS solar cells is given *below*; it was drawn based on Klenk [13] and Shafarman and Stolt [10].

$\text{ZnO}$ . Matched to this are the layer thicknesses and the bandgaps of the materials: the wide CIGS layer serves as absorber with a bandgap between 1.02 eV ( $\text{CuInSe}_2$ ) and 1.65 eV ( $\text{CuGaSe}_2$ ). Absorption is minimized in the upper layers, called window, by the choice of larger bandgaps:  $E_{g,\text{ZnO}} = 3.2$  eV and  $E_{g,\text{CdS}} = 2.4$  eV. The doped  $\text{ZnO}$  also serves as front contact for current collection. Laboratory scale devices, typically 0.5  $\text{cm}^2$  large, are provided with a Ni/Al-grid deposited onto the front side to contact the  $\text{ZnO}$ . For the production of modules, individual cells are divided and monolithically interconnected by a series of scribing steps between the layer depositions [10]. Additionally, susceptibility to dampness makes module encapsulation a requisite for long lifetimes. The electronic structure of a CIGS solar cell is also given in figure 2.3 in form of a one-dimensional band diagram; details are still under dispute in the scientific community – some factors influencing the band alignment will be mentioned later, otherwise see for example Rau and Schock [15] or Klenk [13].

### 2.2.1 CIGS Material Properties

Cu(In,Ga)Se<sub>2</sub> is a I-III-VI<sub>2</sub> compound semiconductor exhibiting a chalcopyrite crystal structure, which is derived from the zincblende structure by alternately replacing Zn by Cu and (In,Ga). It has a tetragonal unit cell<sup>1</sup> with a ratio of lattice parameters  $c/a$  close to 2. In thin-films we have polycrystalline material, that in the case of CIGS, nevertheless, shows a high tolerance against defects, making it so valuable for photovoltaic applications. This includes structural tolerance for off-stoichiometric compositions and the electrically neutral nature of the structural defects. Examples of conditions that are tolerated and still yield solar grade material are: Cu-deficiency up to a Cu/(In+Ga) ratio of 0.7, varying gallium contents, and different grain sizes. The latter is attributed to passive grain boundaries [10]. Also, the use of soda-lime glass, resulting in an indiffusion of sodium into the absorber, has actually proven beneficial, as compared to more expensive glasses [16]. The bandgap can be engineered by changing the gallium content  $x$  in CuIn<sub>1-x</sub>Ga<sub>x</sub>Se<sub>2</sub>; typical values are  $x = 0.1...0.3$  ( $E_g = 1.1...1.2$  eV). Bandgap gradients have been investigated to further improve collection through additional fields [17, 18]; however, except for very thin absorbers ( $d < 1 \mu\text{m}$ ), the resulting gain is minimal. Optically, CIGS is characterized by a high absorption coefficient,  $\alpha > 10^5 \text{ cm}^{-1}$ , for wavelengths not too close to the bandgap.

### 2.2.2 Deposition

Deposition of CIGS can be either by precipitation of Cu, In and Ga precursors followed by annealing in a Se atmosphere at elevated temperatures, or by thermal co-evaporation (physical vapor deposition) of all the four elements under vacuum. In the latter case, each of the elements is evaporated from a separate crucible, their temperatures ( $T > 1000$  °C for the metals) determining the rates of evaporation and consequently that of the film growth. The substrate is held at a temperature of 400 to 600 °C to allow direct formation of the device-quality film. It has proven advantageous to vary the metal fluxes and possibly the substrate temperature, dividing the process into two or three stages. Usually the parameters are chosen so that the film becomes temporarily Cu-rich ( $\text{Cu}/(\text{In}+\text{Ga}) = y > 1$ ), while concluding with an average Cu-poor ( $y < 1$ ) composition [19, 20]. The p-type doping by native defects is achieved through a growth under high selenium pressure (Se excess).

The highest efficiency in co-evaporation has been achieved by the three stage process, which is a modification of the sequential In+Se / Cu / Se deposition

---

<sup>1</sup>Adhering to the standard definition of a crystal unit cell, the lengths of its three sides are  $a = b$  and  $c$  – referred to as lattice parameters.

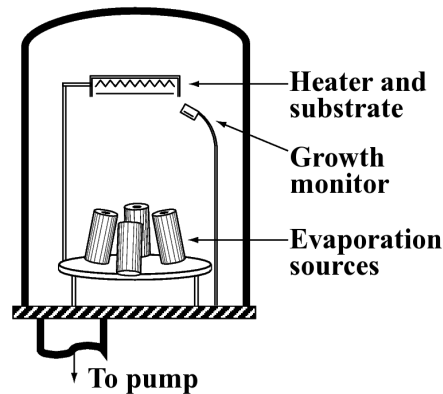


Figure 2.4: Configuration used for multisource elemental co-evaporation. The growth monitor is a quartz crystal. *Reproduced from Shafarman and Stolt [10].*

sequence proposed by Kessler et al. [21]. In the three stage process, the elemental fluxes follow a  $\text{In}+\text{Ga}+\text{Se}$  /  $\text{Cu}+\text{Se}$  /  $\text{In}+\text{Ga}+\text{Se}$  sequence, where the substrate is additionally held at different temperatures during the individual stages [22]; this growth sequence means that Cu deposition is limited to the second stage, at the end of which the film is Cu-rich before adding In and Ga again, a variation of this will be used in chapter 5.

### End Point Detection

A convenient way to monitor the co-evaporation process is the end point detection (EPD) [23]. This consists of recording the output power (OP) delivered to the infrared lamps used as substrate heater for maintaining a constant substrate temperature. The substrate temperature is controlled with a thermocouple in contact with the back side of the substrate. The output power needed is proportional to the emissivity of the developing film. Generally, the emissivity has been observed to be higher for Cu-rich phases than for Cu-poor ones, allowing the use of EPD to monitor the transitions from Cu-poor to Cu-rich composition and vice versa [23]. In chapter 5, this feature is used in an application of the EPD method.

### 2.2.3 The Window: Buffer Layer and TCO

The window layers transmit most of the light from the solar spectrum owing to their large bandgaps. For the n-type partner in the junction, which at the same time needs to be sufficiently conductive to serve as front contact, a transparent

conducting oxide (TCO) is selected. ZnO is cheap and rather easy to grow, making it the general choice. Additionally, buffer layers have proven to be essential in achieving high performance devices.

ZnO is sputtered, in research laboratories via radio frequency (rf) magnetron sputtering from a ceramic ZnO:Al<sub>2</sub>O<sub>3</sub> target (2 wt.% Al<sub>2</sub>O<sub>3</sub>) [24]. Sputtering consists of the erosion of material from a target by bombardment with ions from an argon gas. In a vacuum chamber the eroded material can then precipitate on the substrate. The thickness of the ZnO:Al layer in research cells is typically 0.3-0.4  $\mu\text{m}$ .

### **Why use a buffer layer?**

Experiments have shown better results when a buffer layer is added between the CIGS and ZnO, especially when this is CdS. A drawback in heterojunction solar cells lies in the higher chance of interface recombinations related to lattice mismatch and other imperfections at the junction interface resulting in a higher density of defect states. In this context, a variety of reasons for the benefit in using a buffer layer have been suggested. Among them are a protection of the absorber surface against damage from ZnO sputtering, surface etching in the chemical bath used to deposit the CdS and the indiffusion of Cd into the absorber. The latter seems correlated to a Cu depletion in the absorber surface layer that can lead to a substitution of Cd<sup>2+</sup> for Cu<sup>+</sup> based on their closely matched ion radii. This has been related to a type inversion (p to n) of the absorber surface region, effectively moving the junction into the CIGS; thus, the minority carriers from the bulk become majority carriers at the device interface, having a lower recombination rate there [13, 25]. Also, lattice mismatch is rather moderate – at least for pure CuInSe<sub>2</sub> [10]. An optical benefit lies in the refractive index of CdS being intermediate to those of ZnO and CIGS and hence reducing overall front surface reflection [26].

Chemical bath deposition (CBD), i.e. growth from a liquid solution, has been established as most effective and, therefore, standard routine for CdS buffer deposition [27]. The thickness of CdS is optimized in terms of losses related to CdS absorption and gain by beneficial effects – usually it is chosen at 40-50 nm. CBD results in a very conformal covering, even of rough absorbers and deep crevices (chapter 5). When thin CdS layers are employed, it has been established that an additional buffer of sputtered intrinsic ZnO ( $\sim 0.1 \mu\text{m}$ ) helps to achieve the best performance [10].

For several reasons, intensive research has been focussed on the replacement of CdS by ‘alternative’ buffers during the past years: First of all, the majority of buffer absorption constitutes a collection loss (see section 3.2.1); a higher bandgap

or less absorbing semiconductor would therefore be desirable. Second, the chemical bath deposition is not a vacuum process and consequently harder to integrate in a production line dominated by vacuum depositions. Finally, due to the toxicity of Cd, its use requires additional care and is subject to regulations. Work has focussed on different materials, among them  $\text{In}_2\text{S}_3$ ,  $\text{Zn}(\text{O,S})$  and  $(\text{Mg,Zn})\text{O}$  grown by various methods [12].

### **Buffer Photoconductivity**

As will be pointed out in the next chapter in a discussion of the effect of voltage and light bias on quantum efficiency measurements, the photoconductivity of CdS or other buffers plays a role in the device physics. Instead of contributing to the photocurrent, electron-hole pairs can be involved in such secondary effects. Reasons for a change of layer conductivity under illumination can include low free carrier concentrations (at low temperatures), light doping, or free carrier compensation by trap states. In CdS we find the last case, deep acceptors (hole traps), which usually compensate for n-type carriers, will be filled under blue illumination (photon energies that are absorbed in the CdS); as a result the layer has more uncompensated free electrons and becomes more n-type and, consequently, more conductive [28, 29]. This can have an influence on quantum efficiency measurements, as discussed in sections 3.2.4 and 3.2.5.

# 3 Solar Cell Characterization

Researching possible improvements to solar cell designs and trying to understand the underlying physical processes limiting their performance, it is important, on the one hand, to characterize the devices' electrical performance; on the other hand, it is necessary to study the composition and structure of the semiconductor layers building up the device (material characterization). This chapter will focus on the former, while techniques from material physics used later in this report will be covered in appendix A.

The discussion of solar cell characterization will focus on quantum efficiency (QE) measurements, as method to spectrally resolve the current yield of a solar cell and analyze associated losses. This will include the various loss mechanisms influencing the shape of the quantum efficiency curve, effects of measurements under voltage and light bias, basics of QE modelling and some procedures to determine cell parameters from the QE data. Experimental aspects of a quantum efficiency setup, exemplified by the system built in Nantes, are discussed in the next chapter. First, however, this chapter will give an introduction on current-voltage measurements as the most fundamental technique to characterize photovoltaic devices. The basic concepts mentioned in this chapter hold true for any kind of solar cell; the discussion and details will, however, focus on Cu(In,Ga)Se<sub>2</sub> thin-film cells.

## 3.1 Current-Voltage Characteristics

The most common and meaningful measurement on solar cells is recording the current-voltage  $I(V)$  (or  $I$ - $V$ ) behavior of the cell; this yields the characteristic diode curve. To obtain this curve, a varying bias voltage is applied to the cell and the resulting current is measured or vice versa.  $I(V)$  measurements on solar cells are usually performed under illumination at standard test conditions (light  $I(V)$ ), but additionally measurements without illumination (dark  $I(V)$ ) can yield valuable information. The standard conditions employed by the photovoltaic community are an illumination of 100 mW/cm<sup>2</sup> with a spectrum close to the AM1.5 solar reference spectrum [30] at a temperature of 25 °C.

From three points on the light  $I(V)$  curve, it is possible to deduce the basic cell parameters: open-circuit voltage  $V_{OC}$  [V], short-circuit current density<sup>1</sup>  $J_{SC}$  [mA/cm<sup>2</sup>] and fill factor FF; see figure 3.1. The fill-factor is defined as

---

<sup>1</sup>The cell's current density  $J$  and its actual current  $I$  relate via the cell area  $A$  [cm<sup>2</sup>]:  $I = J \cdot A$ .

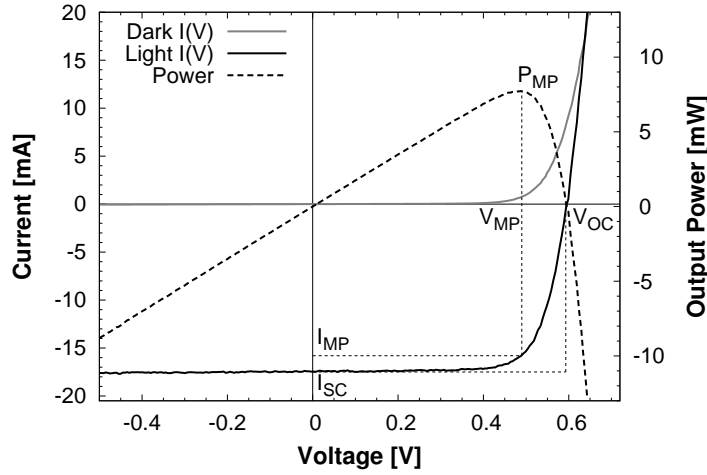


Figure 3.1: Characteristic current-voltage curve of a solar cell in the dark and under illumination. The resulting output power at different operating points is shown. The basic parameters short-circuit current  $I_{SC}$ , open-circuit voltage  $V_{OC}$  and the maximum power point  $P_{MP}$  with the associated current  $I_{MP}$  and voltage  $V_{MP}$  are marked.

$FF = (V_{MP}I_{MP})/(V_{OC}I_{SC})$ ,  $V_{MP}$  and  $I_{MP}$  [mA] being the voltage and current at the point of maximum power, and represents the ratio between the two squares marked by dotted lines in the fourth quadrant of figure 3.1. From these the efficiency  $\eta$  of a cell is defined as

$$\eta = \frac{P_{MP}}{P_{AM1.5}} = \frac{V_{MP}I_{MP}}{P_{AM1.5}} = \frac{V_{OC}J_{SC}FF}{100 \text{ mW/cm}^2} \quad (3.1)$$

with  $P_{AM1.5}$  the incident light power at AM1.5 illumination and  $P_{MP}$  the output power of the cell at its maximum power point.

The information content of current-voltage data is, however, not limited to these basic parameters. The curves allow conclusions on the quality of the p-n junction and losses related to resistive components of the device. A quantitative analysis can be derived from diode equations based on a one or two diode model. These are based on the exponential Shockley equation for a diode, which in the simplest form reads

$$J = J_0(e^{qV/AkT} - 1) \quad (3.2)$$

where  $J_0$  [mA/cm<sup>2</sup>] is the reverse saturation current density of the diode,  $V$  [V] the applied voltage on the device,  $J$  the resulting current density,  $q$  [C] the elementary charge,  $A$  the dimensionless diode ideality factor,  $k$  [J/K] the Boltzmann constant

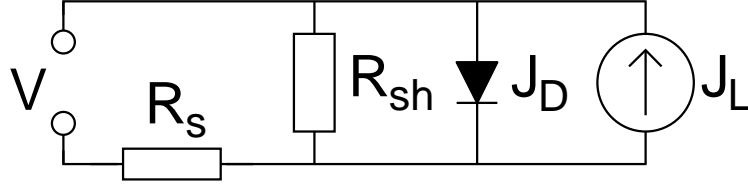


Figure 3.2: Equivalent circuit of a solar cell using a one diode model; including a diode (the p-n heterojunction) with an associated current density  $J_D$ , a current source accounting for the light generated current density  $J_L$ , as well as series resistance  $R_s$  and shunt resistance  $R_{sh}$ .

and  $T$  [K] the temperature. Extending this equation based on the equivalent circuit for a solar cell in the one diode model shown in figure 3.2, we get

$$J = J_0 \exp \left[ \frac{q(V - JR_s)}{AkT} \right] + \frac{V - JR_s}{R_{sh}} - J_L \quad (3.3)$$

where  $J_L$  is the light generated current density in the photodiode. The series resistance  $R_s$  [ $\Omega \cdot \text{cm}^2$ ] accounts for layer and contact resistance in the diode and the shunt (parallel) resistance  $R_{sh}$  [ $\Omega \cdot \text{cm}^2$ ] accounts for small shunt paths through or around the device layers. It is clear that ideally we want a minimal series resistance, but a maximal shunt resistance. The ideality factor allows conclusions on the mechanism dominating the forward current: Diode ideality  $A$  close or equal to 1 indicates thermionic emission as dominating effect, while  $A$  approaching 2 points towards the recombination current in the device as prevalent mechanism. The possible dependence on voltage and illumination level of these quantities can complicate the analysis. [31–33]

### 3.1.1 Experimental Setup

Diode characteristics were recorded with the  $I(V)$  setup in Nantes, consisting of an Oriel model 81150 solar simulator, a Keithley 2601 sourcemeter as precise voltage source and amperemeter, as well as a temperature control for the device under test. The system's lightpower is calibrated with CIGS solar cells measured at NREL for reference.  $I(V)$  measurements are performed in the four-probe configuration, i.e. two pairs of needles for the front and back contact, to minimize effects associated to contact resistance.

Depending on the quality of the solar simulator used, errors in the  $J_{SC}$  are introduced by the limited spatial uniformity of the illumination and the spectral mismatch in relation to the solar spectrum. The latter can be corrected for in a calculation when very accurate values are desired [31]; this is implemented at institutions providing certified measurements.

## 3.2 Quantum Efficiency

Quantum Efficiency  $QE(\lambda)$  is a dimensionless parameter characterizing the current collection in solar cells. It is defined by the ratio of electrons collected from the device per incident photons at each wavelength:

$$QE(\lambda) = \frac{\# \text{ of electrons collected}}{\# \text{ of incident photons}} = \frac{N_e}{N_\nu} = \frac{I(\lambda)/q}{\Phi_p(\lambda)} \quad (3.4)$$

where  $I(\lambda)$  [A] is the photocurrent,  $q$  [C] the elementary charge and  $\Phi_p(\lambda)$  the photon flow [ $s^{-1}$ ]. Therefore, it describes the ability of a solar cell to convert light of different wavelengths to a photocurrent, i.e. current gain and losses are spectrally resolved – which allows a detailed analysis of one of the main parameters determining its performance. In the case of an ideal photodiode, the quantum efficiency would be a step function that is unity for all wavelengths below the wavelength corresponding to the absorber band-gap and zero above. In reality unity can never be attained due to different loss mechanisms and the quantum efficiency looks more like in figure 3.3.

The possible limiting factors that can help to identify causes for insufficient current yield, are summarized in the following section. Afterwards, introductions are given to the internal quantum efficiency as possibility to separate optical losses and to the process of recombination limiting the current collection. As important add-ons to QE systems, the effects of voltage bias and light bias are discussed, while, concerning the physical description of quantum efficiency, basics of theoretical models are mentioned. Finally, the derivation of short-circuit current density  $J_{SC}$  and the absorber's optical bandgap  $E_g$  are presented.

### Spectral Response

Spectral Response essentially is the same as quantum efficiency, given in terms of the radiant power instead of the photon number, resulting in units of [A/W]:

$$SR(\lambda) = \frac{I(\lambda)}{P(\lambda)} \quad (3.5)$$

where  $P(\lambda) = \Phi_p(\lambda)h\nu$  [W] is the radiant power (or radiant energy flux) at a specific wavelength.

It relates to the quantum efficiency  $QE(\lambda)$  as:

$$QE(\lambda) = \frac{SR(\lambda)}{\lambda} \cdot \frac{hc}{q} \quad (3.6)$$

The factor  $hc/q$  equals 1.239842 for the wavelength in units of nm and the spectral responsivity in units of mA/W.

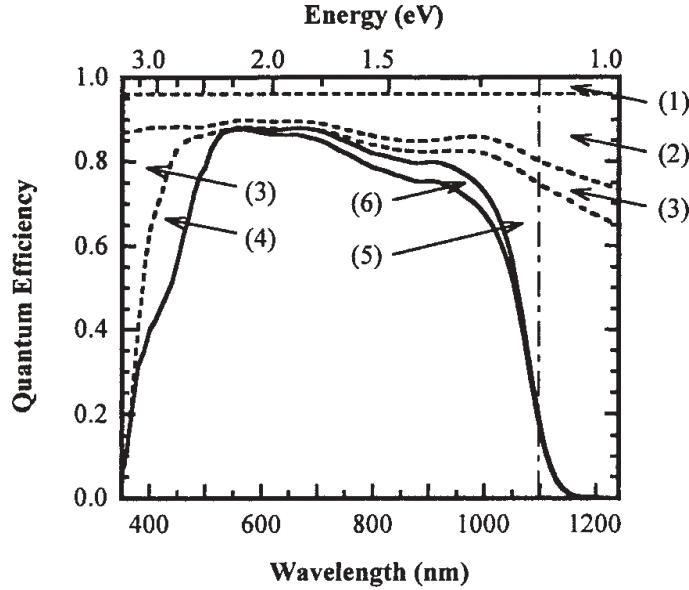


Figure 3.3: Loss mechanisms in quantum efficiency measurements on CIGS cells by: (1) Grid shading, (2) Front surface reflection, (3) TCO (ZnO) absorption, (4) Buffer (CdS) absorption, (5) Incomplete absorption in CIGS, and (6) Collection losses. The vertical line at 1100 nm marks the devices' bandgap. *Reproduced from Hegedus and Shafarman [32].*

### 3.2.1 Current Loss Mechanisms in $\text{Cu}(\text{In,Ga})\text{Se}_2$ Solar Cells

Knowledge of the possible origins of losses in the QE spectra allows quite a variety of conclusions from a qualitative analysis. Additional measurements under voltage and light bias can complement this. In most cases, this will be sufficient to pinpoint loss mechanisms, although more complex quantitative analyses are possible employing theoretical models. This discussion will be based on  $\text{Cu}(\text{In,Ga})\text{Se}_2$  cells (refer to device structure in 2.3), but most processes are also important in other thin-film cell concepts. Based on figure 3.3, reductions in the quantum efficiency curve can be attributed to the following processes:

1. **Grid shading.** CIGS substrate devices on a laboratory scale usually use a contact grid as front contact resulting in a wavelength-independent 2-3 % loss across the whole spectrum. Often, as in our case, QE measurements are done with a small lightspot not touching the grids, whereby this loss does not occur in our measurements.
2. **Reflection.** All of the front surfaces of the air/ZnO/buffer/ $\text{Cu}(\text{In,Ga})\text{Se}_2$  interfaces reflect a portion of the incident light. The refractive indices play an important role here, as investigated for CdS buffers by Orgassa et al. [26].

In champion cells this reflection is often reduced by anti-reflection coatings. For very smooth surface morphology, the ZnO front and back surface constitute an interferometer, leading to an interference pattern in the reflection. For laboratory cells, the ZnO thickness is usually such that the interference appears in the visible spectral range. Examples of this are clearly seen in some of the samples investigated in chapter 5.

3. **TCO absorption.** The transparent conducting oxide (TCO) window layer, usually ZnO, has an absorptivity of 1-5 % across the visible part of the spectrum. Due to free carrier absorption, TCO absorptivity increases in the near infrared domain depending on the carrier concentration in the layer, while in the UV, the TCO's bandgap is the limiting factor for the QE. Carriers created by absorption in this highly doped layer have a brief lifetime and cannot diffuse into the space charge region. In CIGS solar cells, the space charge region is largely in the absorber due to the high doping of the n-type window and a type-inversion close to the p-type absorber's surface.
4. **Buffer absorption.** The bandgap of the buffer layer, if it is narrower than that of the ZnO layer, causes further losses. This is the case for the combination CdS/ZnO and results in a step in the QE between 400 nm and  $\sim 520$  nm. The magnitude of this step depends on the thickness of the CdS layer, and if the CdS is too thick ( $\gtrsim 150$  nm), all photons of this wavelength range are absorbed in the buffer. The majority of holes created in the n-type CdS are not collected, whereby the buffer absorption constitutes a loss. This can also be attributed to the type-inversion, which increases the recombination rate for holes from the buffer at the CIGS/CdS interface, while reducing the recombination rate for electrons from the absorber (the electrons become majority carriers at the interface); therefore, collection from the absorber is enhanced while that from the buffer is hindered [13]. Apart from this, recombination at the CdS/ZnO interface could impair the collection from the CdS. Others suggest an influence of the large number of trap states for holes in CdS in making the buffer absorption a loss mechanism [29].
5. **Absorber bandgap and incomplete absorption.** Adhering to the principle of the internal photoeffect, charge carriers can only be created for photon energies exceeding the bandgap energy. According to  $\lambda = hc/E$  this minimum energy corresponds to a maximum wavelength. The cutoff will, however, not be abrupt – absorption just below the bandgap might be incomplete, while an absorption tail (Urbach tail) appears above the bandgap. The steepness of this cutoff is, among others, determined by bandgap gradients due to composition gradients in the Cu(In,Ga)Se<sub>2</sub>. For an absorber thinner than  $1/\alpha_g$ , where  $\alpha_g$  is the absorption coefficient just above the bandgap, losses by long wavelength transmittance become significant except when using light trapping (back reflector).

6. **Incomplete Collection.** Not all charge carriers might be collected before they recombine. This electronic loss is often stronger for long wavelengths, as these penetrate deeper into the absorber, and it is more likely that thereby created carriers cannot diffuse into the space charge region. In less efficient devices, a reason for losses might also be interface recombination, possibly aided by large spikes or a cliff in the conduction band. The process of recombination will be presented in section 3.2.3. To analyze the collection it is helpful to measure under voltage bias, see section 3.2.4.

### 3.2.2 Internal versus External Quantum Efficiency

To separate optical from electronic losses, an internal quantum efficiency (IQE) can be introduced. The “as measured” efficiency is then termed as external quantum efficiency (EQE). If no distinction is made, the term QE will always stand for the external quantum efficiency in this report.

Two definitions exist for the IQE. The first one, defines it as the generation and resulting collection from those photons which are incident on the junction [29], rather than on the complete device, and therefore requires to remove the reflectance of the cell:

$$IQE(\lambda) = \frac{EQE(\lambda)}{A(\lambda)} = \frac{EQE(\lambda)}{(1 - R(\lambda))} \quad (3.7)$$

where  $R(\lambda)$  is the reflectance and  $A(\lambda) = 1 - R(\lambda)$  the absorptivity of the cell. In this form the IQE can be calculated from a QE and a reflectance measurement on the complete device, assuming that the absorber is thick enough for complete absorption of even long wavelengths (zero transmittance); looking at figure 3.3, only loss #2 is removed.

A second definition found in the literature for the case of thin-film solar cells, says that the IQE corresponds to the current due only to photogeneration and collection in the absorber [32], i.e. also the losses due to absorption in the window layers, corresponding to losses #3 and #4 in figure 3.3, need to be removed in the calculation:

$$IQE(\lambda) = \frac{EQE(\lambda)}{(1 - R(\lambda)) \cdot (1 - A_{TCO}(\lambda)) \cdot (1 - A_B(\lambda))} \quad (3.8)$$

where  $A_{TCO}$  and  $A_B(\lambda)$  stand for the TCO and buffer absorption, respectively. This, however, requires reflectance and transmittance measurements for the respective layers at the employed thicknesses. Furthermore, these measurements can only be made for layers deposited on glass, with characteristics possibly deviating from those of layers in a device.

A similar discrepancy exists in the categorization of electronic and optical losses. While the former affect the generation of carriers, the latter reduce collection. Reflection, shading and incomplete absorption are clearly optical, while impaired collection from the absorber is clearly electronic. Although absorption in the TCO and buffer also creates electron-hole pairs, some authors argue that the desire to reduce absorption in these layers in favor of CIGS absorption, resulting from the poor collection from TCO and buffer, makes this in fact a kind of optical loss. I will, however, consider also this a collection loss and consequently adhere to the first definition of internal quantum efficiency. This means, I define optical losses as those not leading to the creation of free carriers, while electronic losses are those due to photogenerated carriers not contributing to the photocurrent.

### 3.2.3 Recombination in $\text{Cu}(\text{In,Ga})\text{Se}_2$

The nature of thin-film solar cells being heterojunctions of possibly lattice mismatched materials, made up of polycrystalline materials showing high levels of defects and furthermore incorporating impurities introducing further defects, are reasons allowing recombination of generated charge carriers to reduce the functionality of the device. Different recombination paths will affect the device parameters in a certain way, whereby electronic characterization of these parameters allows conclusions to be drawn on the dominant recombination mechanisms. Due to the large number of defects, Shockley-Read-Hall recombination [34, 35] through defect states is dominant over radiative recombination and Auger recombination for the case of CIGS solar cells [36]. The main recombination paths, in the space charge region and at the heterojunction interface, are depicted in figure 3.4; interface recombination is the dominant one in high efficiency CIGS cells [13, 37]. Additional paths, not shown in this figure, can be through defect states in the neutral region and at the back contact. In real semiconductors, we will have to account for more than a single discrete defect state. Additionally, the thermally activated Shockley-Read-Hall recombination can be enhanced by tunneling processes, especially at the interface and in the space charge region; though, according to Klenk [13], tunneling is of minor importance in high performance CIGS cells, as a band-structure enabling tunneling is not in agreement to requirements for high performance. Detailed discussions of recombination in chalcopyrites are given for example by Marrón [33] or Malmström [36]. Other factors that can also impair the device performance include conduction band barriers introduced by the buffer interface.

### 3.2.4 Voltage Bias

Application of an external voltage on the solar cell during the quantum efficiency measurement changes the width of the space charge region (SCR) and, thereby,

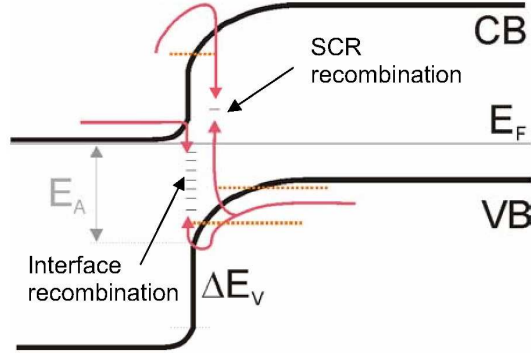


Figure 3.4: Main Recombination paths in heterojunction thin-film solar cells. CB and VB are the conduction and valence band,  $\Delta E_V$  is the valence band offset,  $E_F$  the Fermi level in equilibrium and  $E_A$  the activation energy for interface recombination. Thermally activated recombination via defect states within the bandgap is indicated by solid arrows, while dotted lines denote tunneling enhancement. The most dominant regions for such recombinations are in the bulk space charge region (SCR) and at the junction interface. *Reproduced from Marrón [33].*

influences carrier collection, especially at longer wavelengths. A forward bias will narrow the SCR and reduce carrier collection, while a reverse bias will broaden the SCR and a sufficiently large reverse bias should lead to complete collection.

To better distinguish influences of a wavelength independent change of  $QE(V)$  from one that is wavelength dependent, it is helpful to plot the ratio of QE measurements performed at different voltage biases to the unbiased quantum efficiency,  $QE(V)/QE(0)$ . The more this ratio deviates from unity for reverse bias, the larger is the loss due to incomplete carrier collection. If the ratio increases with wavelength, the SCR width  $w$  and carrier diffusion length<sup>2</sup>  $L$ , together giving what can be termed “efficient collection length”  $L_{eff} = w + L$  [38], are not sufficient for electrons created deep in the absorber to be collected. Wavelength independent deviation implies losses of carriers regardless of where in the absorber they were created; this can be due either to interface recombination or a barrier from heterojunction band-offsets (cliff or large spike) [32]. High efficiency CIGS solar cells usually show only minimal effects under reverse bias, but this procedure can help to identify mechanisms in less well behaved devices.

Under forward bias, the series resistance, see figure 3.2, can reduce  $QE(V)$ , because a portion of the voltage will drop across the resistive components. This can be derived from the diode model (eq. 3.3), as presented by Phillips and Roy [39] or in an alternative way by Sites et al. [40]. Consequently, a combined cell series resistance and measurement circuit load resistance  $R_S + R_L$  can be determined

<sup>2</sup>For CIGS, typically,  $w(0V) \approx 0.1-0.5 \mu\text{m}$  and  $L \approx 0.1-1 \mu\text{m}$  [32].

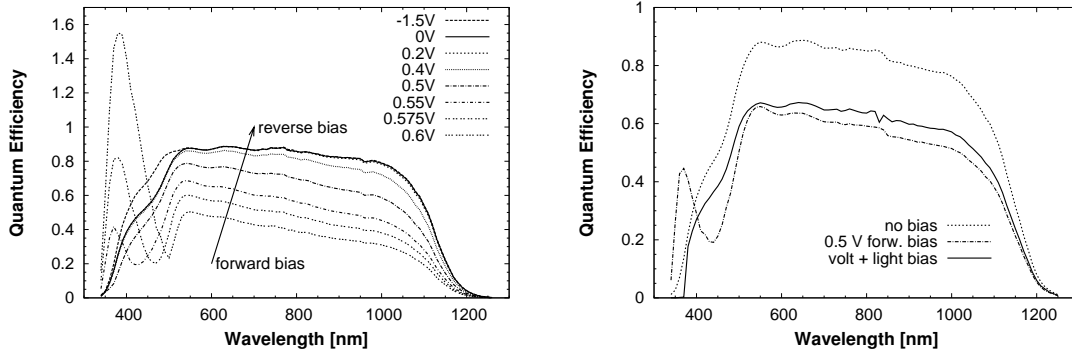


Figure 3.5: Reverse voltage bias artefact from CdS photoconductivity shown for a CIGS cell (*left*). While the response decreases independent of wavelength for photons absorbed in the CIGS, below 520 nm the photomodulated CdS conductivity allows an in-phase forward current. The valleys between 400 and 500 nm, are a result of the lock-in detecting absolute values. A slight increase of collection from the buffer can also be seen for a strong reverse bias. The *right* graph shows how the forward bias artefact is removed under lightbias.

from QE measurements under voltage bias; this procedure will be introduced and applied in chapter 5.4.2. If necessary,  $QE(V)$  can be adjusted to compensate for the series resistance effect [33]. As forward diode current is negligible near short-circuit conditions, standard QE measurements should not suffer from the series resistance effect. While it would be generally interesting to probe the quantum efficiency at the maximum power point to simulate more realistic operating conditions, the series resistance effect is likely to affect this measurement.

Another process, that influences voltage bias quantum efficiency, is photoconductivity of the buffer layer. CdS, for example, is well known to increase its conductivity with blue light exposure, i.e. illumination with photon energies higher than its bandgap. This can lead to a manipulated and even exaggerated response in the region of CdS absorption ( $< 520$  nm), shown in figure 3.5. Through the modulated (chopped) illumination commonly used in QE setups (see chapter 4) the conductivity of the buffer is periodically modulated, as long as the monochromatic light is in the spectral range absorbed by the buffer. This results in an in-phase modulation of the forward current introduced on the device by the applied bias and consequently modifies the measured signal. In forward bias, this can lead to negative signals; however, using lock-in detection, we only probe the absolute value of the signal. The resulting signal can sometimes even exceed unity, as seen in figure 3.5. It is therefore an artefact that can greatly obscure the shape of the  $QE(V)$ , but on the other hand gives an idea of CdS properties and influence. The artefact can be suppressed by additional bias illumination (light bias), as hole traps in the CdS will be filled with carriers generated from the continuous illumination

and not with those from the chopped beam, therefore avoiding the modulation of conductivity; this is shown in the right graph of figure 3.5. The photoconductive effect under bias is also discussed by Engelhardt et al. [41], Nagle [29] and Phillips and Roy [39]; the first even include the forward bias case in their theoretical model for buffer absorption.

Voltage bias QE will be used in the analysis of chapter 5, where some of the aspects mentioned here will be discussed.

### 3.2.5 Bias Illumination

The monochromatic beam used for QE measurements is much lower in intensity (in the order of  $\approx 0.01$  ‘suns’ for the system described in chapter 4), than typical operating conditions simulated in  $I(V)$  measurements ( $100 \text{ mW} \cdot \text{cm}^{-2} = 1$  ‘sun’, i.e. AM1.5 illumination). If the solar cell has a completely linear response, which it ideally should have, this would be irrelevant. There are, however, multiple mechanisms that can lead to an unlinear current response to light intensity. These include minority carrier trapping in the buffer layer and photoconductive effects [42], as well as conduction band spikes at the absorber/buffer interface.

Measurements simulating operating conditions can be achieved by superimposing the modulated monochromatic light with unmodulated ‘white’ bias light,  $\Phi = \Phi_{\text{monochromatic}} + \Phi_{\text{white}}$ . This is called the differential spectral responsivity (DSR) method [43]. The addition of the resulting large current on the small signal is a challenge on detection electronics, discussed in chapter 4. In most cases light bias effects will saturate at a fraction of AM1.5 illumination intensity [29]. For Cu(In,Ga)Se<sub>2</sub> with CdS buffer, Virtuani et al. [44] conclude that efficiency losses at low level illumination are mainly due to a shunt resistance effect on  $V_{OC}$  and FF and not on  $J_{SC}$  changes. Additionally, CIGS has a rather high carrier density, compared to CdTe absorbers, for example. Consequently, nonlinearities are usually not expected for this type of cells. For other buffer layers or growth conditions the case might be different. Instead of always measuring with the DSR method, it is common practice in research laboratories to implement light bias as additional option for quantum efficiency measurements.

Apart from low light level, the nature of monochromatic illumination introduces artefacts if absorption in certain spectral regions influences the collection in others. This can again be a result of CdS photoconductivity. Due to its large number of hole traps, the charge of CdS can increase under illumination. To balance this, the depletion width (space charge region) will increase and can enhance long wavelength collection; just as with reverse voltage bias, only that we are actually moving to a more realistic quantum efficiency. At the same time, short wavelength

response might increase slightly with illumination level when the hole traps in the buffer are filled (still there remains the issue of interface recombination for carriers created in the buffer).

While a spike in the conduction band at the absorber/buffer interface, as seen in figure 2.3, is desirable in heterojunctions, according to Klenk [13], the height of this spike can actually be illumination dependent. An increase of charge in the buffer layer under illumination can shift the Fermi level in the buffer closer to the conduction band and consequently reduce an existing spike. This is an effect from blue light that would be seen as wavelength independent improvement under bias light.

The effects just described are a result of blue photons, either from blue or white illumination. Red bias light will not have this effect and color (bandpass) filters might be used to pinpoint this; for example to examine losses due to band barriers in materials with alternative buffer layers, as done by Pudov et al. [45].

It should be added, that a strong bias illumination might introduce non negligible temperature changes in the test device, when not employing a temperature control.

### 3.2.6 Analytical Modelling of Quantum Efficiencies

Theoretical models have been introduced to describe the spectral current yield of solar cells analytically. These have two possible applications. First, by fitting to experimental data, unknown parameters in the model equations can be deduced. Second, simulations under variation of a single or a restricted number of parameters can give an idea on how the quantum efficiency is influenced by these and allow to develop the background for qualitative analyses, this was done in several of the works cited above. For a polycrystalline material, such as CIGS, simplified models have to be treated with care – particularly when trying to extract actual parameters. The absorption coefficient, to give an example, exhibits variations for different deposition methods.

In developing theoretical models for quantum efficiency of a solar cell, most authors focus on the generation and collection from the absorber, the basics of which will be presented in the following. Engelhardt et al. [41] have developed a model specially adapted to buffer layer absorption and interface recombination and included bias illumination as well as forward voltage bias effects.

In terms of the generation function  $g(\lambda)$ , i.e. the probability of an electron-hole pair being created by an incident photon, and the collection function  $F(\lambda)$ , i.e. the

probability that the generated minority carriers can actually be collected by the junction, the quantum efficiency can be redefined to

$$QE(\lambda) = g(\lambda)F(\lambda) = \int_0^d g(\lambda, x)F(\lambda, x)dx \quad (3.9)$$

where the integration over a layer thickness  $d$  is for the more realistic case of vertically changing generation and collection functions.

All models usually have in common that they derive the generation function  $g(\lambda)$  for their specific case from the Lambert-Beer law. It states that the photon flow  $\Phi_p$  at a depth  $x$  [m] in a medium with absorption coefficient  $\alpha$  [ $\text{m}^{-1}$ ] is:

$$\Phi_p(x, \lambda) = \Phi_p^0(\lambda)e^{-\alpha(\lambda)x} \quad (3.10)$$

where  $\Phi_p^0(\lambda)$  is the incident photon flow. With assumptions on recombination mechanisms, a collection function  $F(\lambda)$  is formed.

In the approach by Gärtner [38, 46], the one most widely used when considering the absorber only, majority carriers are neglected and an assumption of complete collection from the space charge region is made. For carriers generated beyond the space charge region the limitation of collection by diffusion to the SCR is assumed. Further, neglecting the recombination at the back contact this leads to a quantum efficiency

$$IQE(\lambda) = 1 - \frac{e^{-\alpha(\lambda)w}}{1 + \alpha(\lambda)L} \quad (3.11)$$

with the absorption coefficient  $\alpha(\lambda)$  for the absorber, the width of the space charge region  $w$  and the diffusion length  $L$  for minority carriers in the neutral bulk of the absorber. Due to the proportionality  $\exp(-\alpha w) \propto 1/(1 + \alpha L)$  for small  $\alpha w$  and  $\alpha L$  an effective diffusion length  $L_{eff} = w + L$  can be used to reduce equation 3.11 to

$$IQE = K(1 - e^{-\alpha L_{eff}}) \quad (3.12)$$

where  $K$  is a constant accounting for additional influences, such as interface recombination as well as window absorption. However, the analysis is not as straightforward as it may seem. As soon as any of the parameters included in  $K$  become wavelength dependent, for example by free carrier absorption in the doped ZnO, the extraction of  $L_{eff}$  from a fit to measured data will become less reliable. Additionally, the fit depends on the used  $\alpha$ ; some authors use literature values instead of exact measurements on their absorber, even though  $\alpha$  can vary for absorbers with different growth recipes. These are also the reasons, why no model fit of this kind will be performed to the data in chapter 5. For more complete models, equation 3.11 can be extended to include interface recombination [33], or to measurements under voltage bias allowing a fit to extract both  $w$  and  $L$  [47]. Other variations, by introducing restrictions to the collection from the SCR, are discussed by Nagle [29].

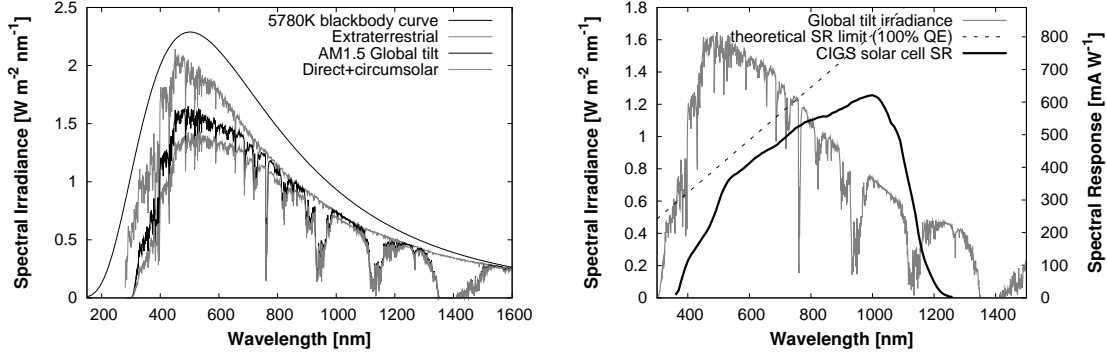


Figure 3.6: The *left* graph shows the ASTM G173-03 AM1.5 reference solar spectrum [30]. Also given are the AM0 (extraterrestrial) spectrum from which the AM1.5 spectrum was derived and the direct component (no diffuse irradiation) contributing to the global tilt spectrum, as well as a corresponding blackbody curve. The *right* graph compares the AM1.5 irradiance with a typical CIGS spectral response curve.

### 3.2.7 Derivation of Parameters from QE Measurements

The most important quantitative parameters deducible from quantum efficiency data are the short-circuit current density  $J_{SC}$  and the absorber's optical bandgap  $E_g$ . Their determination will be introduced and discussed in this section.

#### Short-circuit Current Density $J_{SC}$

The short-circuit current density  $J_{SC}$  can be obtained from quantum efficiency measurements by multiplying the spectral response  $SR(\lambda)$  [mA/W] with the illumination spectrum  $P(\lambda)$  [ $\text{W m}^{-2} \text{nm}^{-1}$ ] and integrating over the wavelength range:

$$J_{sc} = \int_{\lambda_{g,ZnO}}^{\lambda_{g,CIGS}} P(\lambda)SR(\lambda)d\lambda \quad (3.13)$$

Although, absorption tails widen the interval a little, it is here symbolized by the wavelengths  $\lambda_g$  at the bandgaps  $E_g$  for the ZnO window layer and the CIGS absorber, given by  $\lambda_g = hc/E_g$ ; where  $h$  is Planck's constant and  $c$  the velocity of light. Many authors use the quantum efficiency and an illumination spectrum converted to photon flux [26], which is simply a choice on which parameter to convert in order to reach compatible units. Commonly the Air Mass 1.5 Global Solar Spectrum given by ASTM standard G173-03 [30] is used for terrestrial solar cells [32, 48]. Figure 3.6 shows the global tilt AM1.5 solar spectrum<sup>3</sup> together

<sup>3</sup>The atmospheric conditions for the calculations of this spectrum are chosen to represent an annual average for the 48 contiguous states of the U.S.A. The surface is defined as facing the sun

with the AM0 (extraterrestrial) spectrum from which the former was derived and the direct irradiation contribution, i.e. excluding diffuse irradiation, as well as a corresponding blackbody curve<sup>4</sup>. Additionally, the figure gives a superposition of a sample spectral response measurement for a Cu(In,Ga)Se<sub>2</sub>-absorber and the AM1.5 spectrum. These are the two values folded and then integrated in equation 3.13 to obtain the short-circuit current density; the superposition gives a good visualization of the calculation and shows that all wavelengths have a comparable contribution to the current.

The so calculated  $J_{SC}$  can be compared with the value obtained from  $I(V)$  measurements and serve to verify the system calibrations. Due to limitations in spatial uniformity of illumination in an  $I(V)$  solar simulator and the susceptibility of  $I(V)$  setups to spectral mismatch, the calculation from quantum efficiency data generally allows a more exact determination of the short-circuit current density. It should be noted again, that our measurements don't include a grid coverage (figure 3.3); therefore, for comparisons with measurements done under illumination of the complete cell, the  $J_{SC}$  needs to be reduced to account for the grid coverage – for the cells from Nantes a grid coverage of 2 % is assumed.

### Determination of the Optical Bandgap

As illustrated above, the quantum efficiency is confined to the interval between absorber bandgap and window bandgap. The buffer layer is normally thin enough to transmit a portion of the photons and hence a step in the QE can be observed if the buffer-layer bandgap is lower than that of the window, as in the case of the common buffer CdS. The magnitude of this step can actually be used to estimate buffer-layer thickness in comparison to the response at known thicknesses.

The absorption edges at the bandgap exhibit tails and are not sharp drops due to decreasing absorptivity close to the bandgap; therefore, it is not straightforward to extract the bandgaps from a QE curve. A simple method lies in differentiating the QE-curve. The bandgaps of absorber, window and possibly buffer layers lie close to the inflection points, i.e. the extrema in the  $dQE/d\lambda$ -curve. A fit can be used to refine the result. See figure 3.7 for an example of two different absorbers. The values are less exact for the wider gaps of buffer and TCO, where the 10 nm step-size of the measurement corresponds to significantly larger energy intervals than in the long wavelength domain, according to the conversion of the scale by  $E = hc/(\lambda) \approx 1239.8[\text{eV} \cdot \text{nm}]/\lambda[\text{nm}]$ .

---

at 37° tilt toward the equator (=41.81° elevation above the horizon), as an average for the US latitudes. Irradiation is integrated hemispherically to include diffuse irradiation.

<sup>4</sup>Blackbody curve at 5780 K for the sun's average temperature downscaled by the inverse quadratic law to account for the distance between sun and earth.

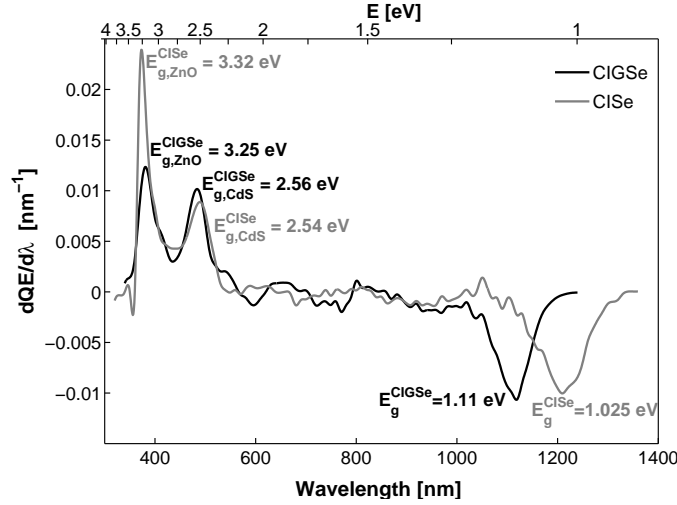


Figure 3.7: Example of bandgap determination by differentiation of a quantum efficiency curve. For the shown bandgaps values from literature are 3.2 eV for ZnO, 2.42 eV for CdS and 1.02 eV for CISE (0 % Ga) [10].

This method is deduced from the Gärtner model (equation 3.12) and the optical absorption coefficient  $\alpha$ , which for a direct gap semiconductor above the bandgap  $E_g$  is given by

$$\alpha h\nu = B(h\nu - E_g)^{1/2} \quad (3.14)$$

Here  $h\nu = hc/\lambda$  is the incident photon energy and  $B$  a material constant. Below the bandgap,  $\alpha$  is found to follow the exponential shape of an Urbach tail [49] with

$$\alpha = \alpha_0 \exp[\sigma(h\nu - E_0)/kT] \quad (3.15)$$

where  $\sigma$  is called steepness parameter;  $\alpha_0$  and the converging energy  $E_0$  are characteristic constants of the material, the latter being larger than the gap energy  $E_g$ ;  $kT/\sigma$  is the width of the exponential tail and, therefore, called Urbach energy  $E_U$ . From these expressions for  $\alpha$ , it is clear that also the QE of equation 3.12 exhibits a sharp drop just above  $E_g$  and below follows an exponential tail. This is just what we see in the quantum efficiency curves, however, this theoretical view clarifies that the inflection point extracted by the differentiation proposed above should indeed be close to the bandgap.

It should be noted, that incomplete collection or the measurement of a quantum efficiency under insufficient illumination will reduce the slope at the long wavelength cutoff. This influences the absorber bandgap deduced from the measurement and, as the case may be, the calculation should emanate from measurements under reverse voltage bias and/or light bias. Furthermore, free carrier absorption in the ZnO and interferences in the reflection influence the bandgap region QE.

Other methods of bandgap calculation are based on an extrapolation of the bandgap edge to zero for a squared IQE or in a linear extrapolation derived from the Gärtner model and equation 3.14 [50]. For these methods a certain error results from choosing the interval for the linear fit. As all methods suffer the same experimental imprecision, none should be considered superior, however, the derivative method is the most straightforward.

# 4 Quantum Efficiency Setup

In the course of this diploma work, a system for measuring the quantum efficiency of solar cells was developed and set up at the Université de Nantes. This allows the routine application of this fundamental characterization technique on solar cells produced by the scientists in Nantes, while prior only selected cells could occasionally be sent for external measurements. This chapter is dedicated to a description of the measurement principle of the system leading to a discussion of specific details of its setup. Included are additional features of the system, such as measurements under light bias and voltage bias, as well as an option to investigate not only semiconductor based photovoltaic cells (AC mode), but also dye-sensitized solar cells (DC mode). Afterwards, an analysis of the measurement precision is presented, including comparisons to QE measurements by the National Renewable Energy Laboratory in Colorado, the Ångström Solar Center in Uppsala and the Helmholtz Zentrum Berlin. Finally, to verify the usability of the system for dye-sensitized solar cells, a few such measurements are presented. The further application on Cu(In,Ga)Se<sub>2</sub> solar cells is left to chapter 5.

## 4.1 Measurement Principle

As equation 3.4 suggests, it is necessary to measure the irradiant power reaching a photovoltaic device and the current produced by the device to obtain its quantum efficiency. The most common way of measuring the irradiation is to place a calibrated photovoltaic device with known quantum efficiency  $QE_{cal}$  in the light-path and afterwards measure the test device in the same lightpath. Then, using equation 3.4 for the test device and the calibrated device we get

$$QE = QE_{cal} \cdot \frac{I_{mes}}{I_{cal}} \quad (4.1)$$

where  $I_{mes}$  is the current produced by the test device and  $I_{cal}$  that from the calibrated detector. This calculation is based on the hypothesis that the photon flow  $\Phi_p$  reaching both devices is the same. To guarantee this, it is necessary to have a sufficiently stable lamp and optics, but also to ensure that the lightspot is smaller than the calibrated cell as well as the test device. If the latter was not fulfilled, we would need to know exactly what portion of the light is entering a device making the calculation much more complex and sensitive to errors. Assuming that the detection electronics stay the same, we can simply use the voltage given by a current to voltage amplifier instead of the current, and multiplicative errors drop out.

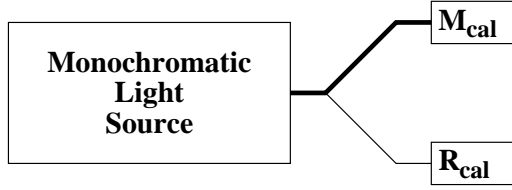
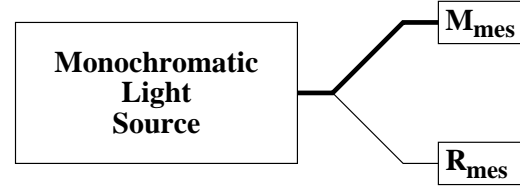
**a) Reference Calibration****b) Test Device Measurement**

Figure 4.1: Measurement principle of a dual beam QE-setup, where (a) the reference device is “calibrated” with the help of a calibrated detector. Afterwards, (b) measurements of test devices are carried out in relation to the reference.

This is the principle used for example by the SE2 group at the Helmholtz-Zentrum Berlin in their setup [33, 51].

A common extension is to add a light-splitter and to conduct measurements in relation to a reference (also called monitor) detector [52]. Now the reference detector is measured in comparison to the calibrated device first and subsequently actual measurements of test diodes are done in relation to the reference. This procedure is sketched in figure 4.1. The hypothesis that the photon flow stays constant is now replaced by the more easily satisfied hypothesis of a constant light-splitting ratio, i.e. the ratio between the photon flows in the two light-paths stays the same between calibration and actual test measurement. Still, the measurement of the calibrated cells is usually carried out at the beginning of each day to avoid errors that could appear from mechanical shifts.

For the extended setup we get the measurement equation by again taking equation 3.4 for all four measurements, the hypothesis of a constant light-splitting-ratio and the equality of reference device quantum efficiency during the subsequent runs. Let  $QE_{cal}(\lambda)$  be the calibrated quantum efficiency of our calibration cell,  $M_{cal}(\lambda)$  and  $R_{cal}(\lambda)$  the measurement and reference signals during calibration, as well as  $M_{mes}(\lambda)$  and  $R_{mes}(\lambda)$  the actual measurement of the device under test and the reference, respectively. Then, the quantum efficiency of the device under test  $QE_{mes}(\lambda)$  is:

$$QE_{mes}(\lambda) = QE_{cal}(\lambda) \cdot \frac{R_{cal}(\lambda)}{M_{cal}(\lambda)} \cdot \frac{M_{mes}(\lambda)}{R_{mes}(\lambda)} \quad (4.2)$$

The setup described in the following will be based on this dual-beam principle.

## 4.2 Setup Details

A photographic image of the QE system that has been assembled is depicted in figure 4.2. Schematically it is shown in figure 4.3. The design was inspired by

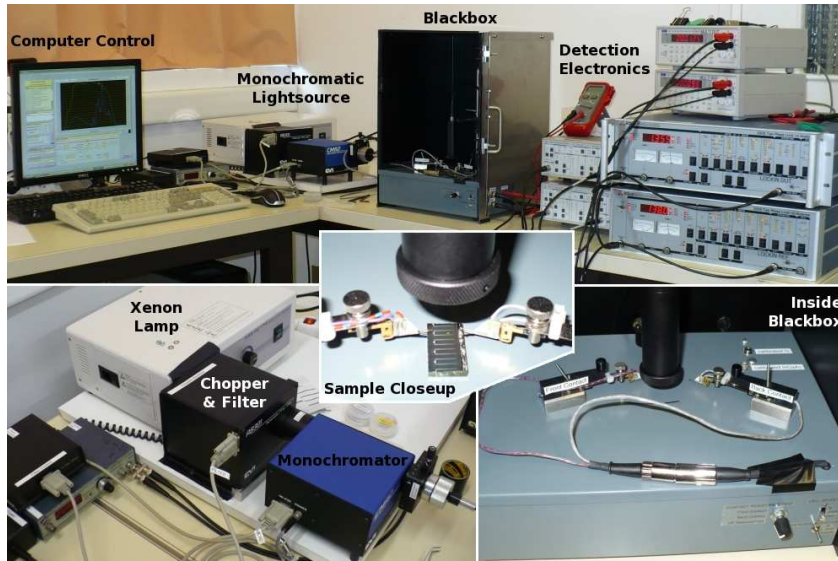


Figure 4.2: The quantum efficiency setup. The upper part shows a complete overview with the PC for control and the three main sections of the system: 1) the monochromatic light source, 2) the blackbox for light delivery, and 3) the detection electronics. Below, a more detailed view of the monochromatic light source and a view inside the blackbox are given. The inset in the middle shows a closeup of a solar cell under test.

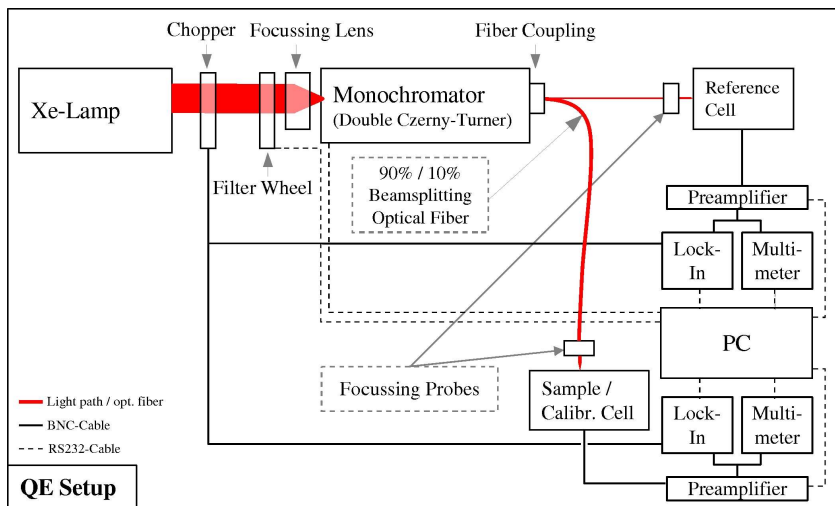


Figure 4.3: Schematic overview of the QE-Setup. It is a grating monochromator based dual-beam setup where the device under test (DUT) and a reference cell are illuminated at the same time. The system is designed for a chopped-light modus with lock-in detection for solid state (mainly CIGS) solar cells, as well as steady state (multimeter based) measurements for testing dye-sensitized solar cells.

a system at NREL described by Field [52]. Input came also from John Kessler's experience with the system at Ångström Solar Center in Uppsala and the system of the SE2 group at the Helmholtz-Zentrum Berlin. Nevertheless, the actual implementation was planned and carried out as part of this project to suit the specific requirements of the users in Nantes – especially, the successful inclusion of light and voltage bias is not self-evident. In the following part of this chapter, the individual elements will be discussed divided into a section on the optics and one on the electronics. Taking the three units distinguished in figure 4.2, these two parts meet within the blackbox at the photovoltaic devices.

As additional challenge, the system is required to measure both  $\text{Cu(In,Ga)Se}_2$  thin-film solar cells and dye-sensitized electrochemical solar cells. Periodic light modulation (chopping) combined with phase-sensitive detection (lock-in) allows a noise reduction and enables the application of light and voltage bias, which are DC components superimposed on the AC signal. This operation mode will be referred to as modulated, chopped or simply AC mode and is applied for the thin-film cells. Dye-sensitized solar cells exhibit much slower response times than semiconductor devices [53]. Therefore, lock-in detection is not feasible and we have to resort to measurements with continuous illumination and DC-multimeter detection. Care has to be taken about noise, as well as dark current offsets and we lose the option of measurements under bias. This operation mode will be referred to as unmodulated, continuous or DC mode.

Attention has been paid to a user friendly and stable operation of the system. In the course of this work, the measurement control has been automated in a LabView program. This includes wavelength, filter and grating changes, as well as control of the detection electronics, data acquisition and QE calculation. For some of the instruments customized drivers have been developed under LabView. The software structure, parameters and operation, together with maintenance details of the system, are described in a separate technical documentation. While the software allows the adjustment of most instrumental settings, only the calibration run requires manual intervention when changing the focus and switching between the calibrated silicon and indium-gallium-arsenide detectors. Such a run is usually performed once at the start of a measurement session.

### 4.2.1 Optics

The optical part of the setup is dedicated to illuminating the photovoltaic devices with monochromatic light across the complete spectral range they respond to. A convenient way to switch focus between calibrated detectors and test devices is necessary for the main lightpath and the lightspots need to be small enough to completely enter all devices, taking into account that the spot size might change

in the ultraviolet (UV) and near-infrared (NIR) spectral regions due to chromatic aberration in the lenses used for the setup. The desired broad spectral range especially into the UV poses a challenge and necessitates compromises in the design and choice of components. For example, optical elements with anti-reflective coatings or achromatic lenses could not be used.

## Light Source

The fundamental requirements to the light source are stability and a strong emittance across the complete spectral range desired for the measurements, especially down into the UV. This can be either obtained by a single lamp or by combination of two different lamps with light summing or a switching mirror. Our choice was a single Xenon lamp (ASB-XE-175EX from Spectral Products), as this offers the required broad band emittance (from 250 nm) in a single lamp. However, care has to be taken to avoid artefacts from the strong peaks in the Xenon spectrum. Furthermore, the lamp spectrum is far from resembling a solar spectrum. The former is assured in our case by the dual-beam setup. This prevents artefacts that could stem from slight imprecisions in the monochromator stepping producing significant deviations in proximity of the Xenon peaks during subsequent scans. The spectral mismatch is more of a concern in current-voltage measurements and for QE systems a sufficient intensity across the spectrum is of greater importance. The lamp model we chose includes a good parabolic mirror in the bulb, directly giving a collimated beam and maximizing the output power. However, it is not made for optical bench integration and care has to be taken in fixing it.

## Light Modulation and Filters

Signal detection with lock-ins allows to reduce the signal-to-noise ratio and to remove DC components from dark currents, i.e. offsets. To enable lock-in detection, the light has to be modulated at an adequate frequency. Therefore, we have installed a Stanford Research System SR540 optical chopper with controller. To allow measurements without lock-in detection, the chopper can be deactivated and manually set to a transmitting position. Typical chopping frequencies for Cu(In,Ga)Se<sub>2</sub> solar cells lie below 200 Hz and often a frequency between 60 Hz and 90 Hz is chosen [31, 33, 43, 54]. In agreement to this, our system usually operates at 86 Hz. A test on a high-efficiency CIGS cell with CdS buffer and on a less well performing one with In<sub>2</sub>S<sub>3</sub> buffer, however, showed that the QE was unaffected by the chosen frequency even for frequencies as low as 23 Hz and as high as 633 Hz.

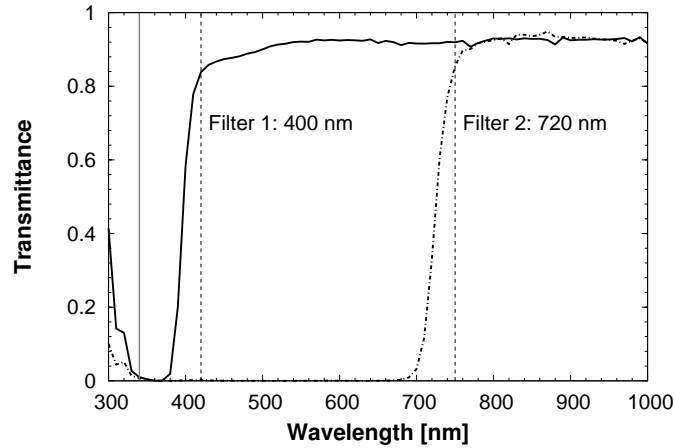


Figure 4.4: Transmittance of the long-pass optical filters with specified cut-on wavelengths at 400 nm and 720 nm. To maximize transmittance while assuring second order suppression the filters are entered into the lightpath at 420 nm and 750 nm, as symbolized by the dashed lines. The grey line at 340 nm symbolizes the lower limit of our measurement range, below which a signal appears despite the light blocking filters due to stray light passed by the monochromator.

Using a grating monochromator, it is necessary to prevent transmission of second order ( $\lambda/2$ ) and higher order diffractions in the monochromator. For this purpose we have an automated filter wheel (AB301 with controller AB300 from Spectral Products) with two long-pass order sorting filters transmitting beyond 400 nm and 720 nm, respectively. For lower wavelengths no filter is necessary, as our lamp emits only down to 250 nm and our optics absorb most light below 300 nm. A fourth position of the filter wheel holds a light blocking filter as shutter for the system, used for example to measure dark current offsets in unchopped measurements. The transmittance of the filters was checked by calculating the ratio of a measurement with filter in the lightpath to one without and is shown in figure 4.4. From this, the optimal wavelengths to enter the filters were determined to be 420 nm and 750 nm, shown by dashed lines in the graph. The filters start transmitting at 380 nm and 680 nm, respectively. Complete second order elimination is therefore guaranteed up to 1360 nm marking the upper end of our measurement range. The lower end of our measurement range is given by stray light scattered in the monochromator giving a phantom-signal below 340 nm, also visible in figure 4.4. The measurement range might be extended down to 300 nm or even slightly lower by employing a UV bandpass filter to remove the scattered light.

These two components are placed in front of the monochromator entrance as the use of a fiber as lightsplitter prevents them from being positioned behind the exit.

## Monochromator

Filter monochromators are sometimes used to offer a greater light transmittance, however, generally only for systems requiring a larger illuminated area. Otherwise, the common choice are grating monochromators. Our monochromator is a Spectral Products CM112 1/8 m dual monochromator (two Czerny-Turner monochromators in series) set up for additive dispersion mode. Each of the units has two ruled gratings with 600 grooves/mm blazed at 500 nm and 1200 nm. It is a rather short system, but disadvantages in spectral bandwidth and straylight are partially compensated for by the dual setup. For details on Czerny-Turner monochromators refer to Radziemski [55, 56] and Rosfjord et al. [57].

The bandpass  $\Delta\lambda$  of a Czerny-Turner monochromator can be calculated as [57]

$$\Delta\lambda = w \cdot \frac{\cos(\rho - \phi)}{knf}, \quad (4.3)$$

where  $w$  is the slit width,  $\rho = \arcsin(kn\lambda/(2 \cos \phi))$  the grating rotation,  $\phi = 12.7^\circ$  the Ebert angle<sup>1</sup>,  $k = 1$  the diffraction order,  $n = 600 \text{ mm}^{-1}$  the grating groove density,  $f = 220 \text{ mm}$  the focal length<sup>2</sup> and  $\lambda$  the wavelength.

The slits determining the bandpass of the monochromator are installed manually and as standard a set of 1.2 mm slits is used. This yields a theoretical bandpass value of approximately 11 nm across the wavelength range<sup>3</sup>, adequate for a spectral step size of 10 nm during the measurement. The theoretical value was confirmed by measurements using a HeNe-laser (632.8 nm) giving a bandpass of 10 nm.

Concerning stray light from the monochromator, the UV and visible regions were analyzed in the discussion of filter transmissions above (figure 4.4). For the long wavelength edge of the spectrum, measurements of quantum efficiency for energies below the bandgap of a device can be considered as shown in the left part of figure 4.5 for a CuInS<sub>2</sub> (CIS) and a Si solar cell. Only at 1360 nm a small “phantom-signal” appears. The remaining range was checked by recording QE curves of a Si cell with four different band blocking filters placed in the focussing probe. This is plotted in the right graph of figure 4.5. The curves correspond well with the transmission curves of the manufacturer and no unexpected stray light is observed. In conclusion, scattered light makes up 1 % of the signal at 340 nm and 1360 nm, below 0.5 % at 350 nm and 1350 nm and less than 0.1 % between 360-1340 nm.

---

<sup>1</sup>Angle between instrument axis and mirror principle ray; the manufacturer of our instrument calls  $2\phi$  the Ebert angle.

<sup>2</sup>Actually the focal length is 110 mm, but is multiplied by 2 to account for the use of a double monochromator.

<sup>3</sup>Including a 20 % addition recommended by the manufacturer.

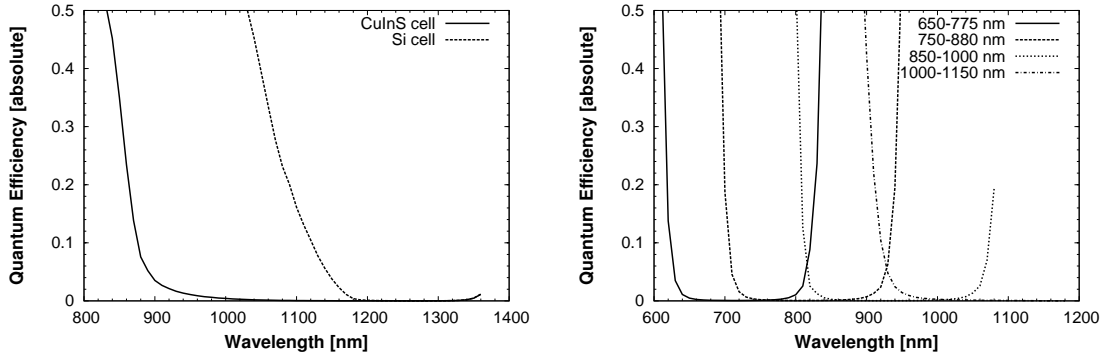


Figure 4.5: Stray light in the long wavelength domain is minimal except at the edge of the spectral range (1360 nm), as shown by the sub-bandgap energy QE plot for a CIS and a Si device in the left graph. For mid wavelengths, the same is shown through Si-diode QE curves with band blocking filters in the right graph.

## Light Splitting and Delivery

As described in section 4.1, quantum efficiency measurements can be made using single or dual beam systems. A dual beam system allows to compensate lamp drifts and errors due to the Xenon spikes and was therefore chosen for our setup. The necessary light splitting can be done using beamsplitters or a bifurcated fiber bundle<sup>4</sup>. The latter, as integrated into our system, has the advantage of great flexibility, ease of use, insensibility to dust and a depolarization of the light. Particularly, the horizontal beam from the optical bench can easily be diverted to illuminate the solar cells from the top. This, however, comes along with a major reduction in light intensity shown in figure 4.6; more than 80 % of the monochromatic light is lost – mostly due to insufficient coupling into the fiber. The slit image of our monochromator to fiber coupler is larger than the fiber tip, and additionally, the fibers of our bundle are circularly arranged, in disagreement to the form of the slit image. In the application of the system, the beam-power has proven to be still sufficiently strong to avoid nonlinearities in the device response due to low light conditions. Another disadvantage of a bifurcated fiber bundle as beamsplitter is the dependence of light coupling into the fiber on light geometry. Geometrical changes in the lamp output or mechanical changes in the lightpath before the coupling will change the light geometry illuminating the fiber tip. Therefore, they affect how much light is coupled into the individual fibers, which in turn determines the ratio of light splitting. At first, the arc in our Xenon light bulb was fluctuating regularly. This was such a major geometrical change that it was reflected in the light-splitting ratio. For an explanation we assumed that the cause were microscopic damages to

<sup>4</sup>The fibers of a bundle are divided with a certain number leading to one and the others to another end.

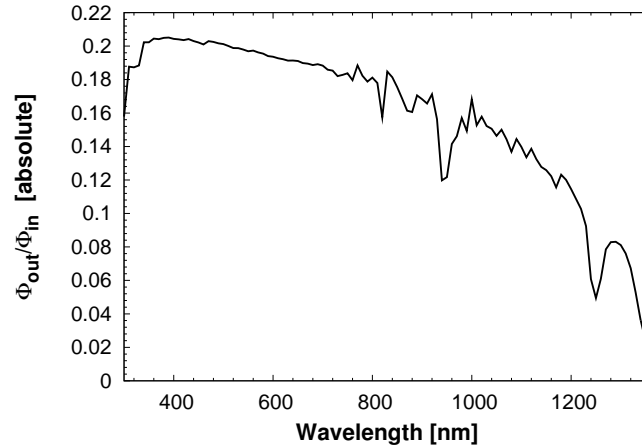


Figure 4.6: Spectral light transfer of the optical fiber setup  $\Phi_{out}/\Phi_{in}$ . The value is the ratio of measured intensity at the 90 % end of the bifurcated fiber bundle compared to the light intensity at the fiber coupler, i.e. complete transmission would correspond to a value of 0.9. The large loss can be attributed to the light coupling into the fiber. The dips at 950, 1250 and 1360 nm are OH absorption lines in the fused silica fiber, while the smaller spikes are artefacts caused by the lamp spectrum.

the bulbs cathode, suggesting bulb replacement. Looking at measurements over time for the repaired system a very good stability was found, refer to section 4.3.2 for details.

Our light-splitting ratio is 90 % to the test/calibrated device lightpath (main lightpath) and 10 % to the reference lightpath, i.e. of 60 fibers in our bundle six were randomly chosen for the reference beam. We are using high OH fused silica fibers to transmit wavelengths down to 300 nm. Therefore, the transmittance curve of the fiber shows OH absorption lines in the near infrared region, a major one being visible at the end of our spectral range (figure 4.6). This is no major drawback. Looking at the typically measured signal intensity (figure 4.7), there is no reduction that is more significant than those appearing at other points in the spectrum.

Focus of the fiber output, which is more or less a point source, onto the detectors and test devices is achieved with a bi-convex lens (1 in. diameter and 1 in. focal length) positioned for approximately 1:1 imaging. The focussing probes fixing the fiber ferrule and housing the lens also include an aperture to cut straylight, which produces a halo around the lightspot. This can be either due to reflections from the fiber tip ferrule or due to the radial gradient in the fiber glasses' refractive index. The reference focus is permanently fixed in relation to the reference detector inside the base of the blackbox. The main focussing probe is vertically mounted and fixed

parallel to a pole, whereby, it can be moved around a constant radius to change focus between the calibrated detectors and test devices.

Concerning the size of the lightspot, we have to consider chromatic aberration that could lead to a deviation from the visible dimensions in the UV and NIR regions. This effect would be avoided by using reflective optics, however, that choice would be much less practical in the application. To estimate the influence of chromatic aberration on the spot size, calculations for the distance between lens and focus of the focussing lens were made and show a deviation of  $\pm 2$  mm across the spectral range to a distance of 46.5 mm for 550 nm green light at 1:1 imaging. To simulate this change for the main beam, the spot size was measured for green light in the focal plane and 3 mm above/below this. The diameter changed from 1 mm to 1.5 mm. We are therefore on the safe side, with the grid spacing on the CIGS cells being 2.5 mm and the diameters of the Si and InGaAs calibrated cell being 3.6 mm and 3 mm, respectively.

### Illumination Power of the Monochromatic Beam

With the knowledge of the optical components in the system, it is possible to interpretate a beam power spectrum, see figure 4.7 for a typical curve, calculated from the measured signal intensity<sup>5</sup>:

$$P(\lambda) = \frac{V(\lambda) \cdot a}{SR(\lambda)} \quad (4.4)$$

$V(\lambda)$  is the lock-in signal in [V],  $a$  the amplification in [mA/V] and  $SR(\lambda)$  the spectral response in [mA/W].

As the amplification is constant over the wavelength range, the difference between the two curves is due to the spectral response of the measured cells (in this case the calibrated Si and InGaAs cells). Now looking at the beam power, its increase below 500 nm and the subsequent valley around 800 nm are due to reduced reflectance of the blazed monochromator gratings optimized for 500 nm and 1200 nm, respectively. The small dip at 420 nm is due to the first filter being entered (figure 4.4), while the dip at 1250 nm and the decline in signal intensity towards the end of the spectrum are OH absorption lines in the fiber (figure 4.6). The peaks at 470 nm and above 800 nm are Xenon emission lines, the strongest at 830 nm falling together with the monochromator's lowest transmittance.

The beam power magnitude varies strongly over the spectral range due to the different optical components, but none of the losses lead to a point where the signal drops considerably more than at other wavelengths. The maximum power

---

<sup>5</sup>Waveform correction for the chopped beam was not applied in these calculations.

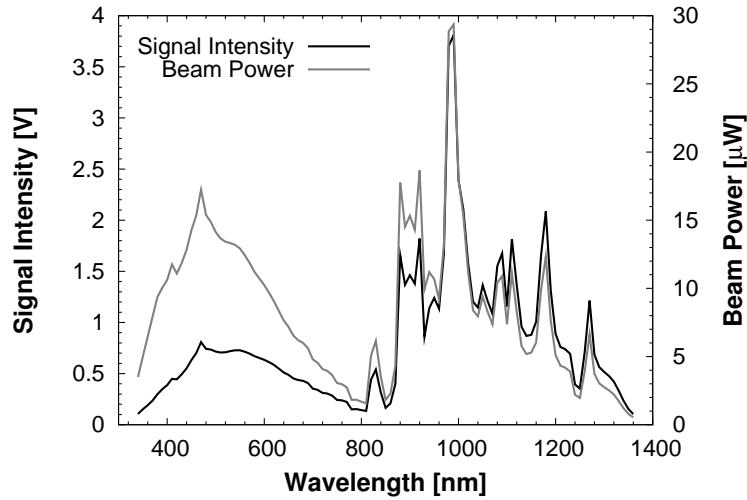


Figure 4.7: Typical signal intensity as read from lock-in and calculated beam illumination power of the QE system’s main lightpath across the measurement range.

is  $\sim 29 \mu\text{W}$ , while the average lightpower over the spectral range is  $\sim 8 \mu\text{W}$ . An increase in lightpower could be achieved by improving the coupling of light into the fiber bundle. However, in praxis the power has proven to be sufficient, as even cells that exhibited nonlinearities under lower light levels showed a response that did not improve with bias illumination.

### Bias Light

An additional feature that was included into the setup is bias illumination, to perform measurements with the device operating under stronger light intensity. To add the bias light during a measurement, a 30 W halogen lamp can be placed inside the blackbox to illuminate a complete cell with unchopped white light. Adjustment of the light intensity is done manually on the lamp power supply and can cover approximately 0.04 to 0.6 ‘suns’<sup>6</sup>. Handling of the DC currents induced thereby is discussed in the following section on the system electronics.

### 4.2.2 Electronics

The electronic part of the setup is adapted to accurately detect the low currents (nA- $\mu\text{A}$ ) produced in the photovoltaic detectors by the monochromatic illumination. To achieve this, the signal is first amplified in current to voltage preamplifiers.

<sup>6</sup>1 ‘sun’ being the intensity of AM 1.5 illumination =  $100 \text{ mW}/\text{cm}^2$ .

The voltage can then be detected using lock-in amplifiers or multimeters, depending on whether the light was chopped or not. Additionally, the amplifiers need to filter DC currents introduced by the optional light or voltage bias.

### Reference and Calibrated Detectors

Different choices exist to measure the luminous flux in the main and reference light-paths. Besides semiconductor photodiodes these include pyroelectric radiometers. However, using semiconductor based detectors and the same electronics as during test measurements causes all multiplicative errors to drop out, and it is unnecessary to apply a waveform correction factor related to the form of the chopped lightbeam [52, 58].

The signal of the reference beam is detected in a Si/InGaAs-tandem photodiode to cover the necessary spectral range with a single device in the lightpath. The current of the two devices can be summed in a parallel circuit or the devices used sequentially with a switch. Either operating mode can be chosen, but no difference in the resulting quantum efficiency measurement was observed. As calibrated photodiodes we have separate Si and InGaAs photodiodes calibrated by Hamamatsu at 25 °C for the ranges 200-1180 nm and 910-1700 nm, respectively.

### Current to Voltage Preamplifiers

To amplify the nA to  $\mu$ A currents we use low-noise  $I$  to  $V$  amplifiers based on operational amplifiers, namely the SR570 from Stanford Research Systems. They include a bias voltage supply and therefore keep the device either at a potential of 0 V or at specified bias voltage in the range of  $\pm 5$  V. For the latter, the integrated bias power supply is connected in series to the cell.

Additionally, two electronic filters can be configured. They allow to cut AC noise in continuous light measurements on dye-sensitized solar cells by setting a 1 Hz low-pass filter. Measuring thin-film solar cells, they are set to a bandpass of 30-100 Hz for a chopping frequency of 86 Hz. This removes DC offsets and noise which could, when amplified with the signal, overload the amplifier output and lock-in input. Especially under light bias or voltage bias the DC components in the signal thereby superimposed on the AC signal can be suppressed. For white light bias on the complete cell the DC component can be up to 5 orders of magnitude larger than the signal from the monochromatic light, i.e. up to a few mA. As the electronic filters are placed after the first and second of three amplification stages, the gain might still need to be slightly reduced under bias to prevent overload of these amplifier stages.

## Lock-in Amplifiers and Multimeters

Detection of the amplified signals is where the distinction between chopped and continuous measurements manifests itself in the instrumentation. The AC signals of the former case are measured using lock-in amplifiers with a reference feed from the chopper; the latter case's DC signals are detected in digital multimeters. The signal varies over 2-3 orders of magnitude during a measurement as the edges of the QE curves coincide with points of low light intensity on the one hand, and the Xenon spikes give strong responses on the other hand. The detection electronics need to account for this with dynamic ranging.

The lock-ins used for the phase sensitive detection are old EG&G 5208 dual-phase lock-ins available to the research group. A dual-phase lock-in has two detection channels phase-shifted by  $90^\circ$  [59, 60]. Therefore, the system can give the magnitude of the signal without phase adjustment, as it is the root of the two channels' square-sum ( $M = \sqrt{A^2 + B^2}$ ). To use the broad dynamic measurement range of the lock-ins, even though their autoranging showed to be unreliable, the range selection was implemented on the software side. The only disadvantage in using the old instruments is a rather slow measurement (10 min per scan) due to their settling time, particularly after a range change.

For the DC measurements TTI 1906  $5\frac{1}{2}$  digit multimeters were purchased. Range selection is automatic. To account for dark currents a DC scan commences with the measurement of the offset that is subsequently subtracted from all measured values. Noise is reduced by averaging 5-10 measurements at each wavelength.

### 4.2.3 System Summary

The quantum efficiency system drafted and built in the course of this work is a grating monochromator based dual-beam setup. All measurements are referred to a "real-time" reference for more accurate measurements. The quantum efficiency of a test device is deduced according to equation 4.2 from that of a calibrated photovoltaic detector measured earlier in the same lightpath. The specifications of the system are summarized in table 4.1. Second and higher order transmission by the monochromator is prevented using long pass optical filters on an automated filter wheel. Stray-light from the monochromator is negligible across the spectral range. The light provided by a Xenon arc lamp is periodically modulated using a chopper to use lock-in detection for the amplified photo-current, thus enhancing the signal-to-noise ratio and eliminating dark current offsets. However, alternatively unmodulated measurements with a DC-multimeter can be made on electrochemical dye-sensitized cells to account for their longer response times. In

Table 4.1: System Specifications

<b>Item</b>	<b>Specification</b>	<b>Notes</b>
Spectral range	340-1360 nm	
Spectral resolution	2-20 nm	monochr. beam spectr. bandwidth
Standard resolution	10 nm	calibrated QE step size
Spectral step size	10 nm	default (minimum is 1 nm)
Uncertainty	5 %	
Wavelength uncertainty	$\pm 1$ nm	
Std. chopping frequency	86 Hz	for lock-in measurements (AC)
Measurement time	$\sim 10$ min	for complete range
Beam size	$\sim 1$ mm	minimum diameter
Beam power	$\sim 29 \mu\text{W}$	max. of Xenon spikes, 1.2mm slit
	$\sim 8 \mu\text{W}$	mean over spectral range
Beam power density	$\sim 1 \text{ mW}/\text{cm}^2$	0.01 “suns”, mean
Voltage-bias capability	$\pm 5$ V	usually around +0.5 V to $-1.5$ V
Light-bias capability	0.04-0.6 “suns”	manual adjustment

both operating modes the current signal is first converted to a voltage in preamplifiers. Light splitting (90 % test device + 10 % reference) and delivery is done using a bifurcated fiber bundle adapted to the monochromator. Additionally, the system includes the possibilities to add voltage bias using the preamplifier and light bias from a separate halogen lamp. The most prominent compromise in the design was done in the choice of an optical fiber bundle as light transmitter and splitter, incurring a significant loss in beam intensity, but at the same time allowing great flexibility, dust protection and ease of use. The complete measurement procedure is computer-controlled. The precision of the system will be discussed in the following.

### 4.3 Discussion of System Precision

The system was designed to reduce systematic and random error sources as discussed in the following. The discussion is divided into a section on systematic error sources and one on the random error. The focus is on the AC mode for CIGS solar cells, however, where applicable, differences in the DC mode for dye-sensitized cells will be mentioned. However, some influences on the precision are hard to quantify. Therefore, it is easier to look at the reproducibility of measurements and make comparisons to other systems than going into all the error details, as our system is not aimed at giving certified results.

### 4.3.1 Systematic Error Sources

The dominating influence on our system's precision lies in its traceability. The calibrated QE used in the calculations was provided by the photodiode's vendor Hamamatsu and the error for their measurement is given at  $\pm 5\%$  (10% below 400 nm). As semiconductor-based detectors are used in form of Silicon and InGaAs photodiodes, they could additionally drift with age requiring a recalibration [31]. Drift in the reference detectors is of no concern, as they only need to exhibit stability between measurements of the calibrated cells, usually performed at the start of every test session.

#### Monochromatic Light

Some basic error sources, among them the size of the lightspot, filter cut-off and stray light in the monochromator, have already been addressed above. It has to be noted that the filters experience some stress due to heating, as they are placed before the monochromator, whereas they reduce the same effect for the monochromator. This could in the long run result in filter damage, but Field [52] concludes that even this is not necessarily a problem for such a system. The monochromator calibration constants were checked and optimized using a HeNe-laser (632.8 nm) and the positional error determined to be smaller than 1 nm. A check on the Xenon emission lines between 823 nm and 1262 nm showed deviations up to 3 nm from the expected values, however, in both directions, the same amount for both gratings and stronger on slightly asymmetric peaks. The disagreement is consequently attributed to the nature of the Xenon lines within a continuous spectrum. The monochromatic beam spectral bandwidth can contribute to an error at the bandgap edge of the QE or when the transmitted light is very asymmetric due to lamp emission lines. For bandwidths of 10 nm the effect is comparable to a miscalibration of less than 1 nm and therefore is only a small addition to the error from undersampling the spectrum [61].

The chopper being placed in front of the monochromator and being enclosed in a blackbox, the latter also being the case for the device under test, prevents chopped non-monochromatic light from reaching the device. Before the enclosure – during system construction – reflections from the chopper could actually reach test devices and caused a noticeable bias illumination at the chopping frequency that was not filtered in the amplifier or lock-in. Otherwise, the optical shielding from a blackbox is not generally necessary, as long as lock-in detection is used.

## Electrical Instrumentation

We are measuring with the same detection electronics in subsequent runs, whose ratio then enters the calculation according to equation 4.2. Therefore multiplicative errors in the electronics, such as an error in the amplifier gain or due to the chopped light waveform in lock-in detection, drop out [31]. DC offsets are of no concern for lock-in measurements, but have to be corrected for in continuous light mode.

### 4.3.2 Random Error

Noise in the electronics, particularly as nA- $\mu$ A currents are amplified by 5-6 orders of magnitude, mechanical vibrations, room temperature changes, etc. can contribute to the random error of the measurement. The electronics drift with operating temperature, therefore they should be allowed a warm-up period of 20-30 minutes prior to a measurement session.

## Noise

Possible mechanical vibrations are damped using rubber feet under the optical assembly. The choice of electronic components, i.e. low-noise amplifiers, use of electronic filters in the preamplifier and optimized lock-in settings, namely the used time-constant (100 or 300 ms to average 10/30 light pulses), allow to keep this part of the random error low. The blackbox and its base box are grounded to additionally serve as electromagnetic shields, but isolated from signal ground to avoid ground loops. All signal cabling outside the shields uses BNC coaxial cables.

To get an idea of the system noise, it is helpful to look at measurements over time, while leaving all parameters, especially the wavelength, unchanged. This is shown in figure 4.8. It also visualizes the advantage of using a dual-beam setup in avoiding influences from lamp instabilities and confirms our hypothesis of a constant light-splitting ratio. The upper graph depicting the measured lock-in signals of both lightpaths exhibits quite some fluctuations, the stronger ones generated by the lamp. The coefficient of variation<sup>7</sup> is at 0.53 % while the maximum deviation reaches up to 4 %. Additionally, a slight drift can be seen over time. Now looking at the ratio of the two signals, which is the factor actually entering our measurement equation 4.2, we see a reduction in both fluctuation and drift. It

---

<sup>7</sup>The coefficient of variation being the percental standard deviation  $c_v = \sigma/\mu$ , i.e. the standard deviation  $\sigma$  divided by the mean  $\mu$ .

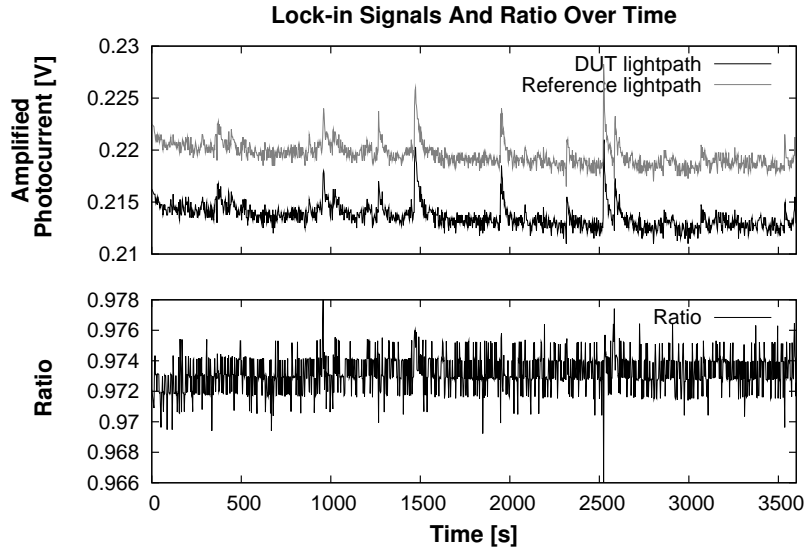


Figure 4.8: Measurements at a constant wavelength over a period of 1 hour. The upper graph shows the lock-in signals (photocurrents converted to amplified voltages) of the two lightpaths, while the lower graph shows their ratio over time. Obviously, fluctuation and drift are strongly reduced in the ratio.

can actually be seen that the fluctuations in the ratio amount to only a few discrete values. The singular maximum deviation located at around 2500 s is 0.8 %, whereas the coefficient of variation lies at 0.12 %.

Accordingly, the noise part of the random error can be quantified and lies at 0.5 % when using the triple coefficient of variation to include 99.7 % of a normal distribution and error propagation to account for two ratios entering the calculation. Using the digital multimeters for detection an average of 5 to 10 values will give a comparable random error as with optimized lock-in settings. Towards the edges of the QE curve, where the signal is reduced, the noise will rise to twice or three times this value.

### Temperature Variations

The performance of semiconductor-based detectors is dependent on temperature. For monochromatic illumination, the delivered light power is low enough for device heating to be negligible. Under white light bias a heating of the test device could occur. Care has to be taken not to use too strong bias, conflicting with the desire to simulate “real” operating conditions. No temperature control for the device under test has so far been installed. Besides the illumination induced heating,

variations in room temperature are a possible error source. Room temperature can also be an influence affecting the mechanical alignment of the optics. Thus it should be kept close to the calibration temperature of 25 °C.

### Spatial Variations

As we only measure the response of a small spot on a laboratory solar cell, there could be an effect due to spatial inhomogeneities. It will be shown in section 4.4 that this is actually the case for dye-sensitized cells. Concerning Cu(In,Ga)Se<sub>2</sub>-absorber based cells studies using light beam induced current (LBIC) measurements, a kind of QE extended for spatially resolved measurements with  $\mu\text{m}$ -sized lightspots, show that this is of no concern for our spot-size (1 mm) as we already average over a sufficiently large area [29, 62].

### 4.3.3 Reproducibility

To investigate the reproducibility of measurements with the system, a kind of experimental view on the random error, two CIGS cells were measured with different system calibrations over a period of a few months. One of the cells was buffered with CdS, the other with the alternative buffer In<sub>2</sub>S<sub>3</sub> [63]. The results for some of the measurements are plotted in figure 4.9. In the visible region, the curves are slightly fanned out, but generally stay rather close together. A very good quantitative marker for the agreement is the short circuit current density calculated from

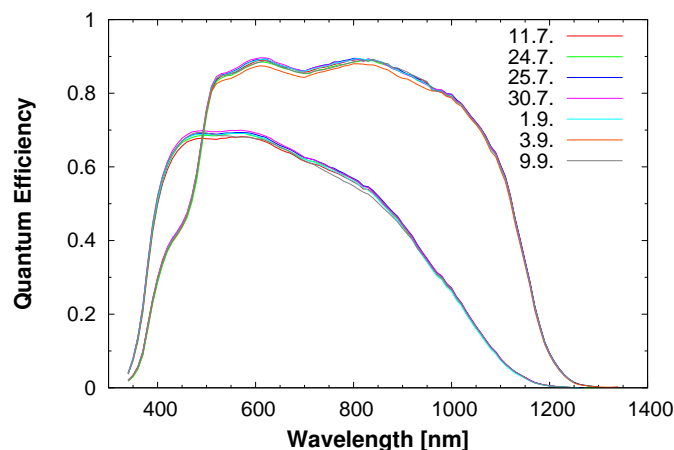


Figure 4.9: Reproducibility of QE measurements for the f88CdS-1 and f88In<sub>2</sub>S<sub>3</sub>-1 cells [63] measured on different days.

the QE. Looking at the  $J_{SC}$  values from the various measurements, they deviate up to 1 % from their mean, while the maximum and minimum are almost 2 % apart. Room temperature could be a possible factor leading to this. For repeated calibrations within one day much less spread of values is usually found. For specific comparisons of cells, it is therefore advisable to measure them in one run.

### 4.3.4 Intercomparison

Comparisons of photovoltaic performance measurements are carried out every few years by major international laboratories. The PEP'93 round robin for example showed an overall standard deviation below 2 % for a set of silicon reference cells, while an additional set with different PV technologies exhibited a larger spread in the results [64]. From this comparison the SI-traceable World Photovoltaic Scale

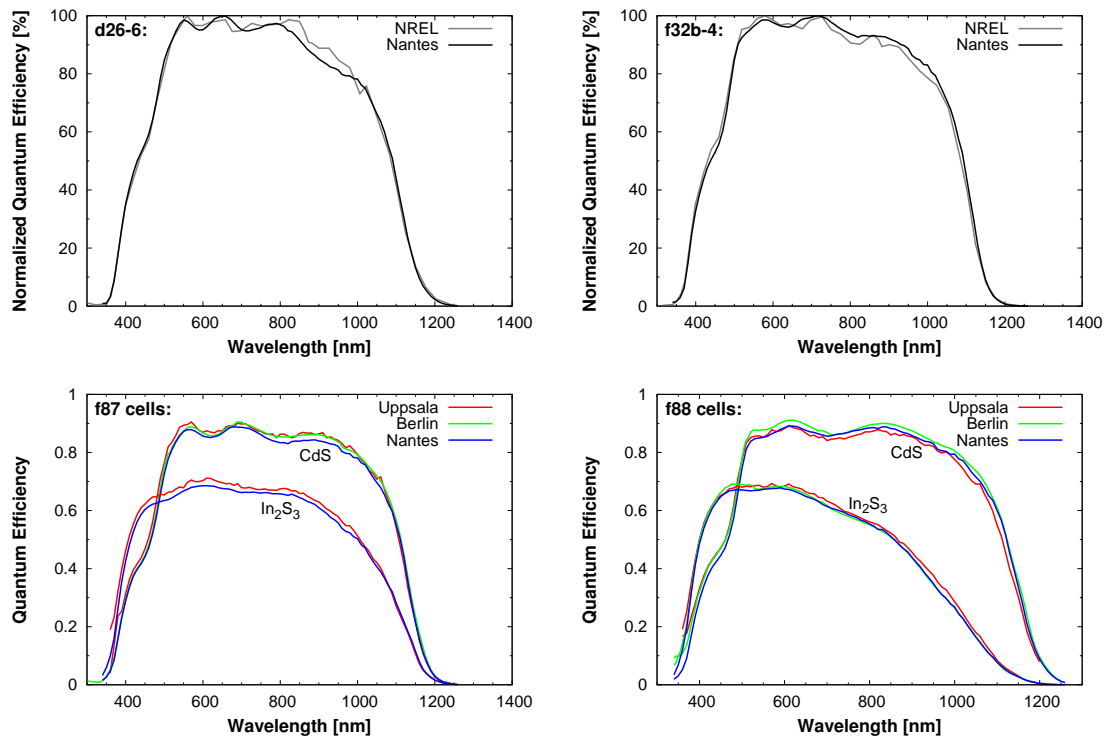


Figure 4.10: Intercomparison of QE measurements. The *upper graphs* show normalized QE curves for the d26-6 and f32b-4 cells measured in Nantes and at NREL. The *lower graphs* show a comparison of 4 cells measured in Nantes, at the Ångström Solar Center Uppsala and at the Helmholtz-Zentrum Berlin (SE2). To the left are the f87 and to the right f88 cells, each in a CdS and  $\text{In}_2\text{S}_3$  buffered version.

Table 4.2: Short circuit current densities  $J_{SC}$  [mA/cm<sup>2</sup>] calculated from Nantes and NREL measurements given together with the deviations of the Nantes values from NREL:  $\Delta = (J_{SC}^{\text{NREL}} - J_{SC}^{\text{Nantes}})/J_{SC}^{\text{NREL}}$ .

cell	Nantes	NREL	$\Delta$
d26-6	32.0	32.36	-1.1 %
f32b-4	32.58	32.6	-0.1 %

(WPVS) was developed [65], which is now recalibrated every few years at a single laboratory instead of a circulation between several institutes.

To validate measurements and get an idea of the systematic error for the new QE setup, we measured Cu(In,Ga)Se<sub>2</sub> solar cells built in Nantes using our system and had them remeasured at other laboratories. The results are depicted in figure 4.10.

For the comparison to the National Renewable Energy Laboratory (NREL) in Golden, Colorado, an institute participating in the WPVS, the curves give only a qualitative view of the shape, as NREL provided normalized curves. A good resemblance of the shape can be seen. The observable deviation can largely be attributed to system differences, as NREL measurements were made using their filter QE system. This has less sampling points and partially a larger bandpass than our grating-monochromator setup [61]. Comparing short-circuit current densities calculated from our QE (including a 2 % loss assumption due to grid coverage) and from NREL's calibrated I-V measurements we have a deviation of -1.1 % for cell d26-6 and -0.1 % for cell f32b-4<sup>8</sup>; see table 4.2 for details. Both were devices with a CdS buffer and a CIGS absorber grown in an isothermal three stage process, though in different deposition chambers.

The f87 and f88 cells with CdS and In<sub>2</sub>S<sub>3</sub> buffers were measured in Nantes, Uppsala and Berlin. Refer to Couzinié-Devy et al. [63] for details on the cells. The Ångström Solar Center in Uppsala uses a dual-beam setup with Xenon lamp, but some differences in the optical arrangement, while the group SE2 at the Helmholtz-Zentrum Berlin has a single beam system that usually switches between a Xenon lamp and a Halogen lamp. Both systems use a grating-monochromator. A comparison of  $J_{SC}$  is given in table 4.3. The Uppsala measurements show some noise from their homebuilt amplifier. For the f88 cells, the Berlin measurements are slightly higher than usual up to 650 nm due to some misadjustments in the system, whereby it was necessary to use the halogen lamp across the complete spectrum. The f87 cell with CdS buffer was remeasured with a better adjusted system, while the In<sub>2</sub>S<sub>3</sub>

<sup>8</sup>The first part of the sample identifier denotes the deposition run; the last number is the cell within a sample.

Table 4.3: Short circuit current densities  $J_{SC}$  [mA/cm<sup>2</sup>] calculated from Nantes, Uppsala and Berlin measurements given together with the deviations of the latter two laboratories from Nantes:  $\Delta(X, N) = (J_{SC}^N - J_{SC}^X)/J_{SC}^N$ .

cell	Nantes	Uppsala	$\Delta(U, N)$	Berlin	$\Delta(B, N)$
f87CdS-3	33.22	34.04	+2.5 %	33.98	+2.3 %
f87In <sub>2</sub> S <sub>3</sub> -3	25.72	26.45	+2.9 %		
f88CdS-3	34.11	33.8	-0.9 %	34.9	+2.3 %
f88In <sub>2</sub> S <sub>3</sub> -2	22.09	22.68	+2.7 %	22.22	+0.6 %

was not included in the comparison to Berlin as there it showed a reduced QE related to lower light intensity – the nonlinearity of this cell had already been observed on another occasion. Nevertheless, the shapes are well reproduced by all systems. Deviations in  $J_{SC}$  are up to 3 %, but this amount is not considerably larger than observed for the reproducibility of measurements in Nantes. Consequently, it can be concluded that none of the three quantum efficiency setups yields particularly biased results, and considering the possible sources of error discussed above, the agreement is very good.

### 4.3.5 Summary of QE Precision

A wide range of systematic and random error sources were discussed. The systematic error is dominated by the error given for the calibrated QE of our Si and InGaAs photodiodes at 5 %. For the noise contribution to the random error an estimate of 0.5 % was obtained. Room temperature is likely to have a certain influence on the measurements as well.

To supplement this error discussion, the system’s reproducibility was analyzed and deviations up to 2 % were observed, which can serve as an indicator of random error. Consequently, for direct comparisons, it is advisable to perform measurements within one day, because much lower deviations were observed under such conditions. Furthermore, in a validation based on NREL measurements a difference of 1 % was found, while a comparison to setups at the Helmholtz-Zentrum Berlin and Ångström Solar Center in Uppsala yielded up to 3 % difference. These results give an idea of the systematic error. None of the systems seems to be particularly biased, as the deviation is almost equal to the reproducibility of measurements in Nantes. On the basis of the good comparability and reproducibility, the precision of the system is estimated at 5 %. The error for dye-sensitized solar cells lies somewhat above this, due to the lower spatial homogeneity of the cells (see also next section).

## 4.4 Continuous Illumination QE on Dye-sensitized Solar Cells

At the Université de Nantes, scientists of the CNRS laboratory Chimie et Interdisciplinarité: Synthèse, Analyse, Modélisation (CEISAM) are working on electrochemical dye-sensitized solar cells. An objective in designing the quantum efficiency system was to make it available to this research group as well.

Dye-sensitized solar cells have a completely different operating approach from semiconductor devices. Their basic design is based on dye-molecules adsorbed to  $\text{TiO}_2$ -nanoparticles submerged in an electrolyte layer between two electrodes, one of which is transparent for illumination, the other covered by a platinum layer. The wide-gap semiconductor  $\text{TiO}_2$  is “sensitized” for solar radiation by the dye. Incident radiation creates excitons (bound electron-hole pairs) in the dye. At the  $\text{TiO}_2$  interface the charges separate. The electrons are injected into the semiconductor’s conduction band and reach the external circuit through the front electrode. The dye molecule remains in an oxidized state and can be reduced by Iodide in the electrolyte, which in turn is reduced at the platinum (Pt) layer on the back electrode taking up electrons from the external circuit. More details can be found in the literature [53, 66]. Efficiencies of up to 11 % have been reported, but stability problems are persistently observed and primarily associated with the dye and electrolyte [6].

Instead of quantum efficiency (QE), scientists in this field tend to use the term incident photon-to-current conversion efficiency (IPCE). Measurements are commonly done with continuous light (DC mode), due to the slow reaction of these cells

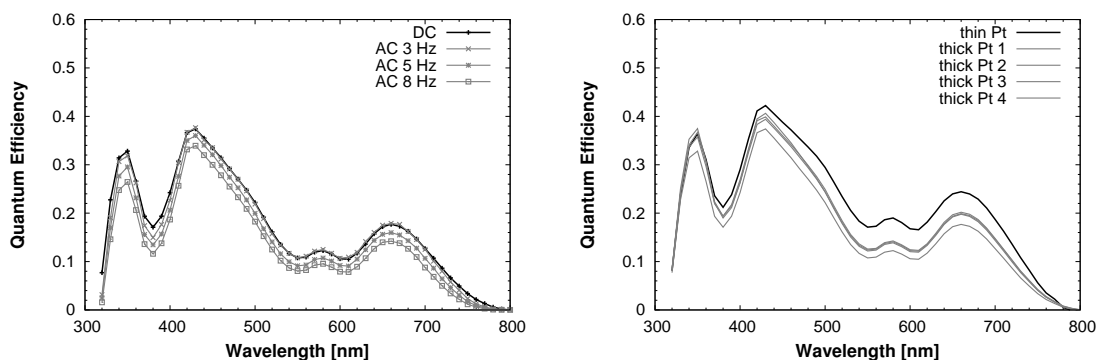


Figure 4.11: Dye-sensitized cell QE curves. *Left*: Comparison of DC mode with AC mode using different frequencies. *Right*: The same cell rebuilt with two different back electrodes (thick and thin Pt) and one of them measured at different positions on the cell to investigate the spatial inhomogeneity of the response.

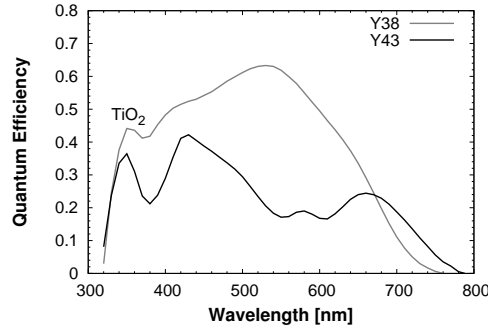


Figure 4.12: Dye-sensitized cell QE curves for two different dyes. Cell Y38 used a ruthenium complex known as N3, while the dye for cell Y43 was based on porphyrin.

on low-level pulsed light. Some studies have been performed concerning measurements under chopped light (AC) and in combination with light bias (differential method) [53, 67]. They conclude that only under sufficiently strong bias illumination and at low frequencies the response times of the cells are fast enough to measure an unreduced signal. Hohl-Ebinger et al. [67] used frequencies as low as 0.3 Hz, while Sommeling et al. [53] used 6.75 Hz and concluded that response time is also dependent on details of the cell setup.

For a cell built at the CEISAM, the response to AC illumination without bias light was analyzed in comparison to the DC mode and is shown in figure 4.11. The figure also shows an investigation of the same cell's spatial uniformity. The DC mode gives reliable results. For the chopped light measurements, it is clear that only the measurement at 3 Hz comes close to the measurements at the same spot under continuous illumination. Our chopper, however, is recommended for use down to 5 Hz only. Using bias illumination might be a feasible option, but still this might not work well for all cells. The spatial variation in measured intensities is not negligible and in the sample case extends up to a difference of 12 % in  $J_{SC}$ . Therefore, it is advisable when measuring dye-sensitized cells to look at several spot positions on the same cell. Moreover, the example of the two different Pt electrodes shows the influence of such a design feature on the current yield. To illustrate the major influence of the dye on the spectral response, figure 4.12 shows two cells using different dyes. Cell Y38 was built using cis-Dithiocyanatobis(2,2'-bipyridyl-4,4'-dicarboxylic acid)ruthenium(II) also known as N3. Cell Y43 was made with a porphyrin based dye, metallated with Zn(II), and substituted on one meso position by a cyano-propencarboxylic acid unit. The differences in absorption of the dyes manifest themselves in the QE; a peak from TiO<sub>2</sub> is visible in both curves.

It was established that the system allows QE measurements of dye-sensitized solar cells using the specially added DC mode when taking into account the larger error due to spatial inhomogeneity of the cells.

# 5 Effects of Varying Cu Supply in Three-stage Absorber Growth

The parameter investigated in this chapter is the amount of copper provided during the second stage of a three-stage co-evaporation deposition of  $\text{Cu}_y\text{In}_{1-x}\text{Ga}_x\text{Se}_2$  for solar cells, i.e. the magnitude of the temporary Cu-richness of the material is varied. Even though I did not myself deposit the absorbers and fabricate the cells, details on the absorber growth and monitoring by end point detection are given for clarity. This is followed by results from the characterization of the material's surface, composition and structure, which are discussed together with a growth model. Solar cells with a CdS buffer have been fabricated from these absorbers and their performance is analyzed using both current-voltage and quantum efficiency measurements; therefore, this chapter is also an application of the QE system in modulated light (AC) mode. The objective is to examine correlations between the growth, structure and morphology, as well as the device performance.

## 5.1 Growth Specifics

The  $\text{Cu}_y\text{In}_{1-x}\text{Ga}_x\text{Se}_2$  absorber layers were deposited onto Mo-coated soda lime glass (3 mm glass, 0.3  $\mu\text{m}$  Mo) by co-evaporation following an isothermal three-stage process (In+Ga+Se / Cu+Se / In+Ga+Se deposition sequence with durations  $t_1/t_2/t_3$ ) at a substrate temperature of 575 °C. Keeping the substrate temperature constant is a modification to the standard three-stage process [22]. During the three-stage process the film is temporarily Cu-rich, but the final composition is Cu-poor. Indium, gallium and copper were evaporated from alumina crucibles and selenium from a Pyrex crucible. The Cu-poor/Cu-rich/Cu-poor transitions were followed using the end point detection method (EPD). The graph in figure 5.1 shows the output power evolution during the deposition sequence. First the substrate is heated with the source shutters closed ( $t < 50$  min); the recorded output power (OP) corresponds to the power needed to heat up the soda-lime-glass/Mo substrate. After opening the shutters, the OP increases and settles at a level associated with the emissivity of Mo/ $\text{In}_x\text{Ga}_y\text{Se}$ . The emissivity remains unchanged during the 1<sup>st</sup> and 2<sup>nd</sup> stage until the film turns Cu-rich, i.e. the abrupt increase in OP after about 78 minutes is related to the Cu-poor/Cu-rich transition. When the film is Cu-rich,  $\text{Cu}_x\text{Se}$  is deposited, which is known to possess the higher emissivity visible in the OP.

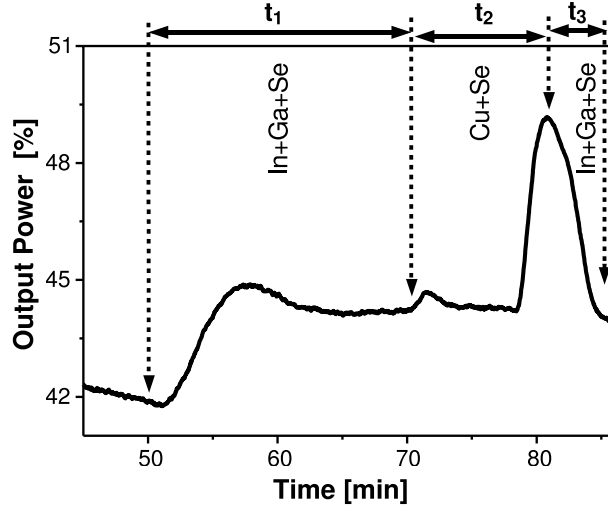


Figure 5.1: End-point detection signal evolution for the complete deposition process of sample C. The three stages are indicated; the large hump at around 80 minutes are the Cu-poor to Cu-rich and back to Cu-poor transitions.

To vary the amount of copper delivered during the growth process, the duration  $t_2$  of the 2<sup>nd</sup>-stage has been varied for six depositions that will be named A through F. Consequently, to pass back to an overall Cu-poor composition,  $t_3$  is adjusted accordingly. Therefore, assuming constant Cu, In and Ga fluxes, the Cu/(In+Ga) ratio at the end of the 2<sup>nd</sup>-stage, referred to as  $y_{nd}$ , can be estimated by

$$y_{nd} = \frac{Cu}{In + Ga} = \frac{t_1 + t_3}{t_1} \cdot y \quad (5.1)$$

with  $y = 0.91$  signifying the mean final Cu/(In+Ga) ratio for our samples, which is determined by EDX (table 5.2), while  $t_1$  and  $t_3$  indicate the durations of the 1<sup>st</sup>-stage and 3<sup>rd</sup>-stage, respectively; see figure 5.1. In figure 5.2, the heater output power between the onset of emissivity, corresponding to the Cu-poor/Cu-rich transition, and the end of the process is shown; it illustrates how the duration of the Cu-rich sequence is progressively increased from run A to run F. The inset indicates the  $y_{nd}$  value obtained from the output power curves for the respective processes according to equation 5.1, i.e. it quantifies the Cu-richness which was temporarily attained. These values agree with those expected from Kessler et al. [23], who estimated the Cu/(In+Ga) ratio to be 1.1 at the top of the output power onset observed between 79 and 83 min in figure 5.2. One can, additionally, observe an almost linear increase of the output power at the end of the process for samples D, E and F. This increase in emissivity might be a result of increased surface area – the morphology will be analyzed in the next section.

All of the solar cells investigated in this study are buffered with a standard chemical bath deposited (CBD)CdS ( $\sim 30$  nm). The window layer consists of a

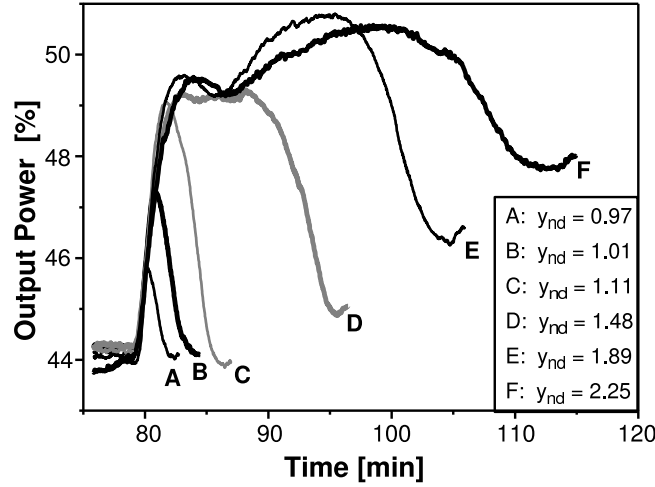


Figure 5.2: End point detection signal evolution for the Cu-poor/Cu-rich/Cu-poor transitions given in comparison for the different samples labeled A-F. The inset gives the calculated Cu/(In+Ga) ratio at the end of the 2<sup>nd</sup> stage,  $y_{nd}$ .

sputtered ZnO/ZnO:Al bilayer ( $\sim 0.2/0.3-0.4 \mu\text{m}$ ). The samples have been divided into cells of  $0.5 \text{ cm}^2$  by mechanical scribing. For contact and to ensure current collection, Ni/Al grids designed for the cells have been deposited. Anti-reflection coatings have not been applied.

## 5.2 Surface and Bulk Analysis

The samples that will be analyzed in the following are labeled A through F in the order of increasing Cu-richness at the end of the second deposition stage ( $y_{nd}$ ), as described above. In this section, the correlation between the duration of the Cu-rich phase during deposition and the films' surface morphology and composition is investigated; the techniques from material physics used here are described in appendix A. The first part of this section will focus on the morphology and is based on SEM and AFM observations. Afterwards, EDX, XRD and SIMS measurements are presented for further material analysis and discussed in conjunction with a growth model for three-stage deposition of CIGS thin-films.

### 5.2.1 Absorber Surface

The increase in sample emissivity at the end of the growth observed in figure 5.2 for depositions D through F suggests an explanation through an increase in sur-

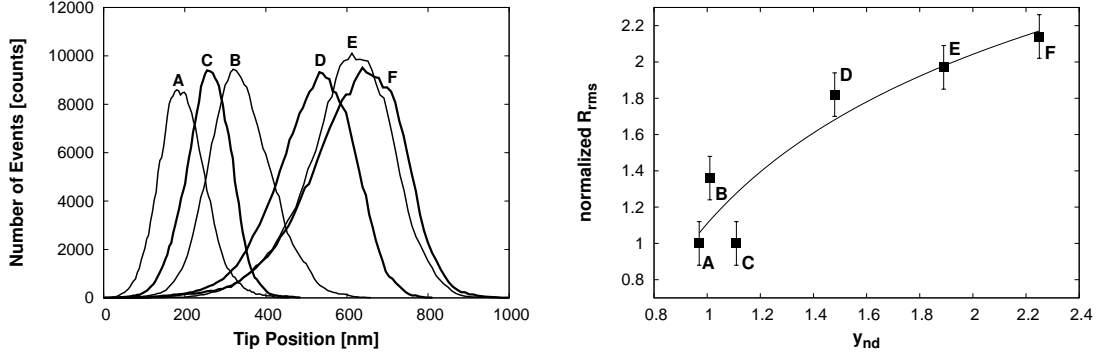


Figure 5.3: Histograms of the tip heights recorded by the AFM are shown in the *left* graph; zero is set to the deepest point measured. The *right* graph shows the resulting root-mean-square roughness  $R_{rms}$  normalized to the smoothest sample against  $y_{nd}$ , the Cu/(In+Ga) ratio at the end of the 2<sup>nd</sup> stage.

face area, i.e. rougher surfaces. Such a correlation between the Cu-richness attained during the process and the absorber morphology is obvious when looking at the SEM micrographs depicted in figure 5.4. From A through F the surface gets rougher. Particularly, the number, width and depth of crevices at the grain boundaries progressively increases from sample A through F; the same is the case for the diameter of the surface grain structure. Additionally, the absorber thickness increases for the rougher films, which is a result of the longer deposition time when increasing the duration of the 2<sup>nd</sup> and 3<sup>rd</sup> stages. All absorbers are thick enough ( $> 1.5 \mu\text{m}$ ) that transmission is negligible. In order to further investigate the roughness of the films and check whether it can be correlated to the parameter  $y_{nd}$  from the previous section, all of the samples have been studied by AFM. Histograms of the tip heights recorded with the AFM are shown in the left half of figure 5.3, where the widths of the distributions confirm the gradual increase in roughness, except for samples B and C. To make this clearer, the relation between the normalized root-mean-square roughness  $R_{rms}$  (from AFM, table 5.1) and  $y_{nd}$  is

Table 5.1: Roughness parameters from AFM in order of increasing roughness: The root-mean-square roughness  $R_{rms}$  and the area ratio, i.e. surface area  $A_x$  to flat surface  $A_{flat}$ . Values are an average of two AFM scans per sample.

Sample	A	C	B	D	E	F
$y_{nd}$	0.97	1.11	1.01	1.48	1.89	2.25
$R_{rms}$ [nm] $\pm 6$	52	52	70	94	102	111
$A_x/A_{flat} \pm 0.02$	1.11	1.11	1.15	1.2	1.23	1.31

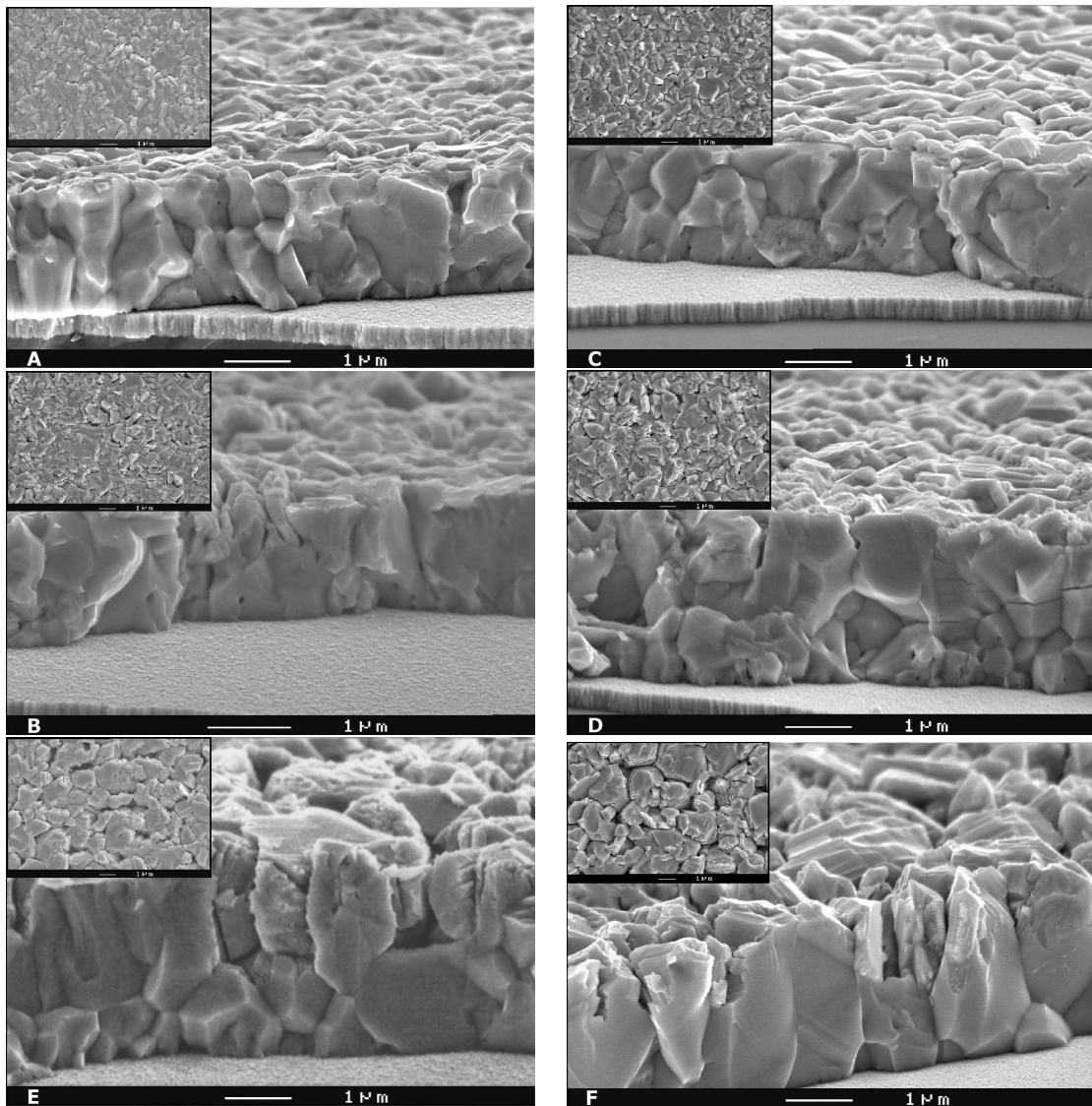


Figure 5.4: SEM images showing the evolution of absorber morphology in the order of increasing roughness (A,C,B,D,E,F). Both tilted cross-sections and plan views (insets) are given. One can clearly recognize the appearance of crevices at the grain boundaries that deepen and broaden towards film F.

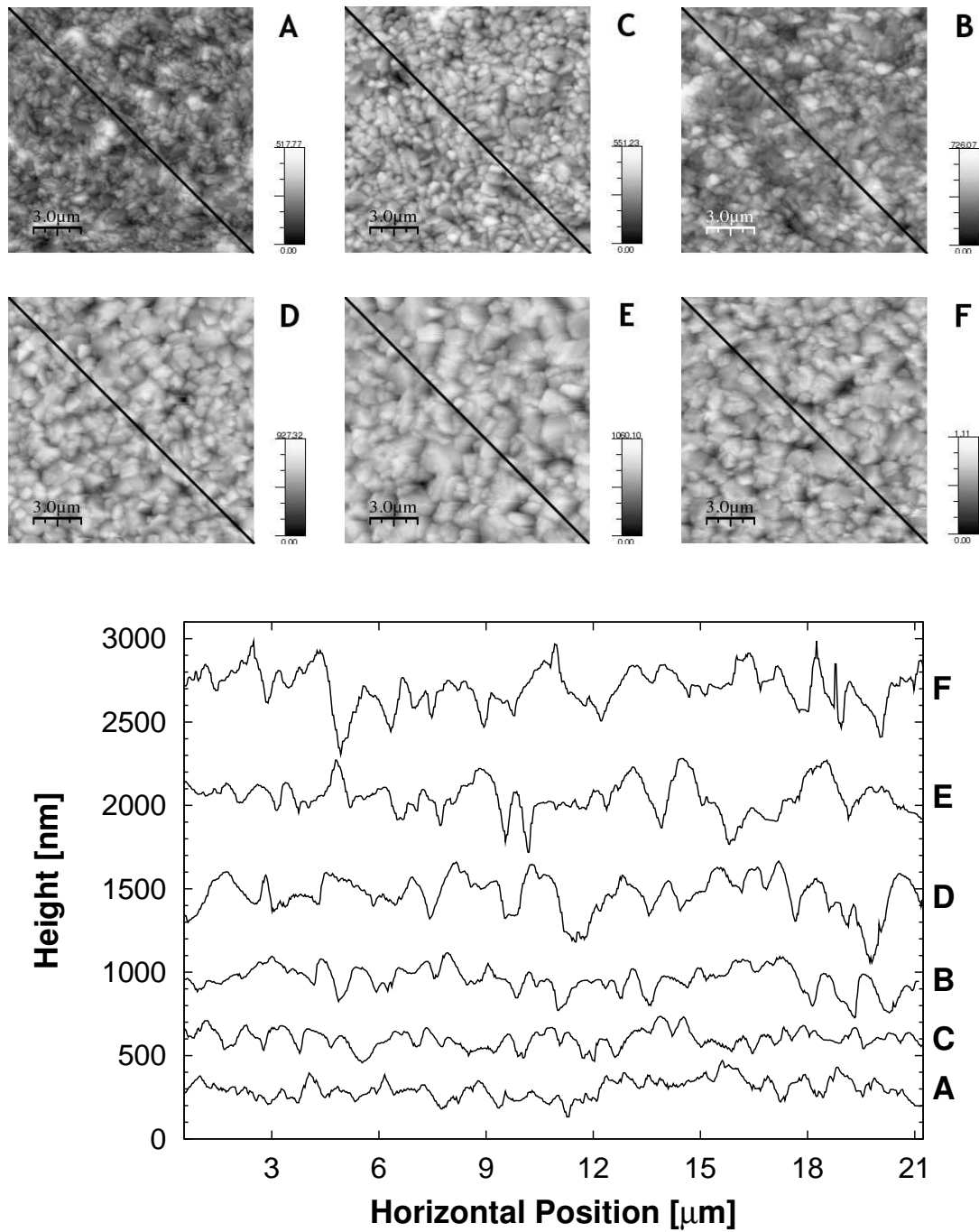


Figure 5.5: AFM images (*top*) and extracted line profiles (*bottom*) in the order of increasing roughness (table 5.1). The diagonal line used for the line profile extraction is marked in the images. For better comparability, overlapping of lines was avoided by vertical offsets – tic spacing on the y-axis is 100 nm. Note that the vertical and horizontal scales are not the same. The increase both in crevice depth and spacing is clearly visible.

added on the right side of figure 5.3. The order of progressing roughness is actually A, C, B, D, E, F. To correlate further measurements to the morphology, this order will be used. In the histograms, the broadening of the left flanks for samples D, E and F is another indicator of the deep crevices observed in the SEM; however, in SEM cross-sections the crevices show depths up to  $1.2 \mu\text{m}$ , while the base width of the histograms reaches only  $0.95 \mu\text{m}$ . This artefact can be explained by the nature of the AFM measurements: obviously the AFM-tip does not completely enter the deepest crevices in the rougher samples.

Besides  $R_{rms}$ , the ratio of the absorber surface area  $A_x$  to the area of a flat surface of same dimension  $A_{flat}$  has been extracted from the AFM data. This ratio shows only a modest increase, table 5.1. This is in part an artefact of the insufficient representation of deep crevices in the AFM data, but also an effect of the grain size increasing parallel to the crevice depth. Figure 5.5 (bottom) illustrates this with section line profiles from the AFM: from sample A through F the crevices get significantly deeper, but also their horizontal distance increases – confirming the SEM observation of larger surface grain diameter. CIGS grains are approximately spherical on the surface [68]: When their radius increases, also the depth of crevices between them should increase, which is what we observe. Concerning the emissivity, crevices will not contribute to its increase, as most of the emission will be reabsorbed on the opposite side of the crevice. However, as we have seen, the crevices are not completely represented in the AFM data and the relative increase of area (table 5.1) is larger than that of the final output power (figure 5.2). Consequently, the rise of the output power at the end of the deposition for samples D through F most likely results from a larger surface area in these samples.

### 5.2.2 Absorber Bulk Composition and Growth Model

Compositional measurements have been performed on the CIGS absorbers to ensure that no major variations occur and affect the device parameters. As the copper to group III ratio,  $\text{Cu}/(\text{In}+\text{Ga})$ , and the gallium content,  $\text{Ga}/(\text{In}+\text{Ga})$ , are the most significant compositional parameters; they are determined by energy dispersive x-ray spectroscopy (EDX). Structural information is obtained from x-ray diffraction measurements (XRD), while secondary ion mass spectrometry (SIMS) yields information on the vertical elemental profiles in the absorber. The SIMS measurements will be discussed in relation to the growth model for three-stage co-evaporation of CIGS given by Gabor [69].

The EDX results are summarized in table 5.2. The values for the  $\text{Cu}/(\text{In}+\text{Ga})$  ratio group around  $y = 0.91$ , although, samples B, D & E deviate up to 0.05. The

Table 5.2: Compositional ratios of the  $\text{Cu}_y\text{In}_{1-x}\text{Ga}_x\text{Se}_2$  as measured by EDX (ordered according to table 5.1). The values for each sample are an average over 2-3 EDX measurements. The deviation of these repeated measurements per sample is almost of the same order as the deviation between the samples.

Sample	A	C	B	D	E	F	
$y = \text{Cu}/(\text{In}+\text{Ga})$ [ $\pm 0.01$ ]	0.89	0.89	0.86	0.95	0.96	0.9	0.91
$x = \text{Ga}/(\text{In}+\text{Ga})$ [ $\pm 0.03$ ]	0.2	0.2	0.16	0.21	0.22	0.25	0.21

$\text{Ga}/(\text{In}+\text{Ga})$  ratio shows an average of  $x = 0.21$ , with deviations up to 0.05 for samples B & F.

The CIGS peaks from x-ray diffraction (XRD) measurements performed on samples A, D and F are given in figure 5.6 together with a complete XRD scan for sample D. The broader left flank of the peaks for sample A is an indicator of a slightly increased gallium gradient in this cell – a possible explanation for this could be that Ga diffusion (see growth model below) is inhibited by the sample never reaching overall Cu-richness ( $y_{nd} = 0.97$ ; table 5.1). The offset between the peaks could result from the small differences in Ga content. All samples have a preferred (112) orientation. Looking at the ratio of the (220) (204) to (112) orientations via the integrated peak areas, we also have slight variations (0.45 for A, 0.32 for D, 0.42 for F); nevertheless, this is less than observed in other studies and not expected to have a significant influence on device performance [70].

Additionally, the vertical composition profile of the CIGS was analyzed on two samples (B and D) employing secondary ion mass spectrometry (SIMS); this is shown in figure 5.7. The elemental profiles appear similar, except for the lower Ga signal in sample B, as expected from the EDX measurements; the  $\text{Ga}(\text{B})/\text{Ga}(\text{D})$  ratio lies a little lower with SIMS than with EDX (0.7 instead of 0.8), however, the change in SIMS signal intensity cannot be directly correlated to the change in concentration for elements present above the dilute limit of  $\sim 1$  at. % [71]. All signals drop close to the Mo back contact. The Cu signal is also reduced at the front surface, indicating a Cu depleted region, as is commonly observed in CIGS [25, 72]. The most interesting observation, however, is the slight decrease of the Cu and Ga contents up to about  $1.4 \mu\text{m}$  that is completely parallel for both samples, while subsequently the signals for sample B rise much faster than for sample D. Due to the different thickness of the two samples, they reach similar final values. The In signals are somewhat elevated in the region of reduced Cu and Ga content. In fact, the evolution of the In and Ga signals reveals a double Ga gradient that is attributed to the three-stage process in the growth model of Gabor [69], which can be divided into five steps:

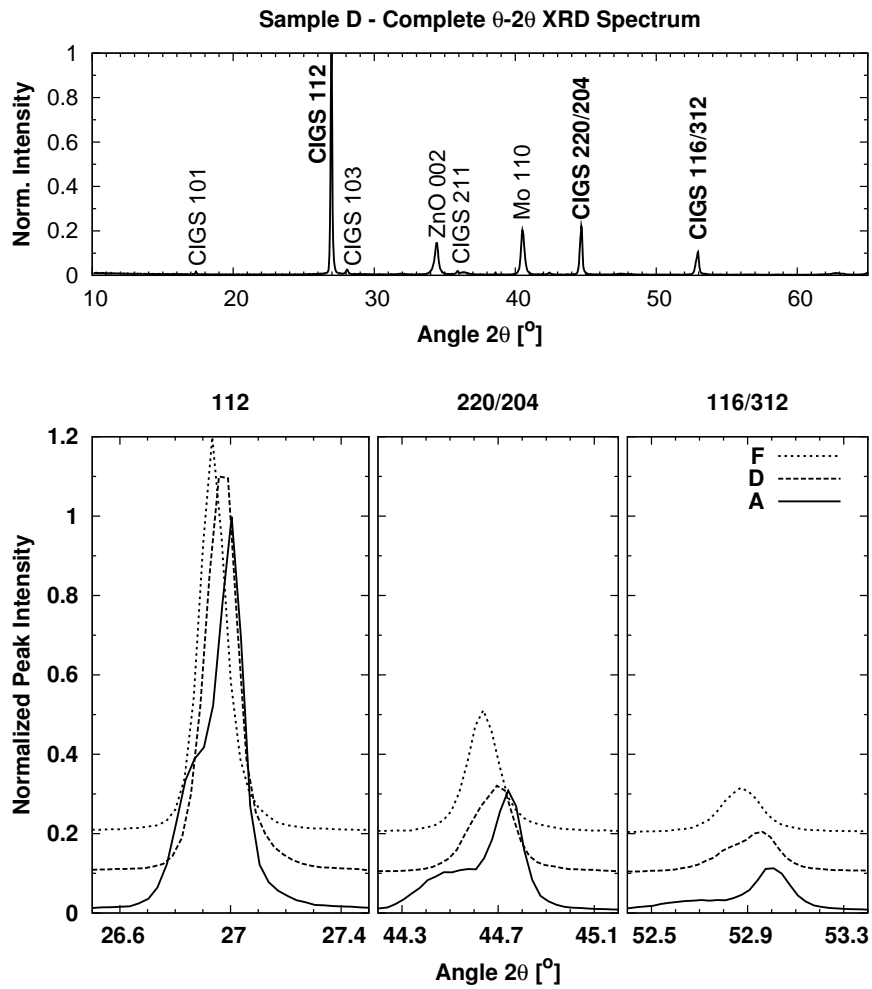


Figure 5.6: *Top*: Normalized XRD scan on a CIGS solar cell for sample D; the visible peaks are labeled. *Bottom*: The (112), (220) (204) and (116) (312)  $\text{Cu}(\text{In,Ga})\text{Se}_2$  peaks in XRD measurements for samples A, D and F. The spectra are normalized to the (112) peak and for D and F shifted vertically for clarity.

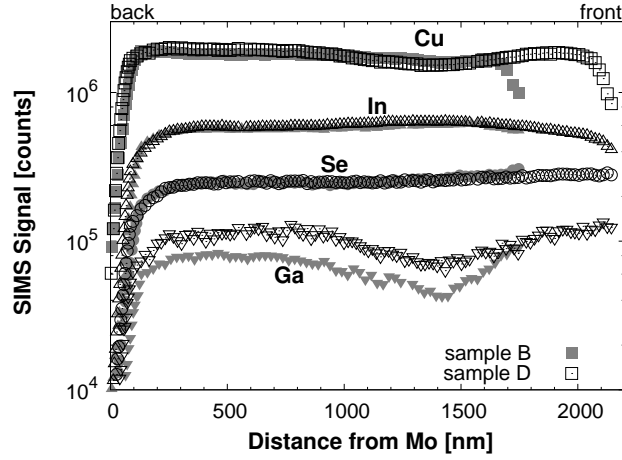


Figure 5.7: SIMS depth profiles for samples B and D plotted from back (Mo-side,  $x = 0$ ) to front. The Cu, Se, In and Ga signals are given for each; for In and Ga they were scaled by a factor 0.5 to avoid overlap with other signals in the graph. The x-axis was rescaled to the thickness obtained from cross-sectional SEM.

- (i) First the In, Ga and Se are deposited forming a  $\text{Ga}_x\text{In}_y\text{Se}$  precursor (first stage).
- (ii) When the group III evaporation is stopped and Cu is delivered (second stage),  $\text{Cu}(\text{In,Ga})\text{Se}_2$  forms through the indiffusion of Cu into the  $\text{Ga}_x\text{In}_y\text{Se}$  precursor and the outdiffusion of In and Ga towards the surface. The diffusion rates of In and Ga differ; the former diffuses faster, which causes the decrease in Ga content visible in the SIMS profiles ('bulk gradient').
- (iii) When the film becomes Cu-rich, a  $\text{Cu}_x\text{Se}$  precursor is deposited on top of the  $\text{Cu}(\text{In,Ga})\text{Se}_2$  during the continuation of the second stage.
- (iv) In the third stage the  $\text{Cu}_x\text{Se}$  reacts with In and Ga now provided once more to form additional  $\text{Cu}(\text{In,Ga})\text{Se}_2$ .
- (v) After stoichiometry is reached again, the additional In and Ga drives the layer to a overall Cu-poor composition – the diffusion from the top now reversing the gradient in comparison to (ii) and leading to a 'surface gradient'.

From the SIMS analysis and the growth model we can draw the conclusion that the elemental profiles are shaped independent of  $y_{nd}$  throughout the lower (first deposited)  $1.4 \mu\text{m}$  of the CIGS material. Note that this first section of the layers results from the growth prior to the sample being Cu-rich (1<sup>st</sup> and part of 2<sup>nd</sup> stage; growth steps (i) and (ii)). Consequently, the upper part of the film, the second section, depends on the continuation of the 2<sup>nd</sup> stage after the sample

becomes Cu-rich (growth step (iii)); the longer this step, the thicker the film and the flatter the Ga profile near the surface. This change in surface gradient can result in differences in conduction band bending close to the interface and could have an effect on device performance. Actually, we already observed the increase in thickness in the SEM pictures, and a further look shows that the crevice-free section of the films is always of comparable thickness (around  $1.4 \mu\text{m}$ ), while the part of the grains divided by crevices increases with  $y_{nd}$ . This supports the conclusion that two sections are grown, the first of which remains unchanged while  $y_{nd}$  is varied. Consequently, the growth of the second section influences the observed difference in surface morphology. The Cu enrichment process of a group III selenide precursor (step (ii)) is known to lead to highly smooth and compact CIGS films with small grains [73], however, the device performance resulting from this kind of absorber is only moderate. The second section growth can be related to the CURO (copper-rich then off) process, which is known to lead to crevices between the grains [73]. The particularity of the present case lies in the  $\text{Cu}/(\text{In}+\text{Ga})$  ratio tending to infinity at the beginning of the third stage, i.e. we have a  $\text{Cu}_x\text{Se}$  precursor reacting with In and Ga, which should lead to films with crevices as deep as the grains' height according to Kessler et al. [20]. Their interpretation suggests that during step (iv) the  $\text{Cu}(\text{In},\text{Ga})\text{Se}_2$  grows on top of the grains from the first section. While the  $\text{Cu}_x\text{Se}$  is gradually consumed during the process, it remains at the grain boundaries of the new-grown  $\text{Cu}(\text{In},\text{Ga})\text{Se}_2$  in a quasi-liquid phase – this is where the crevices then form. The increase in grain size has been attributed to a recrystallisation during the Cu-rich regime [20, 69]. This way it is possible to explain our observation that the surface morphology of the films is directly correlated to the length of the Cu-rich phase, which determines the amount of  $\text{Cu}_x\text{Se}$  segregated during the deposition.

### 5.2.3 Summary of Surface and Material Characteristics

The duration of the Cu flux and therefore the Cu-rich interval during the deposition have been varied. This is characterized by the ratio  $y_{nd} = \text{Cu}/(\text{In} + \text{Ga})$  at the end of the second stage determined from end point detection (EPD). An increase in final sample emissivity for large  $y_{nd}$  is likely to result from rougher morphology, as observed by SEM and AFM. The increase in roughness for the investigated samples is found to follow the sequence A, C, B, D, E, F. However, while the root-mean-square roughness  $R_{rms}$  increases, also the crevices between the surface grains get deeper.

The CIGS material composition and structure show certain variations in EDX and XRD measurements, but no correlation to  $y_{nd}$ . These material variations are within the scope of the used deposition system's reproducibility and from their magnitude no major influence on the resulting device performance is expected.

SIMS shows a variation of slope for the surface region Ga gradient and increasing absorber thickness, as only  $y_{nd}$  related material characteristics apart from the roughness. More generally, the SIMS measurements reveal a two section growth of the absorber for the three-stage process that explains the observed crevices in the upper part. According to Gabor [69] the growth can be divided into five steps. The lower section is completely independent of  $y_{nd}$  and is formed during steps (i) and (ii). During the remaining three steps the upper section is grown; this is correlated to  $y_{nd}$  – which effectively is proportional to the amount of  $\text{Cu}_x\text{Se}$  deposited in step (iii) – and responsible for the observed change in morphology and especially the deep crevices.

## 5.3 Photoelectric Characterization

The analysis of the films shows that the composition of the CIGS is almost unchanged; most differences observed in the device parameters can, therefore, be related to the varying absorber surface morphology and its consequences on the interface formation. Current-voltage and quantum efficiency measurements have been performed on 5 cells per sample to get more representative values. For each sample, cells that were at the same position during absorber growth have been chosen in measuring the parameters to improve comparability by reducing influences from possible gradients in the material composition related to source alignment in the co-evaporation process; deviations from this principle will be mentioned when they seem to influence the measurements.

### 5.3.1 Current-Voltage Characteristics

The device parameters ( $V_{OC}$ ,  $J_{SC}$ , FF, Efficiency) are shown in figure 5.8 following the order of increasing roughness established in the previous section (table 5.1). The cell efficiency is best for sample B, with only a half percent advantage over samples A, C and D. It drops for runs E and F.

Table 5.3: Open circuit voltage loss  $\Delta V_{OC}$  due to increased junction area according to equation 5.2:

Sample	A	C	B	D	E	F
$A_x/A_{flat}$	1.11	1.11	1.15	1.2	1.23	1.31
$\Delta V_{OC}$ [mV]	-2.7	-2.7	-3.6	-4.7	-5.4	-7.0

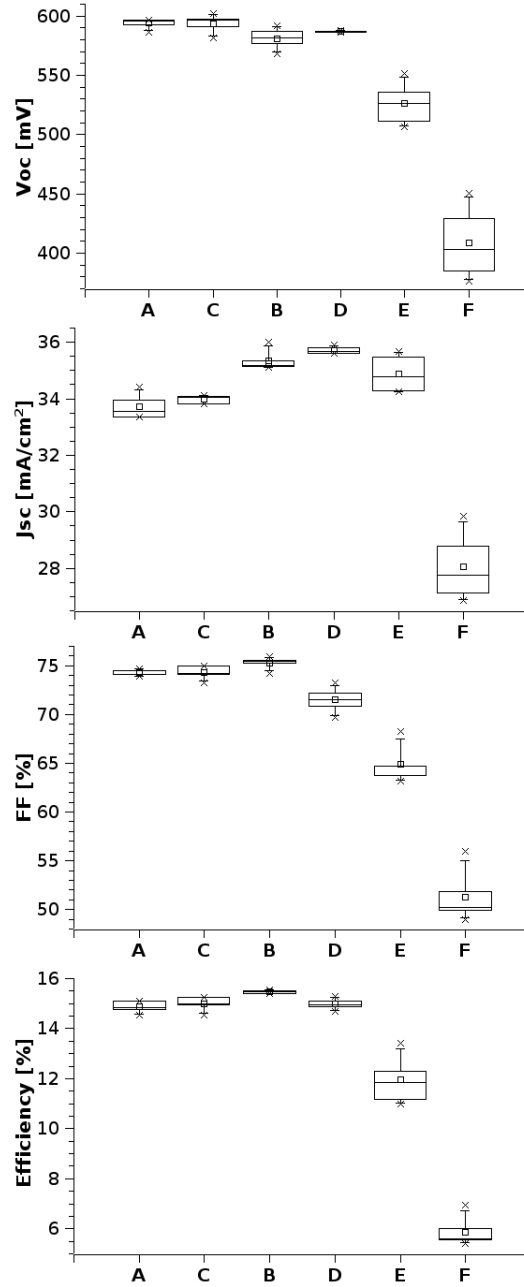


Figure 5.8: Device parameters as boxplot.  $V_{OC}$  and FF from  $I(V)$  measurements,  $J_{SC}$  from QE measurements. The box shows the quartiles and the median, the whiskers include 95 % of the data, the small square denotes the mean and the two diagonal crosses the extrema. Samples are ordered by increasing roughness (table 5.1).

Table 5.4: Parameters deduced from a single diode model (eq. 3.2) fit to light  $I(V)$  curves (average of 4-5 cells per sample); order according to roughness from table 5.1:

Sample	A	C	B	D	E	F
$A$	1.64	1.66	1.60	1.70	1.87	1.91
$R_s$ [ $\Omega$ ]	0.8	0.6	0.5	1.5	2.3	6.8
$R_{sh}$ [ $\Omega$ ]	2500	2700	2800	2100	1000	400
$J_0$ [mA/cm <sup>2</sup> ]	$8 \cdot 10^{-6}$	$7.6 \cdot 10^{-6}$	$6.7 \cdot 10^{-6}$	$2 \cdot 10^{-5}$	$2.3 \cdot 10^{-4}$	$5.4 \cdot 10^{-3}$

There is an explanation for decreasing  $V_{OC}$  with increasing roughness, resulting from the diode model for a solar cell (equation 3.3). Scaling the diode current according to the junction area  $A_x$  and the photocurrent according to the illuminated area  $A_{flat}$ , Palasantzas and Koumanakos [74] derive an expression for the dependence of the  $V_{OC}$  on the surface morphology. The change in open-circuit voltage ( $\Delta V_{OC}$  [V]) with  $A_x$  increasing in respect to  $A_{flat}$  is given as

$$\Delta V_{OC} = -\frac{kT}{q} \ln \left[ \frac{A_x}{A_{flat}} \right] \quad (5.2)$$

with the Boltzman constant  $k$  [J/K], the absolute temperature  $T$  [K] and the elementary charge  $q$  [C]. In simulations for different roughness parameters, Palasantzas and Koumanakos observed only a minor decrease in  $V_{OC}$  in the limit of low roughness and a much stronger decrease in the limit of strong roughness. Using surface ratios calculated from AFM measurements to calculate  $\Delta V_{OC}$  (table 5.3), we can conclude that this model can only explain about half of the observed decrease in  $V_{OC}$  from sample A to D, which is 10 mV. The model does not at all explain the larger decreases of 65 mV for sample E and 170 mV for sample F.

The deep crevices seen in the SEM pictures for the roughest cells (figure 5.4) make it plausible to assume that junction formation is hindered for these cells, resulting in the additional reduction of  $V_{OC}$  through interface recombination. This assumption is supported by the evolution of the diode ideality factor  $A$  derived from a fit of the one diode model (equation 3.3) to the light  $I(V)$  curves with a program written by James Connolly [75]; the results are shown in table 5.4. Generally, the ideality follows the same development as efficiency  $\eta$  and fill-factor: the best junction (low  $A$ ) is found in sample B, corresponding to the highest  $\eta$  and best FF. For the roughness increasing further (D to F), the ideality factor approaches 2, pointing to a larger influence from recombination currents. Likewise, the series resistance increases, while the shunt resistance decreases for samples E and F, both again indicators for a less well formed junction. The reduced shunt resistance indicates that usually negligible leakage currents across the junction might play a role in the roughest samples.

## 5.4 Quantum Efficiency

Quantum efficiency (QE) measurements give further information on the development of the current yield from one sample to another. This analysis will include QE measurements under voltage and light bias. A quantitative breakdown of loss mechanisms will follow the qualitative discussion of the measurements. Additionally, values for the series resistance are derived from QE under forward bias. Representative quantum efficiency curves for each sample are plotted in figure 5.9. The main differences appear in the visible and near infrared regions. Slight differences are furthermore observed in the buffer absorption and at the absorber bandgap edge. The threshold in  $J_{SC}$  for sample F, observed already in the  $I(V)$  derived parameters, is clearly due to an overall reduced quantum efficiency.

In the 500-850 nm wavelength region, a reduction of interference fringes towards rougher cells dominates, while the maxima in quantum efficiency of cells A through E all lie at 90 %. The decrease in interference in the ZnO window is well explainable with reduced smoothness of the junction, when ZnO is grown on a rougher absorber; the ZnO has smaller crystal grains and usually follows the absorber's surface structure.

Above 850 nm (near infrared), the QE continuously improves from A through D, however, not only due to the reduced interference, i.e. reflection. This is revealed by the internal quantum efficiency (IQE) calculated according to equation 3.7 and shown as inset in figure 5.9. Furthermore, reverse voltage bias during QE measurements does not affect the collection for these samples (not shown); complete collection from the absorber is therefore concluded for samples A through D. Further influences on the QE in this spectral domain that could explain the reduced QE of the smoother absorbers are free carrier absorption in the ZnO or incomplete absorption in the thinner CIGS. Likewise, the rougher interface will increase dispersion angles and thus the lightpath in the absorber. On the one hand, there is no reason to believe that the ZnO properties have changed. On the other hand incomplete absorption (CIGS transmittance) is normally negligible for absorbers thicker than 1.5  $\mu\text{m}$  [76], which is given for all samples. It is thus hard to draw any conclusions on the origin of this reflection independent loss.

For morphology E, long wavelength collection is improved under reverse voltage bias, and for morphology F, an additional improvement across the whole spectrum is obtained, as shown in figure 5.10. The reverse bias effect for long wavelengths, i.e. collection of carriers generated deep in the absorber, points to a reduced width of the space charge region (SCR) or reduced minority carrier diffusion length [32] – a change of the latter is unlikely, as the absorber composition is unchanged. It should be added, that about half of the collection loss

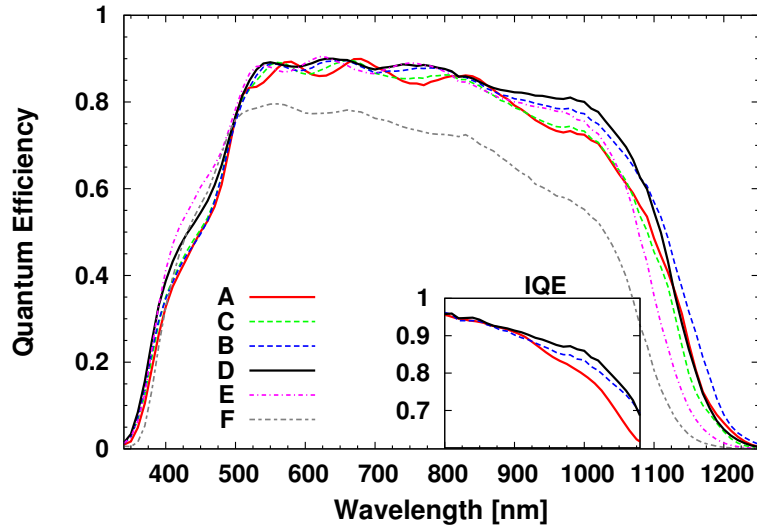


Figure 5.9: Representative QE curves for the six samples. Those having the  $J_{SC}$  closest to the mean value of a sample set have been chosen. The dispersion of the QE curves within a sample is well represented by the dispersion of  $J_{SC}$  in figure 5.8. The inset shows the infrared IQE for samples A, B and D.

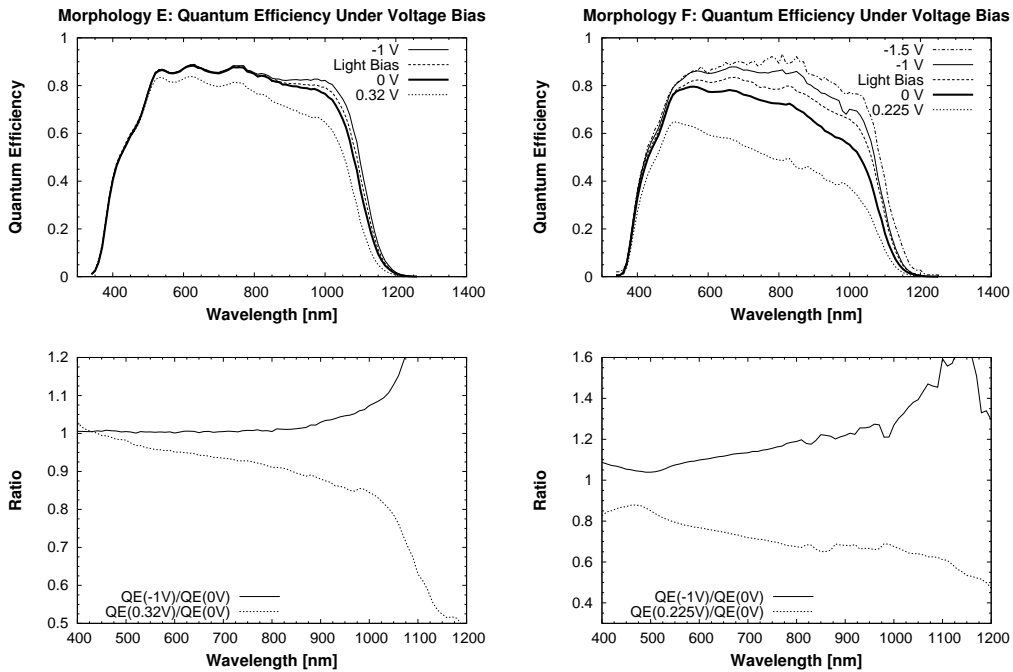


Figure 5.10: QE under voltage bias for the roughest samples E and F. The dip at 980 nm for morphology F at -1 V was an artefact in the calibration, while the higher noise at -1.5 V is a result of reduced amplification to allow the higher bias.

in sample E and also a portion of the loss in sample F are restored under light bias, indicating that under normal operating conditions the SCR in these cells is enlarged when hole traps in the CdS are filled and it becomes more n-type (section 3.2.5). The wavelength independent part of collection improvement in sample F is another evidence for the interface recombination assumed above. It could be also due to a barrier from conduction band offsets [32], however, there is no reason to assume such a decisive change in the band structure between the samples. From the change in slope of the Ga gradient concluded above, we can expect an influence on the form of the band bending. However, as long as the surface Ga content is comparable, we should not have a change in interface band offsets. Gabor [69] has simulated different surface Ga gradients, but he only varied the distance of the gradient from the front surface and not its slope. When this front gradient reaches further into the absorber than the space charge region, the band bending cannot counter the gradient's influence on the conduction band and a photocurrent barrier appears. The simulation resulted in reduced current, but at the same time in significantly improved voltage – the latter in contrast to what we observed above. In conclusion, it is unlikely that changes in the band structure play a considerable role in the differences between our devices.

Looking at the buffer region (below 500 nm), we have a slight improvement in current generation for cells D and E over the smoother samples, that from the IQE is not attributable to reduced interference. This could mean that CdS coverage is reduced for the rougher cells and more blue light is transmitted to the absorber, however, CdS deposited in a chemical bath usually exhibits a good coverage. Alternatively, collection from the buffer might be slightly improved. According to Klenk [13], the interface inversion in CIGS solar cells reduces interface recombination for electrons photogenerated in the absorber, while increasing it for holes from the buffer. A reduction of this inversion could be an explanation for the increased blue light response, as well as for part of the reduction of collection from the absorber found in the roughest cells.

Concerning the absorber bandgap  $E_g$ , the extracted values group around 1.1 eV (1130 nm). The roughest samples E and F expose a cutoff at smaller wavelengths corresponding to a change in bandgap energy of 30 meV and 45 meV, respectively. For sample E this is solely an effect of the incomplete collection of long wavelengths. Sample F additionally exhibits a small actual bandgap change resulting from a Ga gradient related to source geometry during evaporation: Compared to the other samples, cells from the opposite end of the substrate were measured. The slightly lower bandgap energy of absorber B (-15 meV) corresponds to the reduced Ga content found in the EDX measurements discussed above (table 5.2).

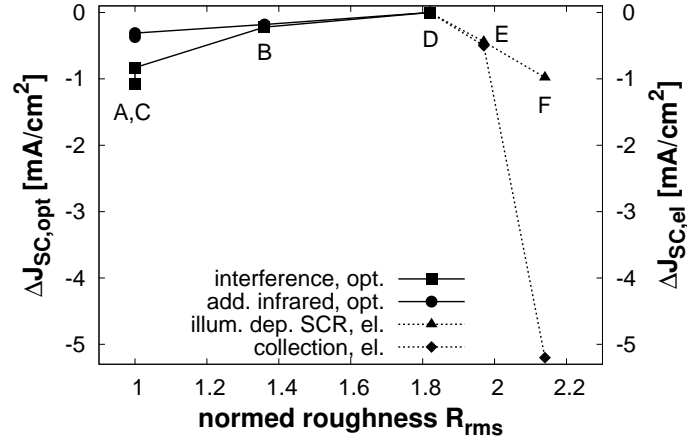


Figure 5.11: Dependence of the short-circuit current losses ( $\Delta J_{SC}$ ) on the absorber roughness. The optical losses ( $\Delta J_{SC,opt}$ ) were separated into a portion due to interference and a portion appearing in the infrared that is not reflection related. Electronic losses ( $\Delta J_{SC,el}$ ) were divided into those appearing due to an illumination dependent SCR width when no light bias is used and real collection losses.

### 5.4.1 Quantitative Analysis of Current Density Variations

The qualitative examination of quantum efficiency has shown that optical losses reduce with increasing roughness; mostly, but not completely, attributable to a lower reflection from reduced interference. It should be noted again, that anti-reflection coatings were not used. For samples E and F, collection losses take over in dominating the short-circuit current density; they originate from a reduced width of the space charge region (SCR) and increased interface recombination, both attributable to an impaired junction formation. A portion of this is, however, only an apparent effect that is rectified through a widened SCR under bias illumination. One can say, that the effects leading to improvements with increasing roughness are optical, while the effects reducing the  $J_{SC}$  when going even rougher are electronic.

The following is an attempt to separate these influences on the  $J_{SC}$ . The change in short-circuit current density ( $\Delta J_{SC}$ ) between samples can be divided into an optical and an electronic part [26]

$$\Delta J_{SC} = \Delta J_{SC,opt} + \Delta J_{SC,el} + \Delta J_{SC,mix} \quad (5.3)$$

where  $\Delta J_{SC,mix}$  is a negligible mixed term.

For the samples showing complete collection from the absorber (A through D) we have  $\Delta J_{SC,el} = 0$  and therefore  $\Delta J_{SC} = \Delta J_{SC,opt}$ ; taken in respect to the highest short-circuit current density (sample D):  $\Delta J_{SC,opt} = J_{SC}^D - J_{SC}^X$ . We calculate  $J_{SC}$

from equation 3.13 and confine our integration to the interval 500 nm to 1050 nm to leave out the effects from the buffer and bandgap region. Further, we use the IQE in the interval 800 nm to 1050 nm (inset in figure 5.9) to separate the reflection independent optical loss in the infrared from the interference loss. The results shown in figure 5.11 indicate that the slope of the optical gain reduces with increasing roughness, i.e. the improvements related to the roughness have almost saturated in sample D. Consequently, we can assume that losses in the roughest samples (E and F) are largely due to impaired collection, i.e.  $\Delta J_{SC,opt} \rightarrow 0$  and  $\Delta J_{SC} = \Delta J_{SC,el}$ . The electronic losses were calculated again using equation 3.13 from the measurements with and without bias (figure 5.10):  $\Delta J_{SC,el} = J_{SC}^{bias} - J_{SC}$ ; this gives a good idea of these losses, even though the -1/-1.5 V reverse bias does not lead to 100 % collection and we slightly underestimate the electronic losses. In figure 5.11 only the loss not rectified under light bias is plotted as collection loss, but the illumination related part is additionally given. This underlines that after a threshold close to growth condition D ( $y_{nd} = 1.48$ ) the electronic current losses quickly become more important than the optical gain.

### Extended Photocurrent Density Breakdown

This quantitative analysis can be extended to include other losses mentioned in section 3.2.1, i.e. to give a complete breakdown of the maximum possible current density. The separation of photocurrent density losses for the different samples is given in table 5.5. Most calculations are based on equations 3.5 and 3.13. If we assume a perfect quantum efficiency ( $QE(\lambda) = 1$ ) up to the observed bandgap  $E_g = 1.1$  eV, we obtain a photocurrent density of 43.2 mA/cm<sup>2</sup> under AM1.5 illumination. Additionally, we can add the observed Urbach tail; in our measurements the typical current density for the interval beyond the bandgap wavelength is 0.4 mA/cm<sup>2</sup>.

First, the grid coverage for all samples is estimated to be 2 %; equivalent to 0.9 mA/cm<sup>2</sup>. The loss resulting from reflection is calculated from measured reflection data; the portion due to interference, as derived above, is indicated. However, the reflectance measurements were not the most accurate ones and possibly somewhat elevated – this is one of the reasons why the final balances don't add up to zero. Deep penetration losses (absorber transmittance) and free carrier absorption in ZnO are not quantified – neither absorbers on glass (without molybdenum layer) to measure transmittance, nor possibilities to determine carrier densities in the ZnO, were available. As stated above, these might be reasons for the observed infrared loss. For the losses related to ZnO and CdS, reflection and observed  $J$  and the reflection equivalent current density are subtracted from the maximum possible current density for the respective intervals; from their bandgaps we attribute  $\lambda < 390$  nm to ZnO and  $\lambda = 390 - 520$  nm to CdS. The recombination of carriers

Table 5.5: Breakdown of photocurrent density  $J_L$  by separation of loss mechanisms. All values are in [mA/cm<sup>2</sup>]. The upper part gives the theoretically possible current density, while the lower part quantifies loss mechanisms and the observed photocurrent. The error in the resulting balance is attributed to inaccurate reflection measurements, underestimation of the recombination in sample F, as well as the partial neglect of ZnO free carrier absorption and incomplete CIGS absorption.

Sample	A	C	B	D	E	F
100 % QE for $E_g = 1.1$ eV	43.2	43.2	43.2	43.2	43.2	43.2
Absorption Tail	0.4	0.4	0.4	0.4	0.4	0.4
Grid cover	0.9	0.9	0.9	0.9	0.9	0.9
Reflection (Interference)	6.5 (1.1)	5.7 (0.8)	5.4 (0.2)	5 (0.1)	5.2 (0.1)	5 (0.1)
Infrared Loss	0.4	0.3	0.2	0	0	0
ZnO recombination	0.7	0.7	0.7	0.7	0.7	0.7
CdS recombination	1.8	1.8	1.8	1.6	1.4	1.4
Collection loss	0	0	0	0	0.5	5.2
Illumination nonlinearity	0	0	0	0	0.4	1
Observed photocurrent	33.7	34	35.4	35.7	34.9	28
<i>Balance</i>	<i>-0.4</i>	<i>0.2</i>	<i>-0.8</i>	<i>-0.3</i>	<i>-0.4</i>	<i>1.4</i>

created in the absorber (collection loss) and the additional loss in samples E and F associated to low level illumination are again taken from above. For sample F, the collection loss is probably underestimated – this is reflected in the resulting balance.

Comparable separations are given by Sites et al. [37, 40] and Orgassa [77]. They show that the reflection losses observed in our study are comparatively high, even if the measured values might be slightly elevated. Many scientists use anti-reflection coatings to reduce this – for example, Orgassa [77] states a reflected current density equivalent of only 0.7 mA/cm<sup>2</sup>; Sites et al. [40] give 2.2 mA/cm<sup>2</sup>, but they don't state whether an anti-reflection coating was applied. For the recombination losses in ZnO and CdS, Orgassa [77] states values close to those given here.

### 5.4.2 Series Resistance Deduced from QE

As mentioned in chapter 3.2.4, quantum efficiency measurements under forward bias are influenced by the cell's series resistance  $R_s$  and in turn allow the extraction of  $R_s$ . The extracted value will include an additional influence from the measure-

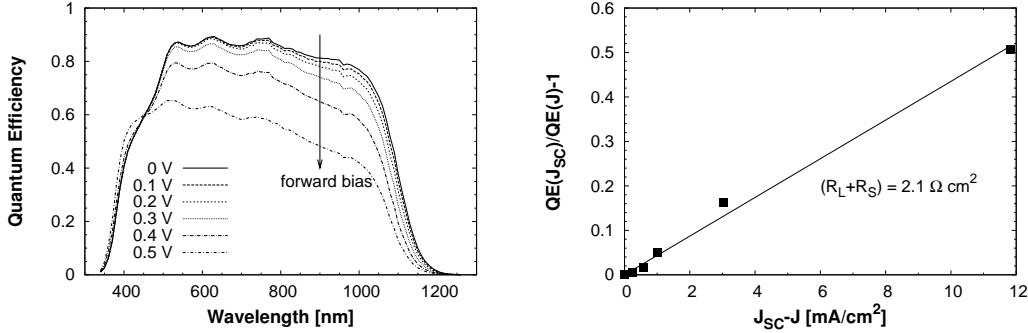


Figure 5.12: Quantum efficiency measurements under forward bias and deduction of  $R_s + R_L$  for sample E. In the *right graph*, the QE-ratio at  $\lambda = 900$  nm (marked by the arrow in the *left graph*) was plotted against the forward current density  $J_F = J_{SC} - J$ . Linear fits can be used to determine  $R_s + R_L$  using equation 5.4. The same procedure has been applied to the other samples.

ment circuit load resistance  $R_L$ , i.e. we obtain  $R_s + R_L$ . Phillips and Roy [39] start from the single diode model (equation 3.3) to derive the following formula:

$$\frac{QE(J_{SC}, \lambda)}{QE(J, \lambda)} - 1 = \frac{q}{AkT}(R_L + R_s)(J_{SC} - J) \quad (5.4)$$

where the ratio of QE at short-circuit conditions and under forward bias is related to the forward current  $J_F = J_{SC} - J$  [mA/cm²] and the sum  $R_s + R_L$  [ $\Omega \cdot \text{cm}^2$ ]. The factors are the elementary charge  $q$  [C], the diode ideality factor  $A$ , the Boltzmann constant  $k$  [J/K] and the absolute temperature  $T$  [K]. This means that the magnitude of the decrease in quantum efficiency under forward bias is related to the magnitude of the series and load resistance. A linear fit of  $QE(J_{SC})/QE(J) - 1$  plotted against  $J_{SC} - J$  [mA/cm²] allows the calculation of  $R_L + R_s$  [ $\Omega \cdot \text{cm}^2$ ]. Equation 5.4 is independent of wavelength, but is not valid for blue wavelengths, where the influence of the photoconductive buffer will be superimposed on the resistance effect.

Such a measurement and calculation has been conducted for four samples: A, D, E and F. The graphical part is exemplified in figure 5.12 for sample E. Our measurements are performed at room temperature ( $T = 300$  K);  $\lambda = 900$  nm was chosen for the quantum efficiency values (arrow in figure 5.12). The QE is integrated together with a solar spectrum according to equation 3.13 to calculate the short-circuit current density  $J_{SC}$  and the current density  $J$  under forward bias. Where photoconductive effects under forward bias distort the blue QE, the current density is approximated according to  $J = J_{\lambda > 550 \text{ nm}} \cdot J_{SC} / J_{SC, \lambda > 550 \text{ nm}}$  with the integration in eq. 3.13 refrained to the interval above 550 nm for  $J_{\lambda > 550 \text{ nm}}$ .

The results for  $R_s + R_L$  are given in table 5.6; for comparison the table again

Table 5.6: Values of  $R_s + R_L$  deduced from quantum efficiency. Additionally, the slope of the linear fit used in the calculation according to equation 5.4 is given (see also figure 5.12). The given uncertainties are only those of the fit. For comparison the value from the diode model fit to light- $I(V)$  data from table 5.4 is added and converted to  $[\Omega\cdot\text{cm}^2]$ . A third series resistance is taken from a similar fit to dark- $I(V)$  curves.

Sample	A	D	E	F
$\left(\frac{QE(J_{SC})}{QE(J)} - 1\right) / (J_{SC} - J)$ [ $\text{cm}^2/\text{A}$ ]	$106 \pm 7$	$78 \pm 7$	$43 \pm 2$	$236 \pm 11$
$R_L + R_s$ [ $\Omega\cdot\text{cm}^2$ ]	$4.7 \pm 0.3$	$3.7 \pm 0.3$	$2.1 \pm 0.1$	$11.1 \pm 0.5$
$R_s$ from light- $I(V)$ [ $\Omega\cdot\text{cm}^2$ ]	0.4	0.75	1.15	3.4
$R_s$ from dark- $I(V)$ [ $\Omega\cdot\text{cm}^2$ ]	1.08	0.52	2.64	3.84

gives  $R_s$  from fits to the light- $I(V)$  curves originally presented in table 5.4. Both methods yield values of similar order. However, assuming that  $R_L$  does not vary significantly, the changes between the samples are different. Only a higher series resistance for sample F than for the others is clear in both data sets. The strongest influence on the series resistance comes from the TCO, which conducts the current to the grid contacts. Thickness variations in the TCO or increased surface area could increase this resistance. The derivation from QE has been performed on only a single cell per sample and might therefore be less representative; the cells exhibiting the basic parameters closest to the sample average were chosen. It is important to consider the completely different measurement conditions for the QE and the  $I(V)$  to clarify why the series resistances determined are hard to compare. The current-voltage measurement was performed at 1 sun continuous illumination with a complete spectrum. In contrast, the quantum efficiency system uses an average of only 0.01 suns monochromatic illumination modulated for lock-in detection. It is most likely that these completely different operating conditions alter the series resistance, i.e. two different resistances were determined and the disagreement is not surprising. This is illustrated further by the series resistance taken from a fit to dark- $I(V)$  data, i.e. measured without illuminating the cell; although again the values are not averaged over multiple cells, the deviation from the other values for  $R_s$  is clear.

## 5.5 Another View on Interface Formation and Recombination

The data from  $I(V)$  and QE suggest that recombination at the interface is increased for the roughest sample (F). A possible explanation relates this to a less

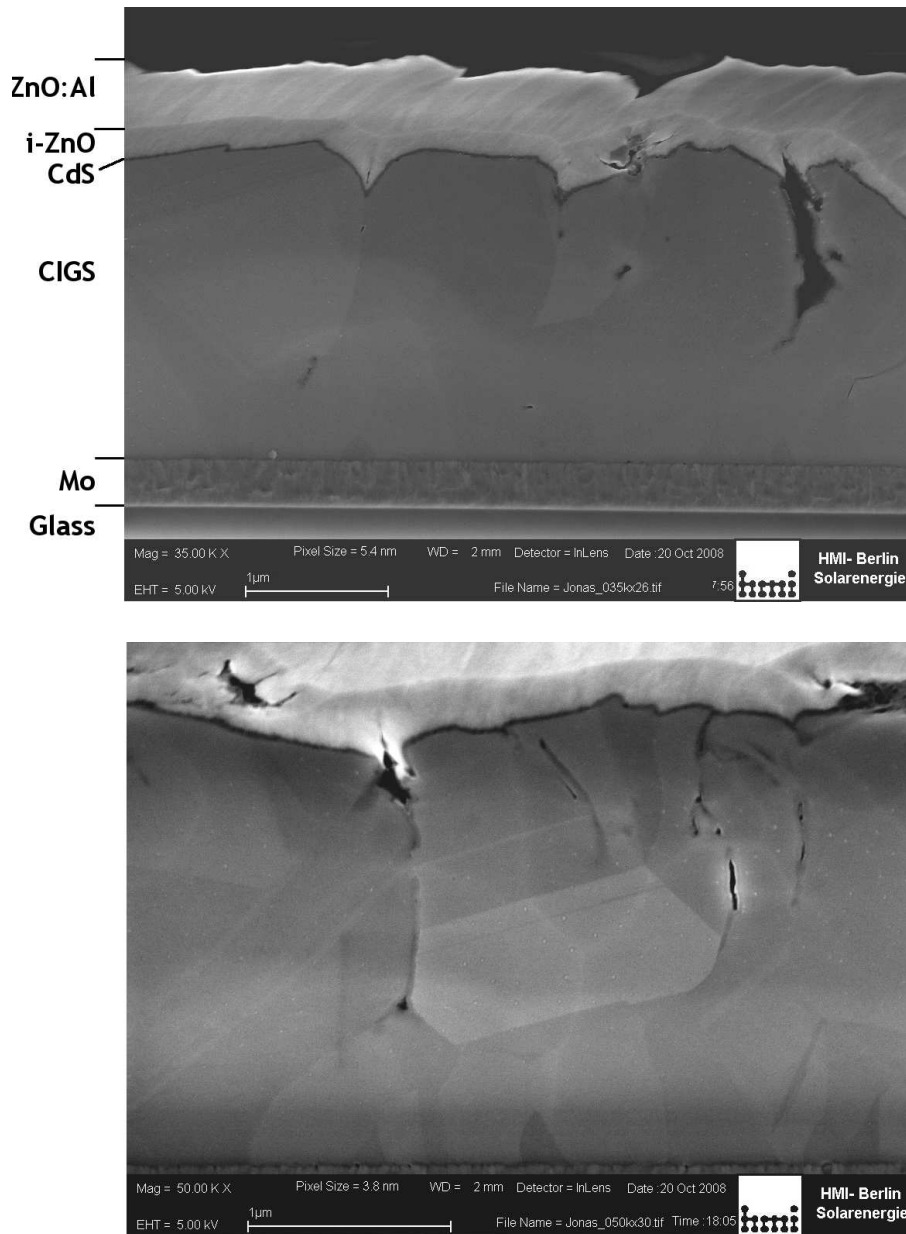


Figure 5.13: SEM micrographs of polished cross-sections for sample F. All layers from the solar cell can be distinguished: glass, Mo, CIGS, CdS, i-ZnO and ZnO:Al. (CBD)CdS (dark) can enter crevices, while the sputtered ZnO cannot. The scale bars at the bottom of the graphs denote 1  $\mu\text{m}$ .

well formed junction due to the deep crevices. This is supported by cross-sectional micrographs of a complete cell for sample F shown in figure 5.13; for a TEM image of a crevice free solar cell as comparison refer to figure 2.3. The junction of sample F is properly formed across most of the cross-section, which explains that we still observe a moderately operating device. The chemical bath deposition of CdS allows a homogeneous covering of even deep crevices. However, at some defect regions the CdS cover seems to be discontinued; this would explain the reduced shunt resistance of the device with resulting leakage currents impairing the performance. The ZnO layer covers the complete cell, but does not enter into the crevices. Additionally, the ZnO thickness varies – this can be correlated to the increased series resistance, which is usually determined by the TCO. At the crevices we have voids in the device, i.e. a locally discontinued junction. The reverse bias QE indicates both a reduced space charge region and increased interface recombination – the discontinued junction could account for both. Consequently, we expect higher recombination rates for carriers created at or close to the crevices. The cross-sectional micrographs, therefore, support the concept of a correlation between morphology and device performance that is mainly related to the crevices between absorber grains.

## 5.6 Conclusions

The isothermal three-stage process with an In+Ga+Se / Cu+Se / In+Ga+Se deposition sequence at constant substrate temperature, monitored by the end point detection method (EPD), allows to grow CIGS absorbers for high efficiency photovoltaic devices. Using this process, we can observe a two section growth of the absorber, with the lower section forming during the 2<sup>nd</sup> stage through the indiffusion of Cu into the  $\text{In}_x\text{Ga}_y\text{Se}$  precursor from the 1<sup>st</sup> stage and the outdiffusion of In and Ga to the  $\text{Cu}_x\text{Se}$  segregated on top. This yields an absorber section not affected by the duration of the Cu-rich interval. The upper section grows from a conversion of  $\text{Cu}_x\text{Se}$  precursors during the 3<sup>rd</sup> stage resulting in crevices between the film's grains and increased roughness parameters. While the second section of  $\text{Cu}(\text{In,Ga})\text{Se}_2$  grows, the  $\text{Cu}_x\text{Se}$  is gradually consumed; it remains at the grain boundaries, where the crevices then form when it is further depleted. This explains that the duration of the period during which the film is Cu-rich, determining the amount of  $\text{Cu}_x\text{Se}$  deposited, is correlated to the surface morphology of the films.

In this study, the Cu-rich deposition time has been varied and characterized by the  $\text{Cu}/(\text{In+Ga})$  ratio  $y_{nd}$  at the end of the second stage. EDX, XRD and SIMS measurements show only minor variations in the material composition not correlated to the device performance. The absorber surface has been investigated

with SEM and AFM to determine the morphology and calculate roughness parameters. A slight increase in device performance is obtained from  $J_{SC}$  increasing with roughness, mostly related to reduced interference in the ZnO. This effect saturates for a morphology close to that of sample D. For further increasing roughness and deeper crevices, the junction quality is impeded leading to a significant reduction of all device parameters. FF and  $V_{OC}$  are already slightly reduced when the current is at its maximum, thus the best efficiency was achieved with morphology B. QE and  $I(V)$  data point towards interface recombination playing a major role in the decrease of device parameters, which is consistent with an impaired junction formation around crevices visible in cross-sectional SEM. It could be interesting to use light beam induced current (LBIC) measurements, i.e. spatially resolved QE (at a single wavelength), to see if the current reduction might be spatially correlated to the crevices. However, the lightspot would have to be in the sub- $\mu\text{m}$  range – the so far best system has a resolution of 1  $\mu\text{m}$  [62]. An alternative with better resolution could be electron beam induced current (EBIC).

Reverse bias QE reveals a slight collection loss in sample E and a more considerable one for sample F. Quantitatively these amount to current density losses of 0.5 and 5.2  $\text{mA}/\text{cm}^2$ , respectively. An additional reduction of QE in these two cells can be attributed to the low level illumination and is related to the CdS photoconductivity - carriers created by the bias light fill trap states in the CdS and make this more n-type, resulting in a wider space charge region. The quantitative analysis of the current losses shows that the optical gain in  $J_{SC}$  (reduced interference) is 1.1  $\text{mA}/\text{cm}^2$ . A comparison of series resistances from a fit to  $I(V)$  curves under illumination and in the dark to those derived from quantum efficiency under forward voltage bias shows the susceptibility of this parameter to the conditions of the illumination.

A rough absorber can help to achieve a rough interface, which is desirable to avoid a reduction of the photocurrent related to interference. The rough interface will break up the interferometric structure of the parallel ZnO surfaces. Crevices, however, hinder the device performance. The isothermal three-stage process is not suited to optimize the surface morphology, as rougher surfaces come along with deeper crevices. From this point of view, a process that creates rough absorbers without crevices between the grains would be superior. However, the growth of crevices is also known from other co-evaporation recipes [20, 73]. Actually, the three-stage process is known to allow crevice free large grained absorbers [69] – provided the Cu-rich interval is not prolonged too much, as this study has shown. It should be added, that in encapsulated cells (or modules) the optical interface between cell surface and encapsulant, usually glass, needs to be considered. An encapsulant which has a lower refractive index than ZnO already reduces reflection and interference.

In general, the achieved efficiency stays high over a wide range of different durations of the Cu-rich interval during the deposition sequence. Up to sample D, losses in fill-factor and voltage are modest and partially compensated by current gains; whereby, efficiencies differ by no more than 0.5 %. The Cu-rich interval is, consequently, not a very critical parameter in avoiding low-yield absorbers, as long as  $y_{nd} \leq 1.5$ .

## 6 Summary

This report has given details on the quantum efficiency system developed and subsequently assembled for the photovoltaics research at the Université de Nantes. Such a system allows to spectrally resolve the photocurrent and analyze loss mechanisms limiting the current yield. The research in Nantes is focussed on thin-film solar cells with  $\text{Cu(In,Ga)Se}_2$  absorber; in this framework, the QE system has been applied in a study on the effects of varying the duration and magnitude of temporary Cu-richness during a three-stage co-evaporation deposition. CIGS solar cells are a technology just entering the market, but there are still many pathways to improve their performance and since much of the past progress has been achieved empirically, a better understanding of the device physics is needed. The contribution of this work is twofold. On the one hand, the instrument built will facilitate the research of other scientists in this field and possibly even serve as model for other setups. On the other hand, an analysis and discussion on the impact of changing a specific deposition parameter was carried out with the help of the QE and other characterizational techniques.

Basics of the photovoltaic generation of electricity in a p-n junction have been presented in chapter 2; particularly,  $\text{Cu(In,Ga)Se}_2$ , a I-III-VI<sub>2</sub> compound semiconductor, as absorber material for heterojunction thin-film solar cells has been discussed. Through asymmetric doping and choice of bandgaps the junction partner  $\text{ZnO:Al}$  serves as window, while most absorption is in the CIGS. The device performance is improved through the introduction of buffer layers, giving a layered structure of glass/Mo/CIGS/CdS/i-ZnO/ZnO:Al for these solar cells. Absorbers for cells presented in this report were grown using co-evaporation (multi-source physical vapor deposition) following a three-stage In+Ga+Se/Cu+Se/In+Ga+Se procedure at constant substrate temperature.

As essential measurements towards understanding device physics and improving the performance of solar cells, the photoelectric characterization by recording current-voltage and quantum efficiency (QE) curves have been introduced in chapter 3. The focus of this report is on the latter, defined as spectrally resolved ratio of electrons collected from the device per incident photons. Technically, the photocurrent under monochromatic light is recorded during a spectral scan across the absorbed wavelengths. The knowledge of loss mechanisms limiting the QE allows conclusions on their influence on the device physics and the current yield. For CIGS thin-film cells, these losses include grid shading (in laboratory cells), front surface reflection, ZnO absorption above the bandgap and by free carriers, buffer absorption, incomplete absorption of long wavelengths in the CIGS, and finally incomplete collection of charge carriers from recombination of electrons and holes.

Due to the large number of defects, Shockley-Read-Hall recombination in the absorber bulk or at the interface is dominant. A possibility to further investigate the collection is using QE with a bias voltage applied on the device. Reverse bias increases the space charge region and should improve collection if significant recombination occurs under unbiased conditions. Another variation is the superposition of continuous white light on the periodically modulated monochromatic light of lower intensity; this is termed light bias and allows probing under more realistic operating conditions. Both voltage and light bias have been discussed in view of device operation and particularly buffer photoconductivity. Some basics on the analytical description of the QE have been given; they allow the simulation of QE curves or the derivation of parameters from fits to the QE curve. Furthermore, procedures to derive the bandgap and the short-circuit current density from QE data have been described.

A quantum efficiency system has been designed to fit the requirements of the research groups in Nantes. Its setup has been described in chapter 4. The measurement procedure has been completely automated and is governed from a PC. The choice was to build a grating monochromator based dual-beam QE system, where all measurements are conducted in relation to a reference cell measured at the same time as the device under test or calibration cell. This corrects for fluctuations in the lamp intensity and reduces errors introduced by the spikes in the Xenon lamp spectrum. The quantum efficiency of a test device is deduced from that of a calibrated photovoltaic detector measured earlier in the same light-path. For CIGS solar cells, the system operates in chopped light mode with lock-in detection. However, a steady-state mode (continuous illumination) using digital multimeters for detection is provided in order to allow QE measurements of dye-sensitized solar cells. The use of a bifurcated fiber bundle as light-splitter allows great flexibility and easy use, but comes at the price of a significant ( $\approx 80\%$ ) loss in light intensity mostly resulting from the light coupling into the fiber. Nevertheless, the system's monochromatic illuminating power on the cells, that on average is  $8\ \mu\text{W}$ , has proven sufficient – nonlinearities in all tested cells had saturated at the given illumination level. Straylight from the monochromator is negligible for the complete measurement range of 340-1360 nm. Options for light bias and voltage bias in chopped light mode were successfully implemented. Whilst the light bias is provided through an additional halogen lamp directly focussed on the cells, the supply for the voltage bias is included in the current to voltage preamplifier.

Systematic and random error sources for the instrument have been discussed. Among the systematic errors, that of the QE of the calibrated detector used in the calculation is the most dominant – stated by Hamamatsu at 5%. The noise in the system was investigated and found to lie below 0.5%. In repeated measurements on the same cells, the  $J_{SC}$  calculated from the QE was found to vary by up to 2% over a period of two months; this can be taken as an indicator for

random errors. Repeatability within a measurement session showed much better agreement. Intercomparison with the National Renewable Energy Laboratory (NREL) in Boulder, Colorado, showed a deviation of only 1 %. Further comparisons were done to measurements from the Ångström Solar Center in Uppsala and the Helmholtz Zentrum Berlin, falling within 3 % of the results from Nantes; this is an indicator for systematic errors. The shapes of the curves are also well reproduced between the laboratories. None of the systems seems to be particularly biased, as the deviation is almost equal to the reproducibility of measurements in Nantes. On the basis of the good comparability and reproducibility, the precision of the system is estimated at 5 %. The error for dye-sensitized solar cells lies somewhat above this, due to less spatial homogeneity of these cells.

In chapter 5, Cu(In,Ga)Se<sub>2</sub> solar cells have been investigated that were grown from an isothermal three-stage co-evaporation process. The transitions between Cu-poor and Cu-rich stages has been monitored by end point detection (EPD), based on the sample emissivity detected via the heater output power necessary to keep the substrate temperature constant. The duration of the 2<sup>nd</sup> stage has been varied and, thus, also the maximum Cu/(In+Ga) ratio before passing back to an overall Cu-poor composition. From SEM and AFM micrographs this can be correlated to changes in surface morphology: Longer Cu deposition leads to greater surface roughness (root-mean-square roughness), larger crystal grains and deeper crevices between the grains. An increase of the final EPD signal, i.e. emissivity, for the most Cu-rich samples can be correlated to this increase in surface area. Variations seen in EDX and XRD measurements on the absorbers are not large enough to expect a strong influence on the device performance and don't point to a correlation with the change in Cu supply. From SIMS depth profiles and SEM data, together with growth models for three-stage co-evaporation, we can conclude a two section growth of the absorber. The first section, which is unaffected by the varied Cu/(In+Ga) ratio at the end of the 2<sup>nd</sup> stage, results from the interdiffusion of Cu, In and Ga between the Ga<sub>x</sub>In<sub>y</sub>Se precursor from the 1<sup>st</sup> stage and Cu<sub>x</sub>Se deposited in the 2<sup>nd</sup> stage. Such an interdiffusion leads to Ga gradients; these are visible in our SIMS profiles. After the film evolves Cu-rich, the excess Cu<sub>x</sub>Se deposited is the precursor for the upper section of the CIGS formed through metal interdiffusion in the 3<sup>rd</sup> stage, when again In and Ga are evaporated in place of Cu. Such a conversion of Cu<sub>x</sub>Se to CIGS is known to lead to the observed large grained morphology with deep crevices.

Analyzing the solar cells produced from these absorbers, high efficiencies are obtained as long as the film did not evolve too Cu-rich during the 2<sup>nd</sup> stage (max. Cu/(In+Ga) ≤ 1.5). The change in surface morphology appears to be the most important factor influencing the efficiency of resulting photovoltaic devices: an increase in surface roughness has a positive effect on the  $J_{SC}$ , primarily by reducing interference – quantitatively a little more than 1 mA/cm<sup>2</sup>. This increase

is partially balanced by a slight decrease in open-circuit voltage and fill factor. For  $\text{Cu}/(\text{In,Ga}) > 1.5$ , all device parameters (FF,  $V_{OC}$ ,  $J_{SC}$ ) deteriorate strongly. The reduced  $V_{OC}$  cannot be explained from the increased junction area, a relation which can be inferred from the diode model. The reduction of current density by up to  $5 \text{ mA/cm}^2$  can clearly be attributed to collection losses when looking at the QE under reverse voltage bias. For the Cu-richest growth conditions, an additional reduction of the long-wavelength QE related to CdS photoconductivity is observed; measured as  $J_{SC}$ , this amounts to  $1 \text{ mA/cm}^2$ . The collection losses are the result of a narrower space charge region and increased interface recombination, both possibly related to the crevices between crystal grains. This idea is confirmed by cross-sectional micrographs of the roughest sample; they show voids in the solar cells, i.e. the ZnO only covers but does not enter the crevices. It could be interesting to investigate if such a reduction in device performance is localized around the crevices, which the proper junction formation seen in the micrographs for the rest of the cell suggests. Additionally, other possible losses in the QE have been discussed and quantified. From measurements under forward bias, a value for the series resistance has been calculated; this disagrees with values from fitting to the current-voltage curve, which, however, is not surprising when considering the completely different illumination conditions.

The quantum efficiency system drafted and built during this diploma work to spectrally resolve current losses in thin-film solar cells has proven to give reliable results, both in various tests and in the application during the specific study on  $\text{Cu}(\text{In,Ga})\text{Se}_2$  solar cells presented in this report. This study has, furthermore, shown that when going too Cu-rich in the second stage of an isothermal three-stage co-evaporation process, device performance is impaired by crevices formed between the absorber grains.

# A Thin-film Material Characterization

When investigating materials used in thin-film solar cells based on polycrystalline semiconductors, a variety of established techniques are used for surface and cross-sectional imaging, as well as for analyzes of structure and composition. This section will only briefly cover the methods from material research used in chapter 5 and the reader is referred to the literature for further details and a wider coverage of methods; a good review in regard to thin-film photovoltaics being given by Durose et al. [71].

## A.1 Scanning Electron Microscopy (SEM)

De Broglie's hypothesis of wave-particle duality and the resulting association of a wavelength  $\lambda = h/p$  to any particle, where  $h$  is Planck's constant and  $p$  the particle's relativistic momentum, led to the possibility of imaging beyond the diffraction limit of optical microscopy using the much lower wavelengths of electron beams. Electron microscopy was pioneered in the early 1930s by Knoll and Ruska [78] and has since developed to a major imaging technology encompassing a great variety of systems. The beam of accelerated electrons is focussed on the probe by means of electromagnetic lenses based on the Lorentz force or electrostatic lenses using the Coulomb force. The resolution is usually limited more by the aberration of the lenses than by the wavelength corresponding to the electron's momentum. First setups were transmission electron microscopes (TEM) in which the electron beam<sup>1</sup> of typically 40-400 keV passes through a sufficiently thin sample and afterwards either the image or the diffraction pattern can be focussed onto the detector plane.

However, the diffraction of transmitted electrons is not the only interaction between electron beam and sample. Other effects that can be detected and form the base of characterizing techniques include secondary, backscattered and Auger electrons, as well as bremsstrahlung, characteristic x-rays and cathodoluminescence. Secondary electrons emitted by the sample following the excitation from the incident beam and to a certain extent also backscattered electrons form the base of scanning electron microscopy. Here the beam is focussed to a small spot and by use

---

<sup>1</sup>The beam (kinetic) energy in [eV] is equal to the accelerating potential  $U$  in [V] as  $E_{kin} = q \cdot U$  ( $q$  is the elementary charge) for electrons accelerated in an electrostatic field.

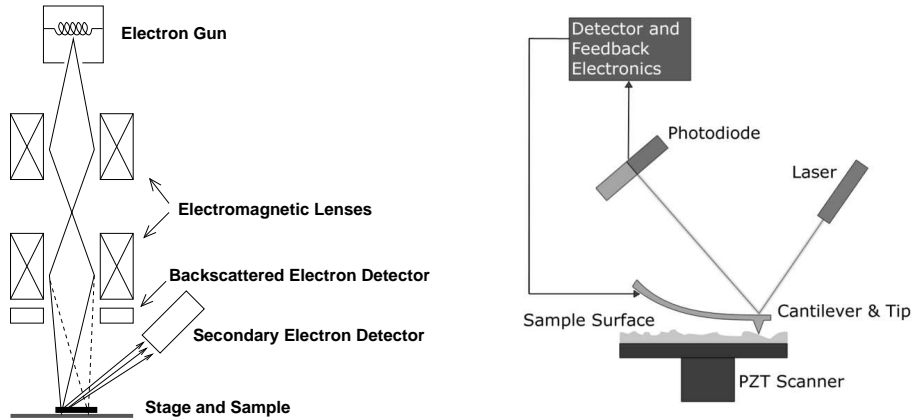


Figure A.1: Simplified schematic view of SEM (left) and AFM (right) setups to illustrate their operating principles.

of deflection lenses scanned across the surface of the specimen, see figure A.1. Detection of low energy ( $< 50$  eV) secondary electrons, generally from the k-orbitals, is achieved by attracting them to the detector with a grid biased at a low voltage (around +400 V); in the detector, a scintillator is at a much higher potential so the electrons are sufficiently accelerated to cause cathodoluminescence in the scintillator. Thereby emitted photons are detected in a photomultiplier. Secondary electron emission in the specimen is dependent on the topography, whereby, detection of the electron signal for each point of the raster yields a surface image that in modern systems is directly recorded in a computer system [79].

Electron microscopes usually operate in high vacuum, to avoid electron interaction with gas molecules. Beam power in SEM systems is up to 40 keV. The sample is grounded to prevent it from charging up, the sample current being another parameter that can be measured.

Images for this report were obtained from a commercial JEOL 6400F scanning electron microscope working at 7-8 kV accelerating potential with the magnification set to 20 000x. Additional micrographs of polished cross-sections were measured at the Helmholtz-Zentrum Berlin.

## A.2 Atomic Force Microscopy (AFM)

Atomic force microscopy is one of several methods belonging to the genre of scanning probe microscopy (SPM). SPM encompasses imaging techniques scanning a very sharp tip over the sample surface. The image can be recorded by either

monitoring a change in the interaction with the surface or by keeping the interaction constant and recording the necessary vertical adjustment to do so. This way a three dimensional surface profile is recorded and not just a two dimensional projection image, like in SEM.

In atomic force microscopy, introduced by Binnig et al. [80], the force between tip and surface is used as interaction. The tip is carried by a cantilever that is monitored with the help of a reflected laser beam recorded on two or more photodiodes mounted side by side, see figure A.1. This way either the deflection of the cantilever during a scan can be measured, or the sample (or tip) is moved with a piezoelectric crystal to keep the cantilever position constant and the voltage applied to the piezo yields the topographic image. Atomic force microscopy can be carried out in contact, non-contact or intermittent contact mode. In the first mode the tip touches the surface during the lateral scan; the force between them is repulsive. In non-contact or intermittent contact mode the cantilever is oscillated at or close to its fundamental resonance frequency or a harmonic, with the tip at a few angstroms above the surface; the force between them in this case is attractive. To calibrate the system, standard samples are measured. Disadvantages lie in the possible presence of tip artefacts in the images and the insufficient representation of steep inclinations and deep trenches. [71]

The digital data matrix of the form  $z = s(x, y)$  recorded in AFM can be plotted to give a topographical image similar to those of SEM, but can further be used for more quantitative analysis of surface features, such as angles and roughness. A simple example are histograms representing the distribution of measured tip heights from an assigned zero point.

The instrument used was a Digital Instruments (DI) Nanoscope IIIA operated in tapping (intermittent contact) mode in air.

### A.3 Energy Dispersive X-ray Spectroscopy (EDX)

In a scanning electron microscope fitted with an x-ray detector a compositional analysis can be made from the emitted characteristic x-rays in what is termed energy dispersive x-ray spectroscopy (EDX).

When an incoming electron causes the ejection of a secondary electron from an inner shell of an atom, a third electron from a higher electronic level will fill the hole during relaxation of the atom, as the excited state is instable (see figure A.2). During this transition from a high- to a low-energy level, a photon carrying the corresponding excess energy  $h\nu$  is emitted:

$$E_i - E_f = h\nu \tag{A.1}$$

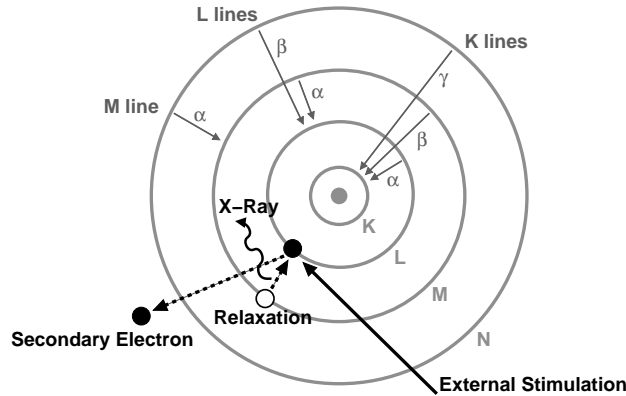


Figure A.2: Scheme of secondary electron ejection and characteristic x-ray emission with line types usually observed in x-ray spectra (level multiplicity of inner shells is omitted for clarity).

Here  $E_i$  stands for the energy of the initial and  $E_f$  for that of the final electronic state. The energy difference  $h\nu$  from transitions involving core levels usually lies in the x-ray domain of the electromagnetic spectrum. In the EDX detector, in most cases a semiconductor detector, the energy of the photons is analyzed energy-dispersively, meaning that the created electronic pulse is counted in the channel corresponding to its intensity of a multichannel analyzer. For each element, different transitions are possible depending on the energy levels in which the hole is produced and from which the relaxation takes place. This forms a characteristic pattern for each element [79].

By their characteristic x-ray pattern the elements in the sample can be identified, but also their fraction in the sample composition quantified, as the x-ray emission intensity at each particular energy is directly related to the number of transitions taking place and thereby to the number of atoms present.

Measurements were performed using a JEOL 5800LV scanning electron microscope equipped with a germanium X-ray detector.

## A.4 X-ray Diffraction (XRD)

The wavelengths of x-rays are of the same order of magnitude as crystal lattice constants, whereby their diffraction provides an optimal probe of lattice parameters. The crystal atoms act as diffraction centers; constructive and destructive interference of the diffracted beam constrain this beam to certain angles in relation to the incident beam [81]. The angular relationship between incident beam  $\theta_i$

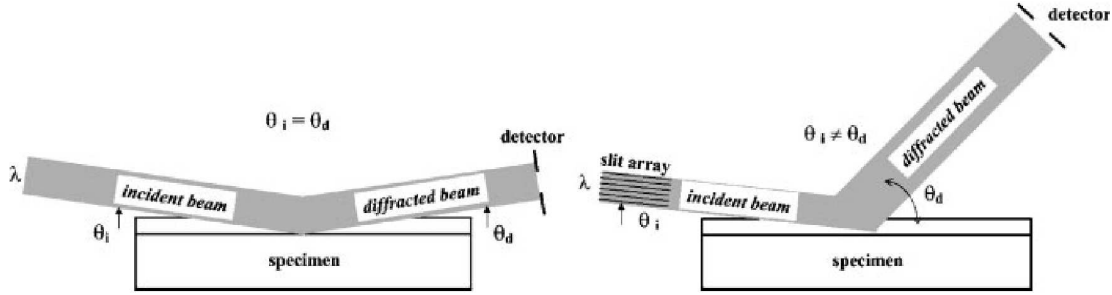


Figure A.3: XRD geometry for symmetrical and asymmetrical configuration on thin-films. *Reproduced from Durose et al. [71].*

and diffracted beam  $\theta_d$  leading to constructive interference is given by the Bragg condition

$$n\lambda = 2d_{hkl} \sin \theta \quad (\text{A.2})$$

where  $n$  is an integer,  $2\theta = \theta_i + \theta_d$ , and  $d_{hkl}$  is the lattice plane spacing corresponding to a crystallographic direction  $\langle hkl \rangle$ .

The geometrical alignment of source, sample and detector needs to allow the detection of diffraction maxima. During a scan, either sample and detector or source and detector are moved to keep the correct angular relationship. Two setup geometries are distinguished for x-ray diffraction, symmetrical Bragg-Brentano geometry with  $\theta_i = \theta_d$  and asymmetrical Seeman-Bohlin geometry with  $\theta_i \neq \theta_d$ ; these are shown in figure A.3. The former constrains the measurements to lattice planes parallel to the sample plane, while the latter probes planes that are tilted with respect to the sample plane. A special case of asymmetric XRD are glancing-incidence measurements made with low incident beam angles to restrict probing to an area closer to the sample surface [71].

By the use of x-ray photons, XRD is a non-destructive method. In symmetric mode, the diffracted intensity measured is plotted versus  $2\theta$ . The diffraction angles, at which a signal is detected, correspond to a lattice spacing  $d_{hkl}$ . Together with intensity ranking of peaks this allows to identify present phases and orientations from known standards. Further quantities commonly sought from thin-film diffraction are lattice parameter, coherency length (related to peak width in the measured spectra) and volume fraction.

Measurements in chapter 5 are restricted to the symmetric Bragg-Brentano configuration and were obtained with a Nonius KappaCCD diffractometer.

## A.5 Secondary Ion Mass Spectrometry (SIMS)

Only very limited information on the compositional depth profile is obtainable by the techniques introduced so far: XRD provides information on the structure of a crystal lattice and from the lattice constants allows conclusions on the elements and compounds present, while EDX yields compositional information from the emitted characteristic x-rays. Cu(In,Ga)Se<sub>2</sub> films, however, particularly when grown in a three-stage process, exhibit vertical gradients of the elements. Secondary ion mass spectrometry (SIMS) allows to analyze this. Additionally, SIMS can provide information on very low elemental concentrations, such as from dopants in a semiconductor or interdiffused elements from other layers of a solar cell [71].

For a SIMS measurement, the specimen is sputtered with a focussed primary ion beam, often oxygen, cesium, gallium or argon, and thereby eroded. Secondary ions from the specimen ejected by the sputtering process are analyzed in a mass spectrometer. The use of mass spectrometry even allows the distinction of different elemental isotopes. Depth information is obtained by a calibration of sputter time to measurements of crater depth with a profilometer in what is called dynamic SIMS mode, while static SIMS with a lower dose of primary ions probes only the uppermost atomic layers of a sample. Owing to the large range of concentrations that can be detected, spanning several orders of magnitude, representation of the data is usually done logarithmically. As the ion yield varies for different elements, quantitative comparisons of their fraction are possible with a special calibration only. From the nature of the probing by sputtering, it is clear that SIMS is a destructive method. Further drawbacks lie in artefacts from lateral inhomogeneities, surface topography and variations in ion yield that can make the data harder to interpret [71].

SIMS measurements were contracted to the Institut für Physikalische Elektronik (IPE, University of Stuttgart). Depth profiles for the contained elements were obtained; however, no calibration for comparison of the elemental fractions was made.

# Bibliography

- [1] S. Rahmstorf and H. J. Schellnhuber. *Der Klimawandel*. C.H. Beck Wissen, 2007.
- [2] Greenpeace International, European Renewable Energy Council (EREC), and German Aerospace Center (DLR). Energy [r]evolution - a sustainable global energy outlook, October 2008.
- [3] D. Ginley, M. A. Green, and R. Collins. Solar energy conversion toward 1 terawatt. *MRS Bull.*, 33(4):355–364, April 2008. URL [http://www.mrs.org/s\\_mrs/bin.asp?CID=12527&DID=206717&DOC=FILE.PDF](http://www.mrs.org/s_mrs/bin.asp?CID=12527&DID=206717&DOC=FILE.PDF).
- [4] M. Mehos. Another pathway to large-scale power generation: Concentrating solar power. *MRS Bull.*, 33(4):364–366, April 2008. URL [http://www.mrs.org/s\\_mrs/bin.asp?CID=12527&DID=208642&DOC=FILE.PDF](http://www.mrs.org/s_mrs/bin.asp?CID=12527&DID=208642&DOC=FILE.PDF).
- [5] L. L. Kazmerski, F. R. White, and G. K. Morgan. Thin-film CuInSe<sub>2</sub>/CdS heterojunction solar cells. *Applied Physics Letters*, 29(4):268–270, 1976. doi: 10.1063/1.89041.
- [6] L. L. Kazmerski. Solar photovoltaics R&D at the tipping point: A 2005 technology overview. *J. Electron. Spectrosc. Relat. Phenom.*, 150(2-3):105–135, February 2006. doi: 10.1016/j.elspec.2005.09.004.
- [7] H. Ullal and B. von Roedern. Thin film CIGS and CdTe photovoltaic technologies: Commercialization, critical issues, and applications - preprint. In *Proceedings of the 22nd European Photovoltaic Solar Energy Conference, Milan*. NREL, September 2007. URL <http://www.nrel.gov/docs/fy07osti/42058.pdf>. NREL/CP-520-42058.
- [8] I. Repins, M. A. Contreras, B. Egaas, C. DeHart, J. Scharf, C. L. Perkins, B. To, and R. Noufi. Short communication: Accelerated publication 19.9ZnO/CdS/CuInGaSe<sub>2</sub> solar cell with 81.2% *Progress in Photovoltaics: Research and Applications*, 16(3):235–239, 2008. doi: 10.1002/pip.822.
- [9] M. A. Green, K. Emery, Y. Hishikawa, and W. Warta. Short communication solar cell efficiency tables (version 32). *Progress in Photovoltaics: Research and Applications*, 16(5):435–440, 2008. doi: 10.1002/pip.842.
- [10] W. N. Shafarman and L. Stolt. *Handbook of Photovoltaic Science and Engineering*, chapter Cu(InGa)Se<sub>2</sub> Solar Cells, pages 567–616. Wiley, 2003.
- [11] B. Andersson. Materials availability for large-scale thin-film photovoltaics. *Prog. Photovoltaics Res. Appl.*, 8(1):61–76, 2000. doi: 10.1002/(SICI)1099-159X(200001/02)8:1<61::AID-PIP301>3.0.CO;2-6.

- [12] C. Platzer-Björkman. *Band Alignment Between ZnO-Based and Cu(In,Ga)Se<sub>2</sub> Thin Films for High Efficiency Solar Cells*. PhD thesis, Uppsala University, 2006. URL <http://urn.kb.se/resolve?urn=urn:nbn:se:uu:diva-6263>.
- [13] R. Klenk. Characterisation and modelling of chalcopyrite solar cells. *Thin Solid Films*, 387(1-2):135–140, May 2001. doi: 10.1016/S0040-6090(00)01736-3.
- [14] C. Agashe, O. Kluth, G. Schpe, H. Siekmann, J. Hpkcs, and B. Rech. Optimization of the electrical properties of magnetron sputtered aluminum-doped zinc oxide films for opto-electronic applications. *Thin Solid Films*, 442(1-2):167–172, October 2003. ISSN 0040-6090. doi: 10.1016/S0040-6090(03)00966-0.
- [15] U. Rau and H. W. Schock. *Clean Electricity from Photovoltaics, Series on Photoconversion of Solar Energy, Vol. 1*, chapter Cu(In,Ga)Se<sub>2</sub> Solar Cells, pages 277–345. Imperial College Press, 2001.
- [16] J. Hedström, H. Olsen, M. Bodegård, A. Kylner, L. Stolt, D. Hariskos, M. Ruckh, and H. W. Schock. ZnO/CdS/Cu(In,Ga)Se<sub>2</sub> thin film solar cells with improved performance. In *Proceedings of the 23rd IEEE Photovoltaic Specialists Conference, Louisville*, page 364, 1993.
- [17] O. Lundberg, M. Edoff, and L. Stolt. The effect of ga-grading in cigs thin film solar cells. *Thin Solid Films*, 480-481:520–525, June 2005. doi: 10.1016/j.tsf.2004.11.080.
- [18] M. Gloeckler and J. Sites. Band-gap grading in Cu(In,Ga)Se<sub>2</sub> solar cells. *Journal of Physics and Chemistry of Solids*, 66(11):1891–1894, November 2005. doi: 10.1016/j.jpcs.2005.09.087.
- [19] W. N. Shafarman and J. Zhu. Effect of substrate temperature and deposition profile on evaporated Cu(InGa)Se<sub>2</sub> films and devices. *Thin Solid Films*, 361-362:473–477, February 2000. doi: 10.1016/S0040-6090(99)00844-5.
- [20] J. Kessler, C. Chityuttakan, J. Lu, J. Schöldström, and L. Stolt. Cu(In,Ga)Se<sub>2</sub> thin films grown with a cu-poor/rich/poor sequence: growth model and structural considerations. *Progress in Photovoltaics: Research and Applications*, 11(5):319–331, 2003. doi: 10.1002/pip.495.
- [21] J. Kessler, D. Schmid, S. Zweigart, H. Dittrich, and H. W. Schock. CuInSe<sub>2</sub> film formation from sequential depositions of In(Se):Cu:Se. In *Proceedings of the 12th European Photovoltaic Solar Energy Conference, Amsterdam*, pages 648–652, April 1994.
- [22] A. M. Gabor, J. R. Tuttle, D. S. Albin, M. A. Contreras, R. Noufi, and A. M. Hermann. High-efficiency CuIn<sub>x</sub>Ga<sub>1-x</sub>Se<sub>2</sub> solar cells made from (In<sub>x</sub>Ga<sub>1-x</sub>)<sub>2</sub>Se<sub>3</sub> precursor films. *Applied Physics Letters*, 65(2):198–200, 1994. doi: 10.1063/1.112670.

- [23] J. Kessler, J. Schöldström, and L. Stolt. Rapid Cu(In,Ga)Se<sub>2</sub> growth using “end point detection”. In *Proceedings of the 28th IEEE Photovoltaic Specialists Conference*, pages 509–512, 2000.
- [24] F. Couzinié-Devy, N. Barreau, and J. Kessler. Dependence of ZnO:Al properties on the substrate to target position in RF sputtering. *Thin Solid Films*, 516(20): 7094–7097, August 2008. doi: 10.1016/j.tsf.2007.12.053.
- [25] D. Liao and A. Rockett. Cu depletion at the CuInSe<sub>2</sub> surface. *Appl. Phys. Lett.*, 82(17):2829–2831, 2003. doi: 10.1063/1.1570516.
- [26] K. Orgassa, U. Rau, Q. Nguyen, H. W. Schock, and J. H. Werner. Role of the CdS buffer layer as an active optical element in Cu(In,Ga)Se<sub>2</sub> thin-film solar cells. *Prog. Photovoltaics Res. Appl.*, 10(7):457–463, 2002. doi: 10.1002/pip.438.
- [27] J. Kessler, K. O. Velthaus, M. Ruckh, R. Laichinger, H. W. Schock, D. Lincot, R. Ortega, and J. Vedel. Chemical bath deposition of cds on cuinse2 etching effects and growth kinetics. In *Proceedings of the 6th International Photovoltaic Science and Engineering Conference, New Delhi*, pages 1005–1010, 1992.
- [28] I. L. Eisgruber, J. E. Granata, J. R. Sites, J. Hou, and J. Kessler. Blue-photon modification of nonstandard diode barrier in CuInSe<sub>2</sub> solar cells. *Solar Energy Materials and Solar Cells*, 53(3-4):367–377, June 1998. doi: 10.1016/S0927-0248(98)00035-X.
- [29] T. J. Nagle. *Quantum Efficiency as a Device-Physics Interpretation Tool for Thin-Film Solar Cells*. PhD thesis, Colorado State University, 2007. URL <http://www.physics.colostate.edu/groups/photovoltaic/PDFs/Tim%20Thesis.pdf>.
- [30] NREL. Reference solar spectral irradiance: Air mass 1.5. Technical report, National Renewable Energy Laboratory, 2003. URL <http://rredc.nrel.gov/solar/spectra/am1.5/>.
- [31] K. Emery. *Handbook of Photovoltaic Science and Engineering*, chapter Measurement and Characterization of Solar Cells and Modules, pages 701–752. Wiley, 2003.
- [32] S. S. Hegedus and W. N. Shafarman. Thin-film solar cells: device measurements and analysis. *Prog. Photovoltaics Res. Appl.*, 12(2-3):155–176, 2004. doi: 10.1002/pip.518.
- [33] D. F. Marrón. *Structural and electronic characterisation of thin-film solar cells based on CVD-grown CuGaSe<sub>2</sub>*. PhD thesis, FU Berlin, 2003. URL <http://www.diss.fu-berlin.de/2003/228>.
- [34] W. Shockley and W. T. Read. Statistics of the recombinations of holes and electrons. *Phys. Rev.*, 87(5):835–842, Sep 1952. doi: 10.1103/PhysRev.87.835.
- [35] R. N. Hall. Electron-hole recombination in germanium. *Phys. Rev.*, 87(2):387, Jul 1952. doi: 10.1103/PhysRev.87.387.

- [36] J. Malmström. *On Generation and Recombination in Cu(In,Ga)Se<sub>2</sub> Thin-Film Solar Cells*. PhD thesis, Uppsala Universitet, 2005. URL <http://urn.kb.se/resolve?urn=urn:nbn:se:uu:diva-5721>.
- [37] J. R. Sites, J. E. Granata, and J. F. Hiltner. Losses due to polycrystallinity in thin-film solar cells. *Sol. Energy Mater. Sol. Cells*, 55(1-2):43–50, July 1998. doi: 10.1016/S0927-0248(98)00045-2.
- [38] R. Klenk and H.-W. Schock. Photocurrent collection in thin film solar cells - calculation and characterization for CuGaSe<sub>2</sub>/(Zn,Cd)S. In *Proceedings of the 12th European Photovoltaic Solar Energy Conference, Amsterdam*, page 1588, 1994.
- [39] J. E. Phillips and M. Roy. Resistive and photoconductive effects in spectral response measurements. In *Proceedings of the 20th IEEE Photovoltaic Specialists Conference*, page 1614. IEEE, 1988.
- [40] J. R. Sites, H. Tavakolian, and R. A. Sasala. Analysis of apparent quantum efficiency. *Solar Cells*, 29(1):39–48, June 1990. doi: 10.1016/0379-6787(90)90013-U.
- [41] F. Engelhardt, L. Bornemann, M. Köntges, T. Meyer, J. Parisi, E. Pschorr-Schoberer, B. Hahn, W. Gebhardt, W. Riedl, and U. Rau. Cu(In,Ga)Se<sub>2</sub> solar cells with a ZnSe buffer layer: interface characterization by quantum efficiency measurements. *Prog. Photovoltaics Res. Appl.*, 7(6):423–436, 1999. doi: 10.1002/(SICI)1099-159X(199911/12)7:6<423::AID-PIP281>3.0.CO;2-S.
- [42] V. L. Dalal and A. Rothwarf. Comment on “a simple measurement of absolute solar cell efficiency”. *J. Appl. Phys.*, 50(4):2980–2981, 1979. doi: 10.1063/1.326181.
- [43] J. Metzdorf. Calibration of solar cells. 1: The differential spectral responsivity method. *Appl. Opt.*, 26(9):1701, 1987. URL <http://ao.osa.org/abstract.cfm?URI=ao-26-9-1701>.
- [44] A. Virtuani, E. Lotter, and M. Powalla. Performance of Cu(In,Ga)Se<sub>2</sub> solar cells under low irradiance. *Thin Solid Films*, 431-432:443–447, May 2003. doi: 10.1016/S0040-6090(03)00184-6.
- [45] A. Pudov, J. Sites, M. Contreras, T. Nakada, and H.-W. Schock. CIGS J-V distortion in the absence of blue photons. *Thin Solid Films*, 480-481:273–278, June 2005. doi: 10.1016/j.tsf.2004.11.099.
- [46] W. W. Gärtner. Depletion-layer photoeffects in semiconductors. *Phys. Rev.*, 116(1):84–, October 1959. doi: 10.1103/PhysRev.116.84.
- [47] N. Meyer, T. Dylla, D. Fischer, M. E. Beck, A. Jäger-Waldau, and L.-S. M. Ch. Solar cells based on HCVD grown CuGaSe<sub>2</sub> absorbers with high open-circuit voltages. In *Proceedings of the 16th European Photovoltaic Solar Energy Conference, Glasgow*, 2000.

- [48] G. P. Smestad, F. C. Krebs, C. M. Lampert, C. G. Granqvist, K. Chopra, X. Mathew, and H. Takakura. Reporting solar cell efficiencies in solar energy materials and solar cells. *Sol. Energy Mater. Sol. Cells*, 92(4):371–373, April 2008. doi: 10.1016/j.solmat.2008.01.003.
- [49] S. M. Wasim, C. Rincón, G. Marín, P. Bocaranda, E. Hernández, I. Bonalde, and E. Medina. Effect of structural disorder on the Urbach energy in Cu ternaries. *Phys. Rev. B*, 64(19):195101–195108, October 2001. doi: 10.1103/PhysRevB.64.195101.
- [50] J. J. Scragg, P. J. Dale, and L. M. Peter. Towards sustainable materials for solar energy conversion: Preparation and photoelectrochemical characterization of  $\text{Cu}_2\text{ZnSnS}_4$ . *Electrochem. Commun.*, 10(4):639–642, April 2008. doi: 10.1016/j.elecom.2008.02.008.
- [51] W. Eisele. *Struktur und Funktion von ZnSe-Pufferschichten in Chalkopyritdünn-schichtszellen*. PhD thesis, Freie Universität Berlin, February 2003. URL <http://www.diss.fu-berlin.de/2003/36/>.
- [52] H. Field. UV-VIS-IR spectral responsivity measurement system for solar cells. In *Presented at the National Center for Photovoltaics Program Review Meeting*. NREL, November 1998. URL <http://www.pvmeas.com/spectralresponsivitymeasurementsystem.pdf>. NREL/CP-520-25654.
- [53] P. M. Sommeling, H. C. Rieffe, J. A. M. van Roosmalen, A. Schonecker, J. M. Kroon, J. A. Wienke, and A. Hinsch. Spectral response and IV-characterization of dye-sensitized nanocrystalline  $\text{TiO}_2$  solar cells. *Sol. Energy Mater. Sol. Cells*, 62(4):399–410, June 2000. doi: 10.1016/S0927-0248(00)00004-0.
- [54] W. Shafarman. Private communication to John Kessler, 1997.
- [55] L. J. Radziemski. Calculation of dispersion for a plane grating in a Czerny-Turner mount: a comment. *Appl. Opt.*, 20(11):1948, 1981. URL <http://ao.osa.org/abstract.cfm?URI=ao-20-11-1948>.
- [56] L. J. Radziemski. Calculation of dispersion for a plane grating in a Czerny-Turner mount: a comment; errata. *Appl. Opt.*, 20(17):2883, 1981. URL <http://ao.osa.org/abstract.cfm?URI=ao-20-17-2871>.
- [57] K. M. Rosfjord, R. A. Villalaz, and T. K. Gaylord. Constant-bandwidth scanning of the Czerny-Turner monochromator. *Appl. Opt.*, 39(4):568–572, 2000. doi: 10.1364/AO.39.000568.
- [58] K. Emery, D. Dunlavy, H. Field, and T. Moriarty. Photovoltaic spectral responsivity measurements. In *Proceedings of the 2nd World Conference on Photovoltaic Solar Energy Conversion (WCPSEC-2), Vienna*, volume 2, page 22982301. NREL, IEEE, 1998. URL [http://www.osti.gov/energycitations/product.biblio.jsp?query\\_id=0&page=0&osti\\_id=677048](http://www.osti.gov/energycitations/product.biblio.jsp?query_id=0&page=0&osti_id=677048).

- [59] TN1000. What is a lock-in amplifier? Technical report, Signal Recovery, 2003. URL <http://www.signalrecovery.com/ApplicationsNotes.htm>.
- [60] TN1001. Specifying lock-in amplifiers. Technical report, Signal Recovery, 2003. URL <http://www.signalrecovery.com/ApplicationsNotes.htm>.
- [61] H. Field. Solar cell spectral response measurement errors related to spectral band width and chopped light waveform. In *Proceedings of the 26th IEEE Photovoltaic Specialists Conference*. NREL, September 1997. NREL/CP-530-22969.
- [62] J. Hiltner. *Investigation of Spatial Variations in Collection Efficiency of Solar Cells*. PhD thesis, Colorado State University, 2001. URL <http://www.physics.colostate.edu/groups/photovoltaic/PDFs/JHThesis.pdf>.
- [63] F. Couzinié-Devy, N. Barreau, and J. Kessler. Influence of absorber copper concentration on the  $\text{Cu}(\text{In,Ga})\text{Se}_2/(\text{PVD})\text{In}_2\text{S}_3$  and  $\text{Cu}(\text{In,Ga})\text{Se}_2/(\text{CBD})\text{CdS}$  based solar cells performance. *Thin Solid Films*, Article in Press, Accepted Manuscript, 2008. doi: 10.1016/j.tsf.2008.11.015.
- [64] C. Osterwald, S. Anevsky, and A. Barua. The results of the PEP'93 intercomparison of reference cell calibrations and newer technology performance measurements: Final report. Technical Report NREL/TP-520-23477, NREL, March 1998. URL [http://www.osti.gov/energycitations/product.biblio.jsp?query\\_id=1&page=0&osti\\_id=654067](http://www.osti.gov/energycitations/product.biblio.jsp?query_id=1&page=0&osti_id=654067).
- [65] C. R. Osterwald, S. Anevsky, K. Bücher, A. K. Barua, P. Chaudhuri, J. Dubard, K. Emery, B. Hansen, D. King, J. Metzendorf, F. Nagamine, R. Shimokawa, Y. X. Wang, T. Wittchen, W. Zaiman, A. Zastrow, and J. Zhang. The world photovoltaic scale: an international reference cell calibration program. *Prog. Photovoltaics Res. Appl.*, 7(4):287–297, 1999. doi: 10.1002/(SICI)1099-159X(199907/08)7:4<287::AID-PIP259>3.0.CO;2-I.
- [66] K. Hara and H. Arakawa. *Handbook of Photovoltaic Science and Engineering*, chapter Dye-sensitized Solar Cells, pages 663–700. Wiley, 2003.
- [67] J. Hohl-Ebinger, A. Hinsch, R. Sastrawan, W. Warta, and U. Würfel. Dependence of spectral response of dye solar cells on bias illumination. In *Proceedings of the 19th European Photovoltaic Solar Energy Conference, Paris*, 2004. URL <http://www.ise.fhg.de/veroeffentlichungen/konferenzbeitraege/2004-1/19th-european-photovoltaic-solar-energy-conference-7-11-june-2004-paris/dependence-of-spectral-response-of-dye-solar-cells-on-bias-illumination>.
- [68] D. Bhattacharyya, S. Chaudhuri, A. Pal, and S. Bhattacharyya. Some aspects of surface roughness in polycrystalline thin films: optical constants and grain distribution. *Vacuum*, 43(12):1201–1205, December 1992. doi: 10.1016/0042-207X(92)90024-Q.
- [69] A. M. Gabor. *The Conversion of  $(\text{In,Ga})_2\text{Se}_3$  thin film to  $\text{Cu}(\text{In,Ga})\text{Se}_2$  for application to photovoltaic solar cells*. PhD thesis, University of Colorado, 1995.

- [70] S. Chaisitsak, Y. Tokita, R. Miyazaki, A. Yamada, and M. Konagai. Control of preferred orientation for Cu(In,Ga)Se<sub>2</sub> thin films and its effect in solar cell performance. In *Proceedings of the 17th European Photovoltaic Solar Energy Conference, Munich*, pages 1011–1014, 2001.
- [71] K. Durose, S. E. Asher, W. Jaegermann, D. Levi, B. E. McCandless, W. Metzger, H. Moutinho, P. Paulson, C. L. Perkins, J. R. Sites, G. Teeter, and M. Terheggen. Physical characterization of thin-film solar cells. *Prog. Photovoltaics Res. Appl.*, 12(2-3):177–217, 2004. doi: 10.1002/pip.542.
- [72] D. Schmid, M. Ruckh, and H. W. Schock. Photoemission studies on Cu(In, Ga)Se<sub>2</sub> thin films and related binary selenides. *Applied Surface Science*, 103(4):409–429, December 1996. doi: 10.1016/S0169-4332(96)00099-2.
- [73] J. Schöldström, J. Kessler, and M. Edoff. Two-stage growth of smooth Cu(In,Ga)Se<sub>2</sub> films using end-point detection. *Thin Solid Films*, 480-481:61–66, June 2005. doi: 10.1016/j.tsf.2004.11.076.
- [74] G. Palasantzas and E. Koumanakos. Roughness effect on heterojunction photovoltaics. *J. Appl. Phys.*, 79(11):8531–8536, 1996. doi: 10.1063/1.362532.
- [75] J. Connolly, Z. Djebbour, A. Darga, C. Bazin, D. Mencaraglia, M. Benosman, N. Bodereau, J. Guillemoles, D. Lincot, J. Kessler, N. Naghavi, J. Kurdi, and O. Kerrec. Analysis of efficiency limiting processes in thin lm Cu(In,Ga)(S,Se)<sub>2</sub> electrodeposited solar cells. In *Proceedings of the 20th European Photovoltaic Solar Energy Conference, Barcelona*, pages 1851 – 1854, 2005.
- [76] A. Kanevce. *Anticipated Performance of Cu(In,Ga)Se<sub>2</sub> Solar Cells in the Thin-film Limit*. PhD thesis, Colorado State University, 2007. URL <http://www.physics.colostate.edu/groups/photovoltaic/PDFs/Ana%20Thesis.pdf>.
- [77] K. Orgassa. *Coherent optical analysis of the ZnO/CdS/Cu(In,Ga)Se<sub>2</sub> thin film solar cells*. PhD thesis, Universität Stuttgart, 2004.
- [78] M. Knoll and E. Ruska. Das Elektronenmikroskop. *Z. Phys. A: Hadrons Nucl.*, 78(5-6):318–339, May 1932. doi: 10.1007/BF01342199.
- [79] G. I. Goldstein, D. E. Newbury, P. Echlin, D. C. Joy, C. Fiori, and E. Lifshin. *Scanning electron microscopy and X-ray microanalysis*. Plenum Press, 1992.
- [80] G. Binnig, C. F. Quate, and C. Gerber. Atomic force microscope. *Phys. Rev. Lett.*, 56(9):930–933, March 1986. doi: 10.1103/PhysRevLett.56.930.
- [81] N. W. Ashcroft and N. D. Mermin. *Solid State Physics*. Thomson Learning, 1976.

To resolve the digital object identifiers (DOI) given in this bibliography where available, append the DOI string to the URL <http://dx.doi.org/>.

# List of Figures

2.1	Schematic band model for a semiconductor . . . . .	3
2.2	Scheme of a p-n junction and its band diagram . . . . .	4
2.3	TEM cross-section of complete CIGS solar cell and typical band diagram . . . . .	6
2.4	Configuration for multisource elemental co-evaporation . . . . .	8
3.1	Characteristic $I(V)$ -curve of a solar cell and basic parameters . . . . .	12
3.2	Equivalent circuit of a solar cell using a one diode model . . . . .	13
3.3	Loss mechanisms in quantum efficiency measurements on CIGS cells . . . . .	15
3.4	Main Recombination paths in thin-film solar cells . . . . .	19
3.5	Reverse voltage bias artefact from CdS photoconductivity . . . . .	20
3.6	ASTM G173-03 solar spectrum and comparison to CIGS QE . . . . .	24
3.7	Example of bandgap determination from a QE curve . . . . .	26
4.1	Measurement principle of a dual beam QE-setup . . . . .	29
4.2	The quantum efficiency setup (photograph) . . . . .	30
4.3	Schematic overview of the QE-Setup . . . . .	30
4.4	Optical Filter Transmittance . . . . .	33
4.5	Stray light in the infrared domain . . . . .	35
4.6	Fiber setup spectral light transfer . . . . .	36
4.7	Typical signal intensity and beam power . . . . .	38
4.8	Lock-in signals and their ratio over time . . . . .	44
4.9	Reproducibility of QE measurements . . . . .	45
4.10	Intercomparison of QE measurements . . . . .	46
4.11	Dye-sensitized cell QE under AC illumination and spatial variation . . . . .	49
4.12	Dye-sensitized cell QE for two different dyes . . . . .	50
5.1	End point detection signal evolution . . . . .	52
5.2	EPD of the Cu-poor/Cu-rich/Cu-poor transitions for varied Cu-richness . . . . .	53
5.3	AFM histograms and root-mean-square roughness . . . . .	54
5.4	SEM images showing the evolution of absorber morphology . . . . .	55

5.5	AFM images and extracted line profiles . . . . .	56
5.6	XRD spectrum and CIGS peaks in XRD measurements . . . . .	59
5.7	SIMS depth profiles for samples B and D . . . . .	60
5.8	Device parameters as boxplot . . . . .	63
5.9	QE curves for the cells with different absorber roughness . . . . .	66
5.10	QE under voltage bias for the roughest samples E and F . . . . .	66
5.11	Dependence of $\Delta J_{SC}$ on the absorber roughness. . . . .	68
5.12	QE under forward bias and deduction of $R_s + R_L$ for sample E . . . . .	71
5.13	SEM micrographs of polished cross-sections for sample F . . . . .	73
A.1	Simplified schematic view of SEM and AFM setups . . . . .	82
A.2	Scheme of secondary electron ejection and charact. x-ray emission . . . . .	84
A.3	XRD geometry for symmetrical and asymmetrical configuration . . . . .	85

# List of Tables

4.1	System Specifications . . . . .	41
4.2	$J_{SC}$ calculated from Nantes and NREL measurements . . . . .	47
4.3	$J_{SC}$ calculated from Nantes, Uppsala and Berlin measurements . . . . .	48
5.1	Roughness parameters from AFM . . . . .	54
5.2	Compositional ratios as measured by EDX . . . . .	58
5.3	$\Delta V_{OC}$ due to increased junction area . . . . .	62
5.4	Parameters from single diode model fit to light $I(V)$ curves . . . . .	64
5.5	Breakdown of photocurrent density $J_L$ by separation of loss mechanisms .	70
5.6	Values of $R_s + R_L$ deduced from quantum efficiency. . . . .	72

# Acknowledgements

Foremost, I am grateful to my supervisors Prof. John Kessler in Nantes and Prof. Martha Lux-Steiner in Berlin for enabling me to carry out my diploma work in France. Their guidance and suggestions were essential for my research and the writing of this report.

The study in chapter 5 was done in collaboration with Nicolas Barreau; together with Lionel Assmann, he also deposited the absorbers, built the solar cells and did some of the material measurements. Besides John and Nicolas, also Ludovic Arzel, François Couzinié-Devy, Thomas Painchaud and Hakim Marko were not only open for scientific discussions at any time, but also the most pleasant company in the office, the lab and for lunchtime “pique-niques”, as well as for concerts or evenings in a bar – merci!

For preliminary work on a QE setup for Nantes, I thank Baptiste Berenguier. On optics, I had fruitful discussion with Cyril Lupi. For the AFM measurements and advice on their analysis, I like to thank Patricia Bertoncini. As this was not possible in Nantes, Ulrike Bloeck und Dr. Daniel Abou-Ras at the Helmholtz-Zentrum Berlin were so kind to polish the cross-sections shown in figure 5.13 and take the SEM images. Also from the Helmholtz-Zentrum, I would like to thank Sebastian Lehmann, responsible for the QE of SE2, and Jörg Beckmann, who wrote the LabView measurement software for the QE that I could use as framework for my own programming. Concerning dye-sensitized solar cells I worked with Yann Pellegrin and Fabrice Odobel.

For additional reading of the manuscript, I am thankful to Pablo Thier and Christian Herzog – and with them I would like to thank all the other friends of the past years.

Without the continuous support of my family I would not have come so far. My grandfather, furthermore, was the most motivating proofreader imaginable. Hanna, I am grateful for the good time we shared while in Nantes, for your patience and support – not only during this past year.